

DESIGN OF A MULTI-DISC ELECTROMECHANICAL BRAKE

By

Ryan James Farris

Thesis

Submitted to the Faculty of the
Graduate School of Vanderbilt University
in partial fulfillment of the requirements
for the degree of

MASTER OF SCIENCE

in

Mechanical Engineering

December, 2009

Nashville, Tennessee

Approved:

Professor Michael Goldfarb

Professor Eric Barth

Professor Nilanjan Sarkar

Copyright © 2009 by Ryan James Farris
All Rights Reserved

To my adorable wife, Renee

ACKNOWLEDGEMENTS

I would like to acknowledge above all God who has made the laws that govern our physical world and has given us the capacity to learn and use these laws to benefit man.

I would like to thank Dr. Michael Goldfarb for the example of his humility despite being the most capable engineer I have ever met. I also want to thank him for his skillful teaching and guidance which has helped me to keep my poles in the left half plane during grad school. I am also grateful to the members of my thesis committee Dr. Eric Barth and Dr. Nilanjan Sarkar for their time and support.

I want to express my deepest appreciation to Dr. Chris Byrne for the vision that he imparted to me during my undergraduate years. His wise counsel and enthusiastic pursuit of knowledge inspires me. I cannot thank him enough for the opportunities he gave me to learn, to build character, and to light fires.

My gratitude also belongs to my best friend, my wife, Renee. She has given me her love and support throughout my graduate studies and together with her I look forward to whatever the future may bring. In addition, I thank my entire family for the encouragement they have provided every step of the way.

Lastly, I would like to acknowledge all the members of the Center for Intelligent Mechatronics for their help and camaraderie. In particular, I thank Dr. Tom Withrow for his friendship and practical advice during my time at Vanderbilt.

TABLE OF CONTENTS

	Page
DEDICATION	iii
ACKNOWLEDGEMENTS.....	iv
LIST OF FIGURES.....	viii
LIST OF TABLES.....	xii
Chapter	
I. INTRODUCTION	1
1. Introduction	1
2. References	4
II. BRAKE DESIGN ITERATIONS.....	7
1. Introduction	7
2. Wafer Disc Brake Prototype 1	7
2.1 Design and Operation.....	7
2.2 Finite Element Analysis.....	11
2.3 Performance	12
2.4 Conclusions.....	14
3. Wafer Disc Brake Prototype 2	15
3.1 Design and Operation.....	15
3.2 Performance	19
3.3 Conclusions.....	21
4. Wafer Disc Brake Prototype 3	22
4.1 Design and Operation.....	22
4.2 Performance	26
4.3 Conclusions.....	30
5. Conclusion.....	31
III. MANUSCRIPT I: DESIGN OF A MULTI-DISC ELECTROMECHANICAL BRAKE	32
1. Abstract.....	33
2. Introduction	33
3. Wafer Disc Brake Design.....	36
3.1 Brake Configuration.....	36
3.2 Design Relationships.....	40
3.3 Special Considerations for the Normally Locked Design	44
4. Brake Control	45

5.	Performance Characterization.....	47
6.	Comparison of Wafer Disc Brake and Magnetic Particle Brake	56
7.	Conclusions and Recommendations.....	60
8.	References	61

Appendix

A.	PART LIST AND DRAWINGS	64
B.	COMPONENT LIST AND DATA SHEETS	81
C.	MATLAB SIMULINK MODELS.....	88
D.	MANUSCRIPT II: DESIGN AND SIMULATION OF A JOINT-COUPLED ORTHOSIS FOR REGULATING FES-AIDED GAIT.....	93
1.	Abstract	94
2.	Introduction	94
3.	Joint-Coupled Controlled-Brake Orthosis (JCO).....	96
3.1	The JCO Gait Sequence	97
3.2	Joint Coupling Design.....	98
3.3	Wafer Disc Brakes	99
3.4	Ankle Support	101
3.5	Mass and Inertia	104
4.	Gait Control and Simulation.....	104
4.1	Walker Model	105
4.2	Orthosis Model	107
4.3	Control Algorithm	107
4.4	S1 : State 1	108
4.5	S2 : State 2	108
4.6	S3 : State 3	108
4.7	S4 : State 4	109
4.8	Simulation Results	111
5.	Preliminary Experiments.....	111
6.	Conclusion.....	114
7.	References.....	114
E.	MANUSCRIPT III: DESIGN OF A JOINT-COUPLED ORTHOSIS FOR FES-AIDED GAIT ..	117
1.	Abstract	118
2.	Introduction	118
3.	Joint-Coupled Controlled-Brake Orthosis (JCO).....	121
3.1	The JCO Gait Sequence	122
3.2	Joint Coupling Design.....	123
3.3	Wafer Disc Brakes	126
3.4	Ankle Support	129
3.5	Mass and Inertia	129
3.6	Donning and Doffing.....	130

4.	Simulation	131
5.	Preliminary Experiments.....	131
6.	Conclusion.....	137
7.	References.....	138

LIST OF FIGURES

Figure	Page
1-1. Sectioned view of a magnetic particle brake.....	2
2-1. Sectioned view of wafer disc brake prototype 1	9
2-2. Wafer disc brake prototype 1	9
2-3. Finite element analysis of discs in wafer disc prototype 1	12
2-4. Holding torque of brake prototype 1 vs. compressive force.....	13
2-5. Sectioned view of the normally locked wafer disc brake prototype 2.....	16
2-6. Wafer disc brake prototype 2	17
2-7. Stainless steel disc stack heat treatment – before and after	20
2-8. Sectioned view of the normally unlocked wafer disc brake prototype 3.....	24
2-9. Sectioned view of the normally locked wafer disc brake prototype 3.....	24
2-10. Wafer disc brake prototype 3	25
2-11. Maxon EC45 flat motor affixed on the outside of brake prototype 3.....	27
2-12. Strain gages applied to compression star	28
2-13. Sinusoidal compressive force tracking in brake prototype 3	28
2-14. Compressive force step response in brake prototype 3.....	29
2-15. Torque output relative to compression force (strain gage) tracking	29
3-1. Sectioned view of a magnetic particle brake.....	35
3-2. Sectioned view of normally unlocked wafer disc brake	38
3-3. Sectioned view of normally locked wafer disc brake	39
3-4. Fully functional wafer disc brake	39
3-5. Schematic of wafer disc brake controller	47
3-6. Experimental setup for testing of the wafer disc brake	49

3-7. Maximum and minimum dynamic wafer disc brake torque	50
3-8. Normally unlocked brake sinusoid tracking.....	53
3-9. Normally locked brake sinusoid tracking.....	53
3-10. Normally unlocked brake step response	54
3-11. Normally locked brake step response	54
3-12. Normally unlocked brake torque gain vs. frequency.....	55
3-13. Normally locked brake torque gain vs. frequency.....	55
3-14. Wafer disc brake power dissipation capacity	56
3-15. Normalized step responses of wafer disc brake and magnetic particle brake.....	59
A-1. Stator tube detail drawing.....	65
A-2. Rotor barrel detail drawing	66
A-3. Top cap detail drawing	67
A-4. Bottom cap detail drawing	68
A-5. Compression star detail drawing.....	69
A-6. Motor cap detail drawing	70
A-7. Stator disc detail drawing	71
A-8. Rotor disc detail drawing.....	72
A-9. Spring guide detail drawing	73
A-10. Disc spacer detail drawing.....	74
A-11. Stator key detail drawing.....	75
A-12. Rotor key detail drawing	76
A-13. DU radial bearing detail drawing.....	77
A-14. DU thrust bearing detail drawing.....	78
A-15. Motor alteration detail drawing.....	79
A-16. Ball screw alteration detail drawing	80

B-1. Motor data sheet	82
B-2. Ball screw data sheet	83
B-3. DU bearing data sheet	84
B-4. Flanged ball bearing data sheet.....	85
B-5. Normally unlocked spring data sheet.....	86
B-6. Normally locked spring data sheet	87
C-1. Simulink diagram of wafer disc brake and dynamometer controller.....	89
C-2. Simulink diagram of brake torque controller	90
C-3. Simulink diagram of brake position controller	91
C-4. Simulink diagram of dynamometer motor controller	92
D-1. Solid model of JCO concept.....	97
D-2. Femur link detail.....	102
D-3. Cross-section of normally locked knee brake	103
D-4. Fully functional knee brake prototype	103
D-5. Dynamic simulation solid model	106
D-6. Simulation states	109
D-7. Simulation results	110
D-8. Procession of simulation states.....	110
D-9. FES/JCO generated gait sequence experiment	113
D-10. Joint angle data during gait experiment shown in Fig. D-9.....	113
E-1. Solid model of JCO concept	120
E-2. Anthropomorphic 50 th percentile male with JCO	122
E-3. Schematic representation of JCO gait sequence	123
E-4. Detailed image of femur link and joint coupling cable.....	124
E-5. Femur link detail	125
E-6. Cross-section of normally locked knee brake	128

E-7.	Fully functional knee brake prototype.....	129
E-8.	Depiction of steps for donning JCO	130
E-9.	Progression of simulation states.....	131
E-10.	FES/JCO generated gait sequence experiment.....	134
E-11.	Joint angle data during gait experiment shown in Fig. E-10.....	134
E-12.	Representative data from quadriceps fatigue experiment	135
E-13.	Representative data from a five-minute quadriceps fatigue experiment.....	136
E-14.	Representative data from a single subject for three consecutive quadriceps fatigue experiments.....	136

LIST OF TABLES

Table	Page
2-1. Summary of brake prototype 2 test results.....	21
3-1. Parameter results of analytical and experimental design optimization.....	44
3-2. Summary of wafer disc brake characterization with comparison to a magnetic particle brake.....	60
A-1. Wafer disc brake fabricated and modified parts.....	64
B-1. Wafer disc brake purchased components.....	81
D-1. Simulation parameters	106

CHAPTER I

INTRODUCTION

1. Introduction

Several control applications require the use of an electrically controllable proportional rotary brake (e.g., [1]-[16]). Probably the most common and thoroughly developed example of such a device is the magnetic particle brake (MPB). Magnetic particle brakes produce a steady-state resistive torque roughly proportional to the input current. A sectioned view of a magnetic particle brake is shown in Figure 1-1. DC current applied to the brake coil induces a magnetic field which links fine ferrite particles to the rotating brake shaft. The amount of current in the coil determines the strength of the magnetic field, which in turn determines the resistive torque imposed on the brake shaft. Compared with the closed-loop control of a high-performance DC torque motor, these devices provide a relatively low electrical power and light-weight means of exerting controlled dissipative mechanical torque. Further, using an electric motor as a dissipater requires measurement of velocity, which typically contains phase lag, which in turn adds energy to the system (rather than dissipating it). A proportional brake, on the other hand, does not require velocity measurement and is guaranteed to be energetically passive.

Though the weight of a magnetic particle brake is low relative to a DC motor (for a given resistive torque), in many cases the weight remains significant. Several efforts to increase the performance of such devices have been reported, including the development of magnetorheological fluid brakes, electrorheological fluid brakes, and piezoelectrically actuated brakes (e.g., [17]-[23]). Magnetorheological and electrorheological brakes provide improved torque-to-weight characteristics relative to magnetic particle brakes, but sacrifice bandwidth and dynamic range relative to the MPB. The piezoelectrically actuated brake described in [23] offers a higher bandwidth and decreased electrical power consumption for low-frequency excitation relative to a magnetic particle brake, but provides less torque-to-weight and more torque ripple.

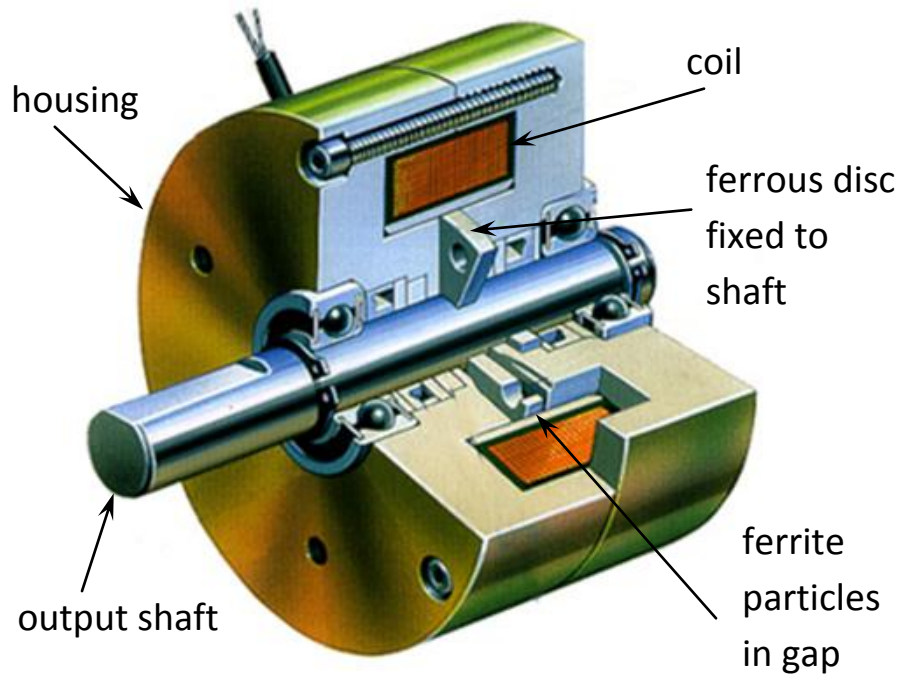


Figure 1-1. Sectioned view of a magnetic particle brake taken from PrecisionTork.com.

This thesis presents the design of an electrically-actuated proportional brake that provides a significantly improved torque-to-weight ratio relative to a magnetic particle brake, while maintaining (or improving) dynamic range and response time. Importantly, unlike particle brakes, magnetorheological fluid brakes, or electrorheological fluid brakes, the proposed device can be designed in both a normally unlocked and normally locked configuration, which offers a greater number of design options for a given application. The approach utilizes a motor-driven ball screw, which compresses a multiple-disc mechanism for resistive torque generation. Due to the amplification effects of a small ball screw lead and a large number of discs in the disc stack, the brake provides a resistive torque approximately three orders of magnitude larger than the motor torque. Due to the relatively thin discs used on the brake, the authors refer to the device as a wafer disc brake (WDB).

Note that electrically actuated multiple disc brakes and clutches are commercially available and used in heavy equipment applications (e.g., material handling). Such brakes, however, operate similarly to a magnetic particle brake, in that they utilize a stack of ferrous discs subjected to an electrically induced magnetic field. Such brakes are effective, but due to residual magnetism and sticking of plates, do not provide well-behaved proportional operation. Further, due to the nature of the attractive forces generated by a magnetic field, implementation of such brakes in a normally locked configuration would be a nontrivial task. The remainder of this thesis describes the design of the (wafer disc) brake and characterizes and compares its

performance to that of a commercially available magnetic particle brake of comparable size.

2. References

- [1] R. J. Farris, Hugo A. Quintero, Thomas J. Withrow, and Michael Goldfarb, "Design and Simulation of a Joint-Coupled Orthosis for Regulating FES-Aided Gait" *Robotics and Automation, 2009 IEEE International Conference on* , pp.1916-1922, May 2009.
- [2] R. J. Farris, Hugo A. Quintero, Thomas J. Withrow, and Michael Goldfarb, "Design of a Joint-Coupled Orthosis for FES-Aided Gait" *Rehabilitation Robotics, 2009 IEEE International Conference on* , pp.246-252, April 2009.
- [3] M. Goldfarb, W. Durfee, K. Korkowski, and B. Harrold. Evaluation of a Controlled-Brake Orthosis for FES-Aided Gait, *IEEE Transactions on Neural Systems and Rehabilitative Engineering*, vol. 11, no. 3, pp. 241-248, 2003.
- [4] M. Goldfarb and W. Durfee. Design of a Controlled-Brake Orthosis for Regulating FES-Aided Gait. *IEEE Transactions on Rehabilitation Engineering*, vol. 4, no. 1, pp. 13-24, 1996.
- [5] B. Weinberg et al., "Design, Control and Human Testing of an Active Knee Rehabilitation Orthotic Device," *Robotics and Automation, 2007 IEEE International Conference on* , pp.4126-4133, 10-14 April 2007
- [6] J. Chen and W. Liao, "Design and control of a Magnetorheological actuator for leg exoskeleton," *Robotics and Biomimetics, 2007. ROBIO 2007. IEEE International Conference on* , pp.1388-1393, Dec. 2007
- [7] B. Aeyels, W. Van Petegem, J. Vander Sloten, G. Van der Perre, and L. Peeraer, "EMG-based finite state approach for a microcomputer-controlled above-knee prosthesis," *Proceedings for the IEEE Engineering in Medicine and Biology 17th Annual Conference*, vol. 17, no. 2, pp. 1315-1316, Sep. 1995.
- [8] W. S. Harwin, L. O. Leiber, G. P. G. Austwick, and C. Dislis, "Clinical potential and design of programmable mechanical impedances for orthotic applications," *Robotica*, vol.16, pp. 523-530, Sep.-Oct. 1998.

- [9] H. Herr, and A. Wilkenfeld, "User-Adaptive Control of a Magnetorheological Prosthetic Knee," *Industrial Robot: An International Journal*. 2003; 30: 42-55.
- [10] J. Furusho et al., "Development of Shear Type Compact MR Brake for the Intelligent Ankle-Foot Orthosis and Its Control; Research and Development in NEDO for Practical Application of Human Support Robot," *Rehabilitation Robotics*, 2007. ICORR 2007. IEEE 10th International Conference on , pp.89-94, June 2007
- [11] Changhyun Cho; Jae-Bok Song; Munsang Kim, "Energy-Based Control of a Haptic Device Using Brakes," *Systems, Man, and Cybernetics, Part B: Cybernetics*, IEEE Transactions on, vol.37, no.2, pp.341-349, April 2007
- [12] Jinung An; Dong-soo Kwon, "Haptic experimentation on a hybrid active/pассиве force feedback device," *Robotics and Automation*, 2002. Proceedings. ICRA '02. IEEE International Conference on , vol.4, pp. 4217-4222, 2002
- [13] Ying Jin; Furusho, J.; Kikuchi, T.; Oda, K.; Takashima, S., "A basic study on passive force display and rehabilitation system with redundant brakes," *Complex Medical Engineering*, 2009. CME. ICME International Conference on , pp.1-6, 9-11 April 2009
- [14] M. Sakaguchi, et al., "Passive force display using ER brakes and its control experiments," *Virtual Reality*, 2001. Proceedings. IEEE , pp.7-12, 17-17 March 2001
- [15] ZhiDong Wang; Fukaya, K.; Hirata, Y.; Kosuge, K., "Control Passive Mobile Robots for Object Transportation - Braking Torque Analysis and Motion Control," *Robotics and Automation*, 2007 IEEE International Conference on , pp.2874-2879, 10-14 April 2007.
- [16] N.M. Mayer, F. Farkas, and M. Asada, "Balanced walking and rapid movements in a biped robot by using a symmetric rotor and a brake," *Mechatronics and Automation*, 2005 IEEE International Conference , vol.1, pp. 345-350, 29 July-1 Aug. 2005.
- [17] Ahn Kyoung Kwan; Tran Hai Nam; Yoon Young Il, "New approach to design MR brake using a small steel roller as a large size magnetic particle," *Control, Automation and Systems*, 2008. ICCAS 2008. International Conference on , pp.2640-2644, 14-17 Oct. 2008.
- [18] B. Kavlicoglu, F. Gordaninejad, and C. Evrensel, "A Semi-Active, High-Torque, Magnetorheological Fluid Limited Slip Differential Clutch," *Journal of Vibration and Acoustics*, vol.128, issue5, pp.604-611, Oct. 2006.
- [19] K. Karakoc, E. J. Park, and A. Suleman, Design considerations for an automotive magnetorheological brake, *Mechatronics*, vol.18, issue8, Pages 434-447, Oct. 2008.

- [20] W.H. Li, and H. Du, "Design and Experimental Evaluation of a Magnetorheological Brake," *The International Journal of Advanced Manufacturing Technology*, vol.21, issue7, pp.508-515, May 2003.
- [21] Gosline, and V. Hayward, "Eddy Current Brakes for Haptic Interfaces: Design, Identification, and Control," *Mechatronics, IEEE/ASME Transactions on*, vol.13, no.6, pp.669-677, Dec. 2008.
- [22] D. Senkal, and H. Gurocak, "Compact MR-brake with serpentine flux path for haptics applications," *EuroHaptics conference, 2009 and Symposium on Haptic Interfaces for Virtual Environment and Teleoperator Systems. World Haptics 2009. Third Joint*, pp.91-96, 18-20 March 2009.
- [23] M. Gogola, and M. Goldfarb, "Design of a PZT-actuated proportional drum brake," *Mechatronics, IEEE/ASME Transactions on*, vol.4, no.4, pp.409-416, Dec 1999.

CHAPTER II

BRAKE DESIGN ITERATIONS

1. Introduction

The wafer disc brake presented in this thesis evolved over two years of research and four iterations before arriving at its final embodiment. Each of the three preceding prototypes offered useful insight regarding design concepts and components. Each iteration provided greater understanding of how to best model the device such that better predictions could be made about its performance. For these reasons, this chapter is included to impart a greater understanding of the wafer disc brake through the knowledge of its development.

2. Wafer Disc Brake Prototype 1

2.1 Design and Operation

Initially, the intended mechanism for activation (to compress a stack of friction discs) was an electromagnetic voice coil (such as a BEI KIMCO linear voice coil actuator). Before adding the complexity of electrical actuation to an unproven concept, the first prototype of the wafer disc brake was designed with manual actuation so that the multiple disc stack concept could be evaluated. As shown in Figure 2-1, the first

prototype was comprised of a simple stator body design with four cylindrical slots running lengthwise along its inside face such that rods could be inserted to serve as splines for the stator discs. A half inch diameter steel shaft served as the rotor and turned within bronze bearings held in place by top and bottom caps. The rotor shaft was keyed such that rotor discs would couple to it via a standard 1/8" key. In this configuration, 35 rotor discs and 36 stator discs—all 0.010" thick blue spring steel—were alternately coupled to their respective members and would provide a resistive torque if a compressive force was applied to the stack. To generate this compressive force, a fine-threaded lead screw was affixed to the top cap of the brake and was outfitted with a wing nut and a precision compression spring. Knowing the spring constant and the pitch of the lead screw, a predictable force could be applied to the friction disc stack via an intermediate stack compressor piece. A photograph of the first prototype wafer disc brake is shown in Figure 2-2.

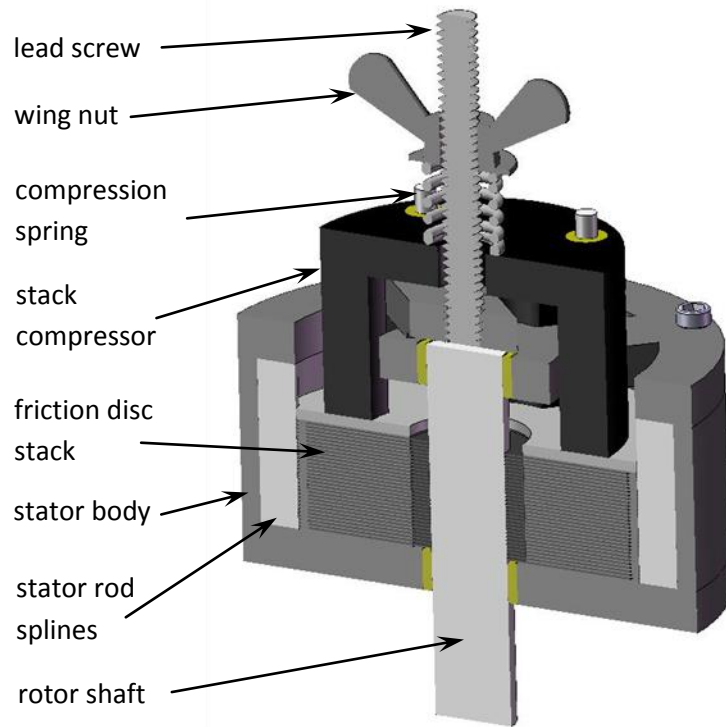


Figure 2-1. Sectioned view of wafer disc brake prototype 1.

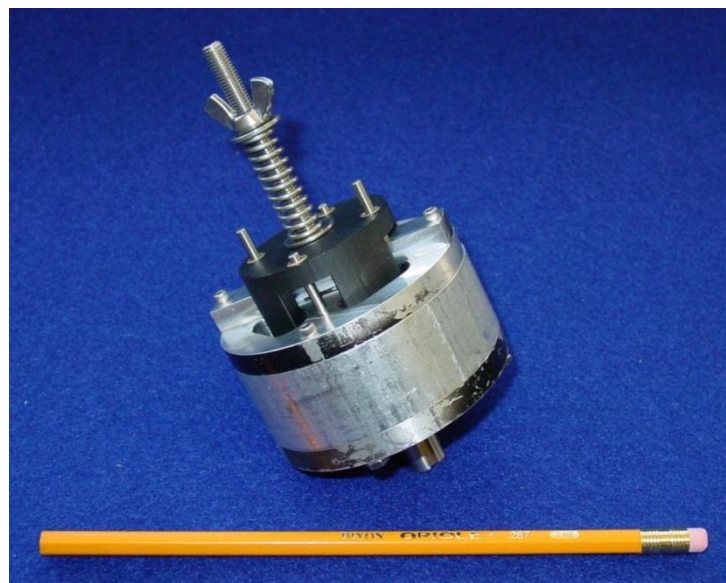


Figure 2-2. Wafer disc brake prototype 1.

The brake design was analytically evaluated to predict the expected torque output. Assuming uniform distribution of interface pressure between discs,

$$P = \text{constant} \equiv P_m \quad (2-1)$$

$$dF_f = P_m(2\pi r dr) \quad (2-2)$$

$$F_f = \int_{r_i}^{r_o} 2\pi P_m r dr = \pi P_m (r_o^2 - r_i^2) \quad (2-3)$$

$$T_{disc} = \int_{r_i}^{r_o} r \mu P_m (2\pi r dr) = \frac{2\pi \mu P_m}{3} (r_o^3 - r_i^3) \quad (2-4)$$

$$T_{brake} = \frac{2\mu F}{3} \frac{(r_o^3 - r_i^3)}{r_o^2 - r_i^2} N \quad (2-5)$$

where P , P_m is the pressure applied to each friction interface, F_f is the force of friction on one surface, r_o is the outer radius of the friction interface, r_i is the inner radius of the friction interface, T_{disc} is the resistive torque generated at each disc, μ is the coefficient of friction of the disc material, T_{brake} is the resistive torque generated by the brake, F_{stack} is the normal force applied at the interface surface, and N is the number of friction interfaces (i.e., one fewer than the total number of discs used). With an inner radius of contact of 9.53 mm, an outer radius of contact of 27.0 mm, a static friction coefficient of 0.16, 70 friction interfaces, and a maximum force provided by the spring of 80 N, the predicted maximum torque from wafer disc brake prototype 1 is 17.6 Nm.

2.2 *Finite Element Analysis*

The most significant unknown in this first wafer disc brake prototype was the performance of the discs. Of particular concern was the stress concentration at the keyway of the rotor discs (i.e., where the discs couple to the rotor shaft). A finite element analysis was conducted in CosmosExpress, a Solidworks FEA package, to determine how the steel discs would handle the high stresses generated during braking. A 90 Newton force in the plane of the disc was simulated to one of the radial keyway faces which would correspond to a 25 N-m torque distributed through the 35 rotor discs at a radial distance of 7.87 mm (i.e., the radial distance from the center of the shaft to the end of the key). In this first analysis, the disc was constrained from buckling, or “potato-chipping.” The resulting factor of safety in this first study was 1.58. A second study was conducted with the same parameters as the first with the exception of the constraint on buckling and with the normal force at the key being slightly offset by 0.005 to initiate a buckling effect. In this case, the factor of safety drops down to 0.35 and the disc fails due to the onset of buckling. Results of this analysis are shown in Figure 2-3.

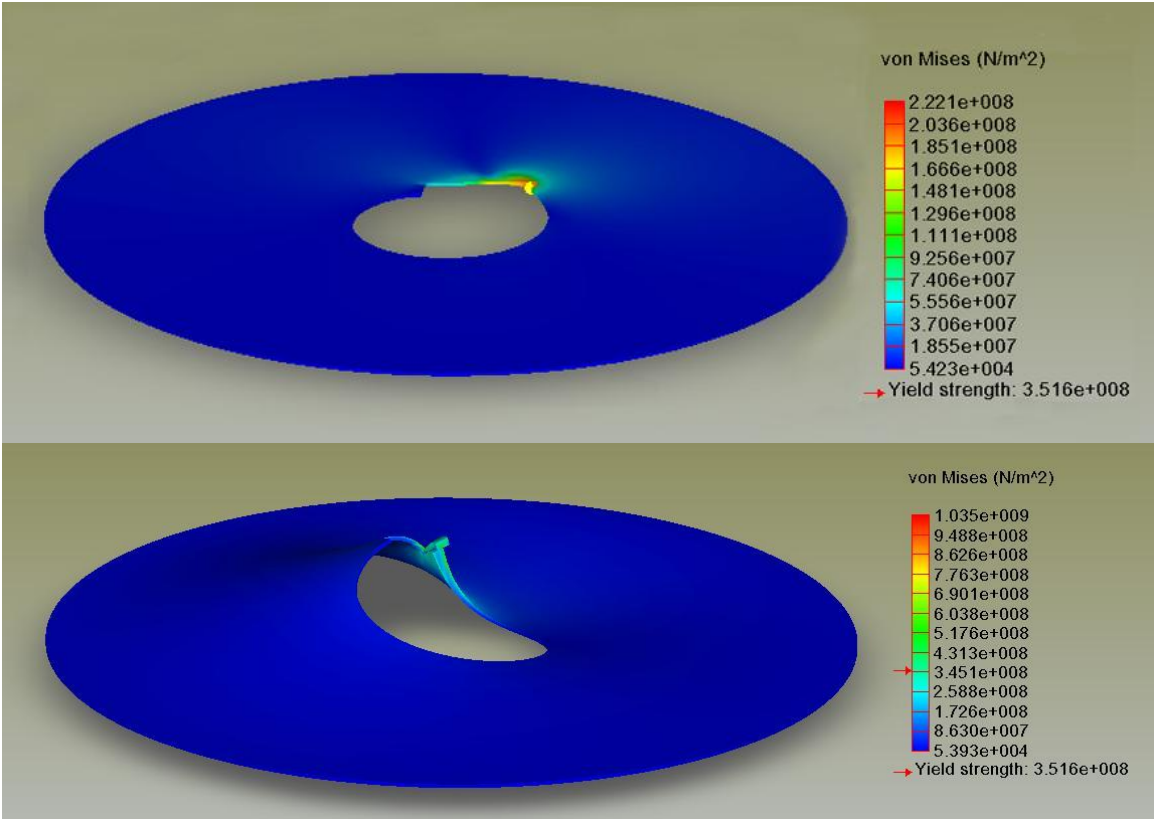


Figure 2-3. FEA stress analysis of friction discs in brake prototype 1. (a) Normal stress with disc constrained from buckling; no disc failure. (b) Normal stress with slight eccentric loading at keyway; disc failure.

2.3 Performance

An experiment was conducted to characterize the holding torque generated by the brake as it related to the compressive force applied to the disc stack. Holding torque was recorded by attaching a lever arm of known length to the rotor shaft and applying a force on the end of the arm while holding the brake stator body stationary. A digital force gage was used to measure the force applied to the arm and the maximum value was recorded just before the rotor began to turn. In the manner described in the previous section, the actuation wing nut was manually turned two revolutions at a time,

taking a torque reading at each position. The results of this experiment are presented in Figure 2-4 and show a maximum torque of approximately 25 Nm for a compressive force of about 80 N. The weight of the brake during this test was 0.79 kg (1.74 lbs) and its diameter was 76.2 mm (3.0 inches). The total thickness of the brake, including the shaft but excluding the actuation mechanism was approximately 67 mm (2.64 inches).

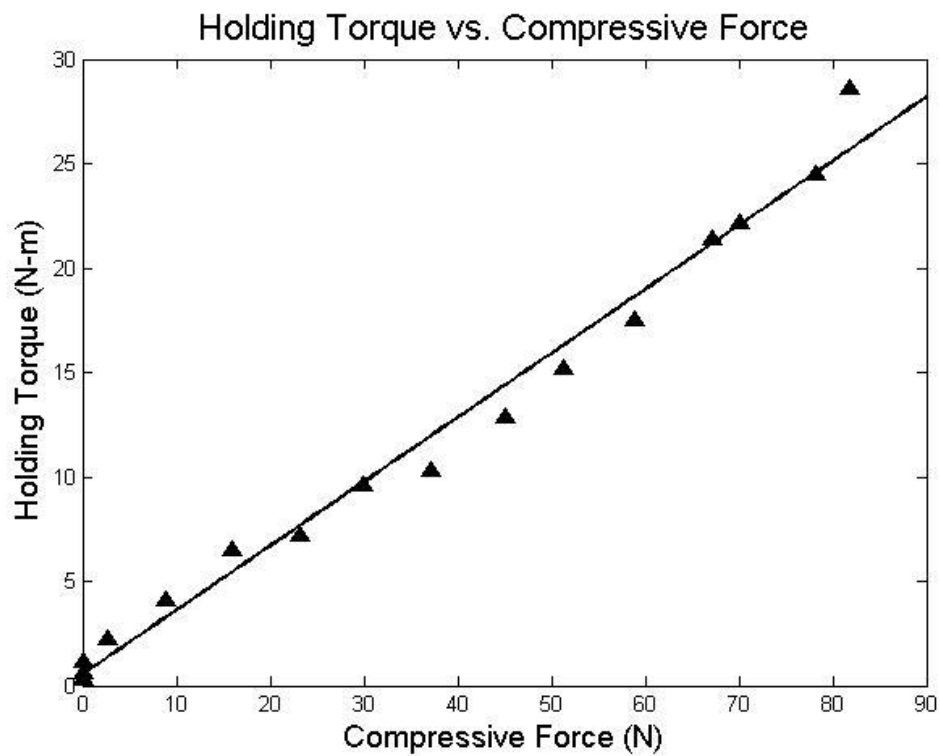


Figure 2-4. Holding torque of brake prototype 1 versus compressive force.

2.4 *Conclusions*

The first wafer disc brake prototype provided valuable insight into the feasibility of a small, lightweight, multiple thin-disc brake. Most significantly, it showed that with comparatively small actuation forces, this type of brake mechanism can produce large amounts of holding torque. Specifically, this 0.79 kg brake gave a maximum of approximately 25 N-m of torque from a compressive force of about 80 N. However, a voice coil actuator which could produce that level of force would be quite large and make the brake size and shape too restrictive for many applications. For example, BEI Kimco linear actuator LA28-22-000A is capable of producing 88 N of continuous force, but adds 1.14 kg (2.51 lbs) to the brake and extends its length by an additional 55.9 mm (2.2 inches), making the brake weight and length 1.93 kg (4.25 lbs) and 123 mm (4.84 inches), respectively. Thus, it was decided that a different actuation mechanism was needed to provide the compressive force to the disc stack rather than an electromagnetic voice coil. Additionally, it is noted that the predicted maximum value of torque from the brake was well short of the actual maximum torque from the brake. This is largely due to inaccuracy in coefficient of friction. The spring steel discs used in this first prototype have a “blued” surface finish which is easily worn off as the discs rub against each other. In friction coefficient testing, it was found that the coefficient ranged from 0.16 up to 0.29 depending on how much of the bluing had been worn off. A final observation from the finite element analysis which would later prove important was that disc buckling would likely prove the primary mechanism of disc failure, rather than strictly a tearing failure at the keys.

3. Wafer Disc Brake Prototype 2

3.1 *Design and Operation*

Having proven with the first disc brake prototype that the concept of a multiple disc friction mechanism was feasible, the logical next step was to add electronic actuation. In the second prototype, a small dc motor was used as the primary mover to turn a ball screw which generated the compressive force for the disc stack. In this way, the small torque from the motor is amplified through the small pitch of the ball screw to a large compressive force. The ball screw also plays a role in making the actuation mechanism backdrivable, such that the force on the disc stack, and therefore the torque output of the brake, remains in proportion to the current input to the motor. This backdrivability also allows the brake to be operated in a normally locked configuration, (see Fig. 2-5), in which compression springs act to compress the disc stack. The motor in this case operates in reverse to decompress the disc stack such that the output torque of the motor is inversely proportional to the input current.

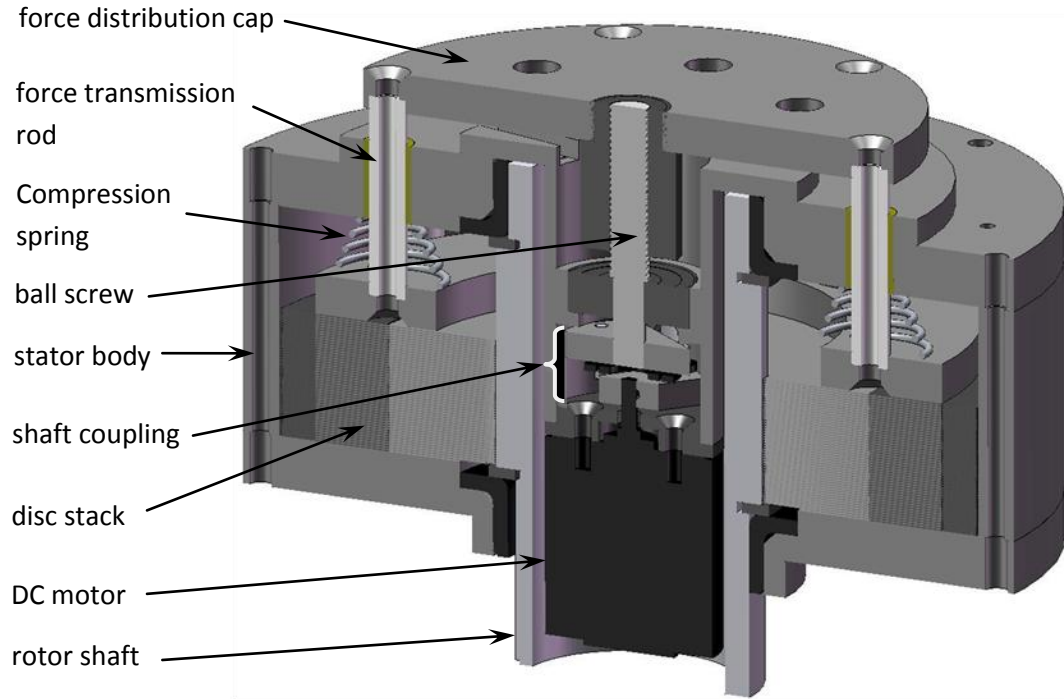


Figure 2-5. Sectioned view of the normally locked wafer disc brake prototype 2.

Consideration was given to keeping the profile of the brake as low as possible. To this end, a hollow steel shaft was chosen to function as the rotor, allowing all of the actuation components to be housed concentrically within the shaft. This larger diameter rotor shaft—as well as three added keyways—also decreased the stress on the discs at the keyways due to the larger moment arm. The use of conical springs also aided the effort to minimize brake size due to their low profile operation and ability to collapse fully. A photo of the second brake prototype is provided in Figure 2-6.

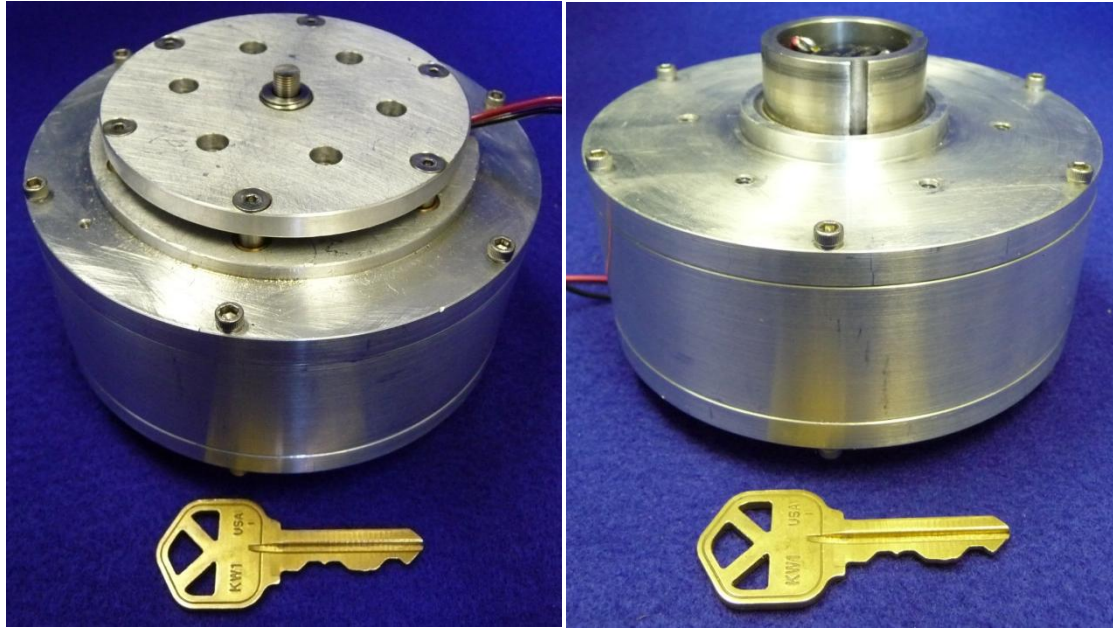


Figure 2-6. Wafer disc brake prototype 2.

A finite element analysis was conducted during the design of the second brake prototype to determine a suitable disc thickness. The larger diameter of the rotor shaft and the addition of three extra keyways permitted 0.006" thick tempered stainless steel discs to be used. This stainless steel was opted for over the blue spring steel of the first prototype due to its corrosion resistance and to avoid the inconsistency of the friction provided by the blued discs as the bluing wore off. The brake design was analytically evaluated to determine the number of discs required to achieve the 50 N-m target which was set for this brake. Examining the DC motor as the first actuation component and assuming proportionality between the motor input current and motor output torque,

$$T_{motor} = iK \quad (2-6)$$

where T_{motor} is the output torque of the motor, i is the input current and K is the motor torque constant. Assuming zero friction in the ball screw, this motor torque may be related to the linear force produced in the ball screw by,

$$Fdx = T_{motor}d\theta \quad (2-7)$$

where F is the linear force in the ball screw, and dx and $d\theta$ are finite linear and angular displacements, respectively, which are related by the pitch of the ball screw such that,

$$F = T_{motor} \frac{2\pi}{L} \quad (2-8)$$

where L is the ball screw lead (i.e., linear distance travelled per revolution). This linear force serves to compress the friction disc stack and is related by several factors to the braking torque. Taking Equation 2-5 and substituting for linear force, it is now possible to relate the brake torque directly to motor input current:

$$T_{brake} = \frac{2\mu(2iK\pi)N(r_o^3 - r_i^3)}{3L(r_o^2 - r_i^2)} \quad (2-9)$$

The Faulhaber Micromo 2224 dc motor chosen can handle a maximum continuous current of 1.2 Amps, with a torque constant of 6.92 mNm/A. The lead of the Steinmeyer miniature ball screw selected was 0.5 mm. With an outer radius of contact

of 41.3 mm, an inner radius of contact of 31.8 mm, and a coefficient of friction of 0.15, the number of discs necessary to achieve 50 N-m of holding torque was calculated to be 88. Expecting some losses, however, the brake was designed to accommodate a stack of 50 rotor discs and 51 stator discs.

3.2 *Performance*

This brake was experimentally tested in the same manner described for the first prototype, but with the brake torque output being controlled by the current input to the motor. The first tests with 101 spring tempered stainless steel discs yielded a maximum torque of 53.6, which agreed favorably with the predicted value. However, the minimum torque was very high, over 15 N-m. It was clear that this was being caused by the internal stresses in the disc stack which were causing the discs to push against each other (i.e., the discs were not completely flat, and therefore the stack tended to expand when pressure was relieved). Efforts to improve disc flatness by purchasing the steel in sheets instead of rolls and by using water-jet cutting instead of laser cutting to reduce heat effects proved ineffective. A heat treatment was then tried on the disc stack with the intention of removing residual stresses in the discs caused by cold working during creation of the steel sheet and to remove any additional warping caused by the laser cutting process used to cut the discs. The temper annealing process involved raising the temperature of the discs to 480°C (900°F), holding at this temperature for four hours, and letting the stack cool back to room temperature gradually, all while being

compressed by a 0.45 kg (1.0 lb) weight. This proved effective in increasing the flatness of the discs, as shown in Figure 2-7.

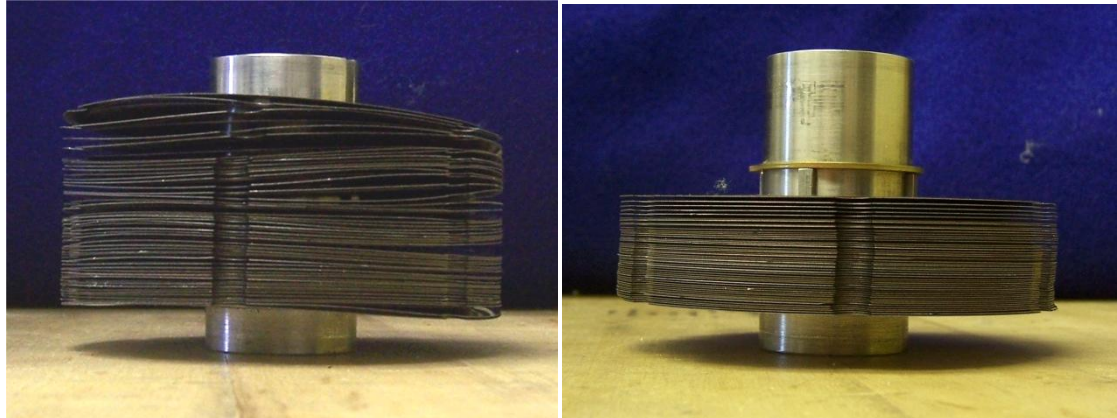


Figure 2-7. Comparison of stainless steel disc stack flatness before heat treatment (left) and after heat treatment (right).

Despite the greatly improved flatness, testing of the brake after heat treatment yielded an increased maximum torque value (122.3 N·m), and only a slightly decreased minimum torque value (12.7 N·m). Although the heat treatment was effective in flattening the discs, it had also allowed the disc surfaces to oxidize slightly, which greatly increased the coefficient of friction between discs. As this was not a desirable effect, the discs were sanded with fine grit sandpaper and the experiment was repeated. The results of these efforts were promising, with a maximum torque of 54.2 N·m and a minimum of 3.5 N·m. However, the minimum torque remained unacceptably high, and the disc stack was still expanding some when relieved, so it was decided to reduce the number of discs in the brake to 81. This combination of 81 discs which had been temper

annealed and sanded gave the best results for wafer disc brake prototype 2: a maximum torque of 50.2 N-m and a minimum of 0.62 N-m. A summary of these results is given in Table 2-1.

	101 Discs, untreated	101 Discs, temper annealed	101 Discs, temper annealed and sanded	81 Discs, temper annealed and sanded
Maximum Torque (N-m)	53.6	122.3	54.2	50.2
Minimum Torque (N-m)	> 15	12.7	3.5	0.62

Table 2-1. Summary of brake prototype 2 test results.

Dynamic operation of the brake was not evaluated due to inconsistency in ball screw backdrivability. Even though friction in the ball screw was minimal, the ultra small pitch of the thread (0.5 mm lead) hindered backdrivability, making dynamic brake operation unpredictable.

The total weight of the wafer disc brake prototype 2 was 1.12 kg (2.47 lbs), with a diameter of 102 mm (4.00 inches) and a length of 66.7 mm (2.625 inches).

3.3 Conclusions

The second wafer disc brake prototype improved upon the first prototype in several ways. Most significantly, the second prototype included the addition of

electromechanical actuation through the use of a dc motor and a ball screw transmission. Additionally, the rotor shaft was enlarged and included an additional three keyways such that the stress at the disc keyways was reduced and thinner discs could be used. Furthermore, the rotor shaft was hollow, allowing all of the actuation components to fit concentrically within the shaft to minimize the brake profile. While this design was acceptable in many aspects, it had the undesirable characteristic of exposed moving parts (the force distribution cap).

Excellent static maximum and minimum torque values were obtained from the brake after a process of heat treatment and sanding of the discs. Without this treatment, the discs proved too warped to work effectively in the brake. However, significant disc stack expansion still occurred when pressure on the stack was released; this required a thicker brake profile due to the necessity of allowing room for the stack to expand. Dynamic results were not obtained due to inconsistency in ball screw backdrivability (a problem caused partly by the small pitch of the thread).

4. Wafer Disc Brake Prototype 3

4.1 *Design and Operation*

The goal of the third wafer disc brake prototype was to minimize weight and length while still providing the torque range obtained in the second prototype. To reach

this goal, a significant change was made in the brake design concept; namely the rotor shaft was removed and the outer barrel of the brake was designed to serve as the rotating body. Sectioned views of the normally unlocked and normally locked configurations of the third disc brake prototype are provided in Figures 2-8 and 2-9. The issue of external moving parts was addressed by incorporating all force transmission members within the brake body. Of particular importance is the star-shaped compression member which transmits the force of the ball screw radially outward through its spokes to the disk stack. A key component in the third prototype which reduced the brake profile was the Portescap NuvoDisc flat “pancake” motor used to actuate the brake. Increasing the diameter of the central stator tube allowed for all the actuation components to remain within the height profile of the brake. This increased diameter also served to reduce the stress on the discs at the keyways. Further reducing this stress by including a total of 12 key splines on the stator body and 12 on the rotor barrel allowed high strength plastics to be considered for disc material. Plastic discs provide two main advantages over steel discs in this application: 1) they are much lighter, and 2) they are much flatter, even after being laser cut. A glass epoxy laminate, G-10, was chosen for its high strength and high working temperature. A finite element analysis established the thickness of the discs at 0.005 inches. GGB DU bearings were used in this prototype as they were in the previous. One further design change from the second to the third prototype involved the selection of the ball screw. Since the 0.5 mm lead ball screw had proved problematic, a THK brand 1.0 mm lead ball screw was chosen

with the expectation of improved backdrivability. A photograph of the brake is shown in Figure 2-10.

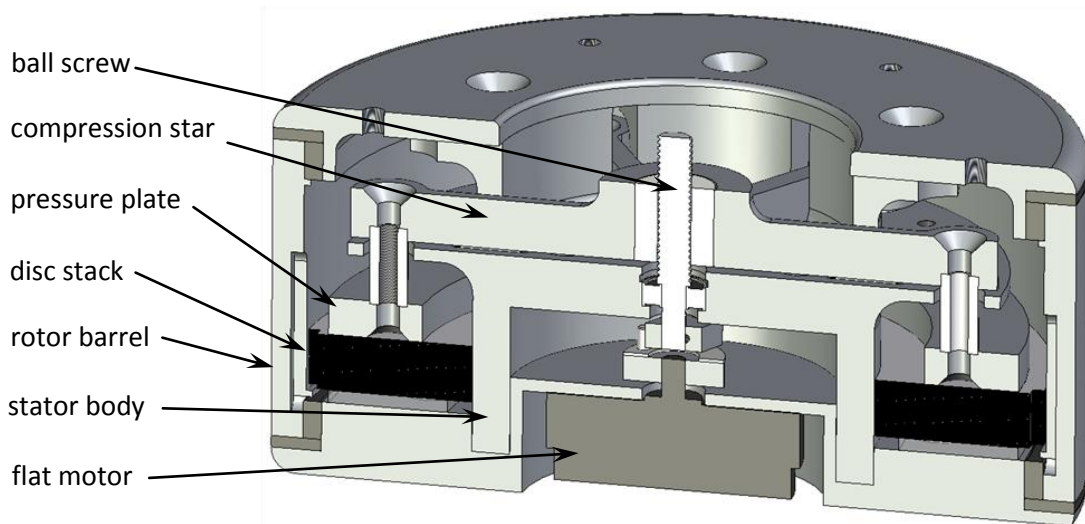


Figure 2-8. Sectioned view of the normally unlocked wafer disc brake prototype 3.

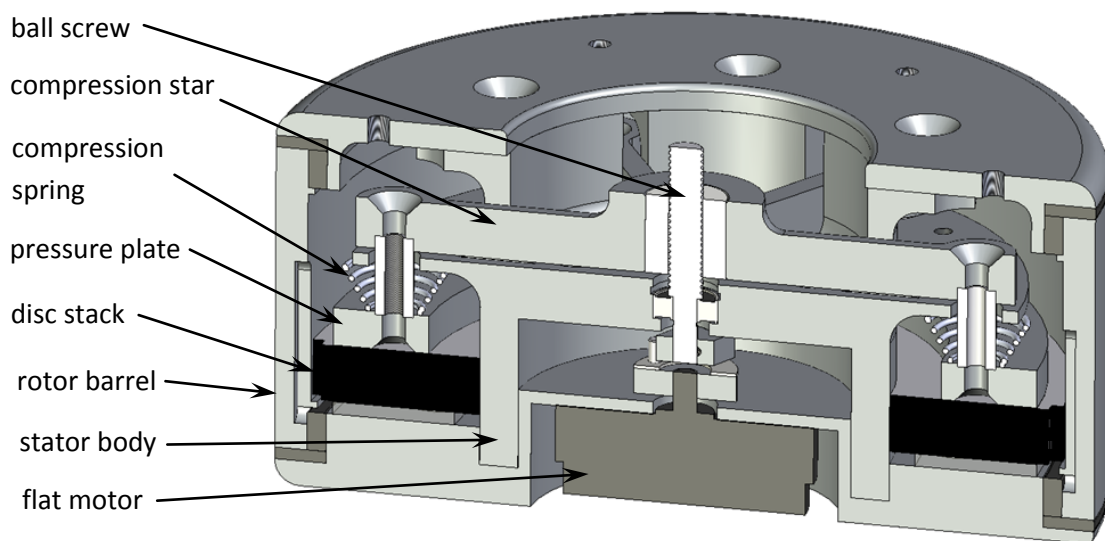


Figure 2-9. Sectioned view of the normally locked wafer disc brake prototype 3.



Figure 2-10. Wafer disc brake prototype 3.

Analytical calculations were conducted in the same manner as the previous prototype, but with new motor and ball screw specifications as well as a new coefficient of friction for the new disc material. The maximum continuous current of the nuvoDisc motor is 1.3 A, with a torque constant of 7.8 mNm/A. The Faulhaber Microlinea ED series ball screw that was chosen had a lead of 1.0 mm. From friction coefficient tests, the G-10 disc material was shown to have a static coefficient of friction of 0.21. Based on design constraints, 71 discs were able to fit in the brake. Using these values in Equation 2-9, along with the new outer radius of contact of 43.6 mm (1.72 inches) and a new inner radius of contact of 34.9 mm (1.38 inches), a maximum value of static torque was estimated at 37 N-m.

4.2 Performance

The third brake prototype was only tested in the normally locked configuration. As previously described, in this configuration compression springs do the work of compressing the disc stack and the motor performs the job of relieving the pressure. Springs were selected to provide a compressive force on the disc stack comparable to that which the motor was predicted to provide. This resulted in a maximum torque of 33 N-m and a minimum torque of 0.16 N-m. While this range was desirable, the dynamic performance of the brake was unacceptable due to significant nonlinearity in the torque response. This nonlinearity was caused by stiction in the ball screw which, in effect, made the motor underpowered for the task. The weight of the third brake prototype was 0.73 kg (1.61 lbs) with a diameter of 102 mm (4.00 inches) and a length of (1.875 inches).

The problem of an underpowered motor was addressed by replacing it with a larger motor via an external mounting piece as shown in Figure 2-11. The Maxon EC45 flat motor chosen as a replacement was rated for over five times the continuous torque of the nuvoDisc motor and was quickly shown to provide adequate power for the needs of the brake. However, while power to overcome the stiction in the ball screw was no longer a problem, the stiction still produced nonlinearities between the input current and the output torque.

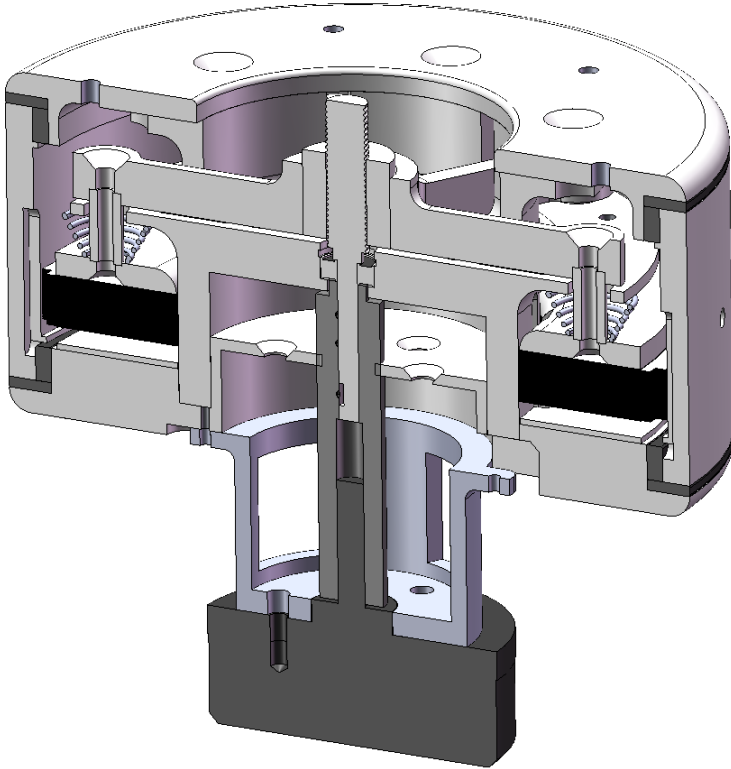


Figure 2-11. Maxon EC45 flat motor affixed on the outside of brake prototype 3.

In light of the nonlinearity in the brake mechanism, a switch was made from open loop control to closed loop control by adding strain gages to two opposing arms of the compression star (see Fig. 2-12). In this manner, utilizing a full-bridge arrangement of strain gages, force feedback on the disc stack was provided. Although the compression star had not been designed with strain gage application in mind, a strong strain signal was achieved using semiconductor gages, and good compression force tracking and step response was achieved (see Figs. 2-13 and 2-14). Despite this demonstrated ability to control the compression force on the disc stack, the dynamic torque output of the brake remained sporadic and unpredictable (see Fig. 2-15).

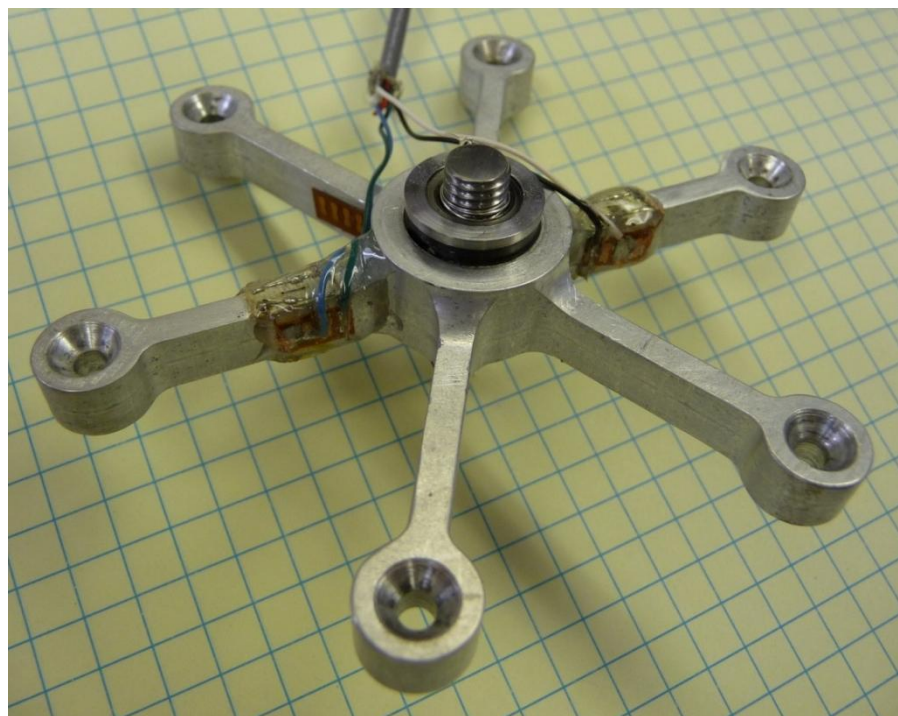


Figure 2-12. Strain gages applied to two opposing arms of the compression star to provide force feedback on the disc stack.

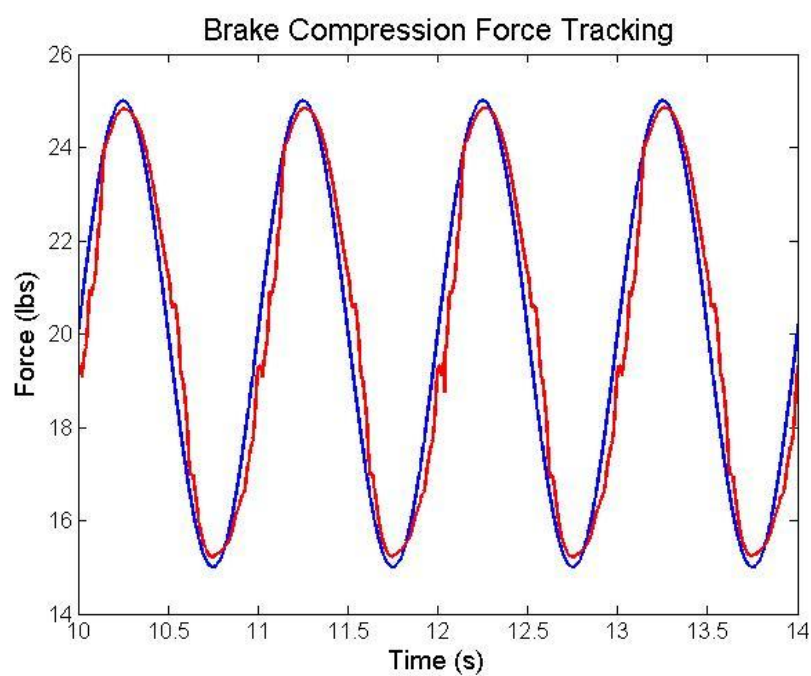


Figure 2-13. Sinusoidal compressive force tracking in brake prototype 3.

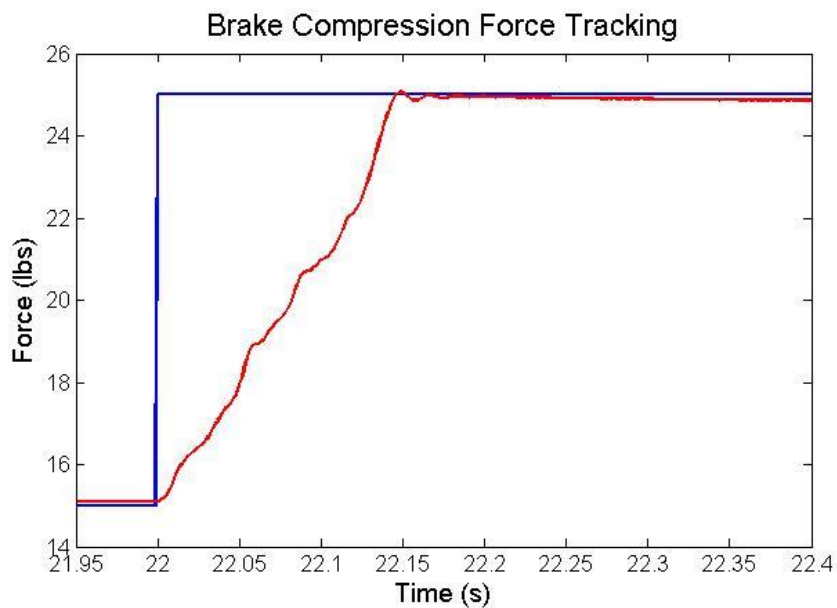


Figure 2-14. Compressive force step response in brake prototype 3.

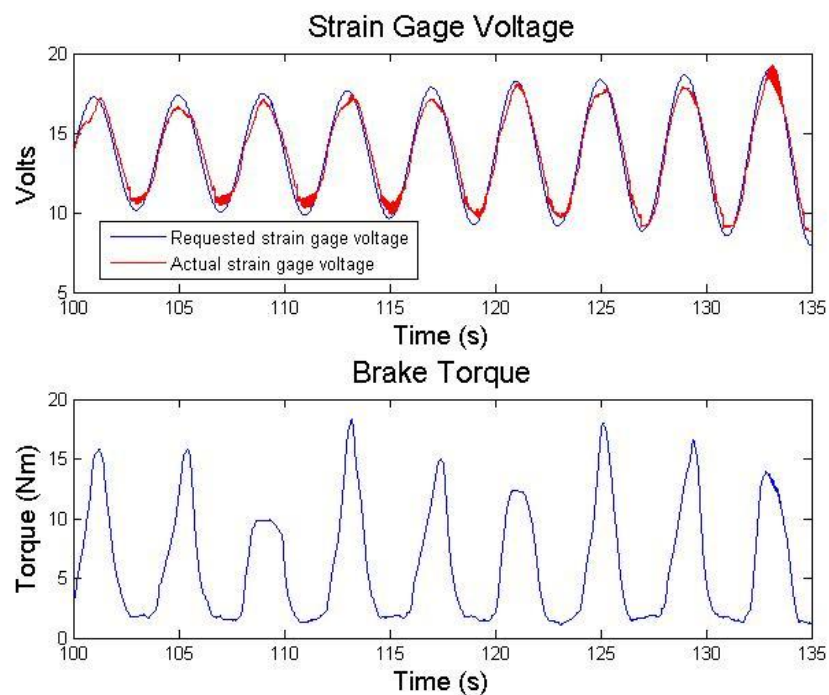


Figure 2-15. Inconsistent torque output relative to good compression force (strain gage) tracking.

4.3 *Conclusions*

Two of the three goals for the third brake prototype were accomplished. The first goal was to decrease the weight of the brake, which was accomplished by a radical design change which effectively used the outer barrel as the brake's rotor shaft. By using a new "pancake" motor, all the actuation components were within the body of the brake, reducing its profile. Additionally, a large diameter inner stator body was used and additional key splines were added so that high strength plastic discs could be used in place of steel. The second goal was to maintain a large torque output range similar to that of the second brake prototype, and this goal was also achieved. The third goal, which was not achieved, was to obtain good dynamic control over torque. Despite the effective implementation of closed-loop compression force control, unknown nonlinearities in the generation and transmission of torque within the disc stack prevented predictable torque control. One additional problem that was encountered during the testing of the third brake prototype was disc failure. Although the 0.005 inch thick G-10 discs could theoretically handle the compressive keyway stresses with an acceptable factor of safety, buckling proved to reduce the factor of safety and often caused total disc failure at the inner stator discs keyways. To address this problem, small spacer rings were placed in between each stator disc to provide support from buckling near the keyways without impeding the compression of the rotor discs against the stator discs. This added component prevented further disc keyway failures.

5. Conclusion

The evolution of the wafer disc brake through three prototypes provided the insight necessary to design the final wafer disc brake, which is presented in the following chapter. These three prototypes brought the design to a point where several key characteristics could be addressed in the final design. Primary among these desired characteristics was the ability to dynamically control the resistive torque in a consistent way. Also important was the need to provide both normally unlocked and normally locked operation robustly from the same basic design (albeit with minor modifications). Additionally, the larger motor attached to the third prototype was incorporated into the brake to maintain its low profile. Additional issues addressed in the final design included the desire for a totally enclosed design and the desire for a design which would be relatively easily manufactured and assembled.

CHAPTER III

MANUSCRIPT I: DESIGN OF A MULTI-DISC ELECTROMECHANICAL BRAKE

Ryan J. Farris and Michael Goldfarb

Department of Mechanical Engineering

Vanderbilt University

Nashville, TN 37235

Submitted as a Regular Paper to the

IEEE/ASME Transactions on Mechatronics

1. Abstract

This paper presents the design of an electrically-actuated, proportional brake that provides a significantly greater torque-to-weight ratio than a magnetic particle brake (considered a benchmark of the state-of-the-art) without sacrificing other characteristics such as dynamic range, bandwidth, or electrical power consumption. The multi-disc brake provides resistive torque through a stack of friction discs which are compressed by a dc-motor-driven ball screw. Unlike nearly all other proportional brakes, which operate in a normally unlocked mode, the brake presented here is designed such that it may be configured in either a normally unlocked or normally locked mode. The latter enables lower electrical energy consumption and added safety in the event of electrical power failure in certain applications. Following the device description, experimental data is presented to characterize the performance of the brake. The performance characteristics are subsequently compared to those of a commercially available magnetic particle brake of comparable size.

2. Introduction

Several control applications require the use of an electrically controllable proportional rotary brake (e.g., [1]-[16]). Probably the most common and thoroughly developed example of such a device is the magnetic particle brake (MPB). Magnetic particle brakes produce a steady-state resistive torque roughly proportional to the input

current. A sectioned view of a magnetic particle brake is shown in Figure 3-1. DC current applied to the brake coil induces a magnetic field which links fine ferrite particles to the rotating brake shaft. The amount of current in the coil determines the strength of the magnetic field, which in turn determines the resistive torque imposed on the brake shaft. Compared with the closed-loop control of a high-performance DC torque motor, these devices provide a relatively low electrical power and light-weight means of exerting controlled dissipative mechanical torque. Further, using an electric motor as a dissipater requires measurement of velocity, which typically contains phase lag, which in turn adds energy to the system (rather than dissipating it). A proportional brake, on the other hand, does not require velocity measurement and is guaranteed to be energetically passive.

Though the weight of a magnetic particle brake is low relative to a DC motor (for a given resistive torque), in many cases the weight remains significant. Several efforts to increase the performance of such devices have been reported, including the development of magnetorheological fluid brakes, electrorheological fluid brakes, and piezoelectrically actuated brakes (e.g., [17]-[23]). Magnetorheological and electrorheological brakes provide improved torque-to-weight characteristics relative to magnetic particle brakes, but sacrifice bandwidth and dynamic range relative to the MPB. The piezoelectrically actuated brake described in [23] offers a higher bandwidth and decreased electrical power consumption for low-frequency excitation relative to a magnetic particle brake, but provides less torque-to-weight and more torque ripple.

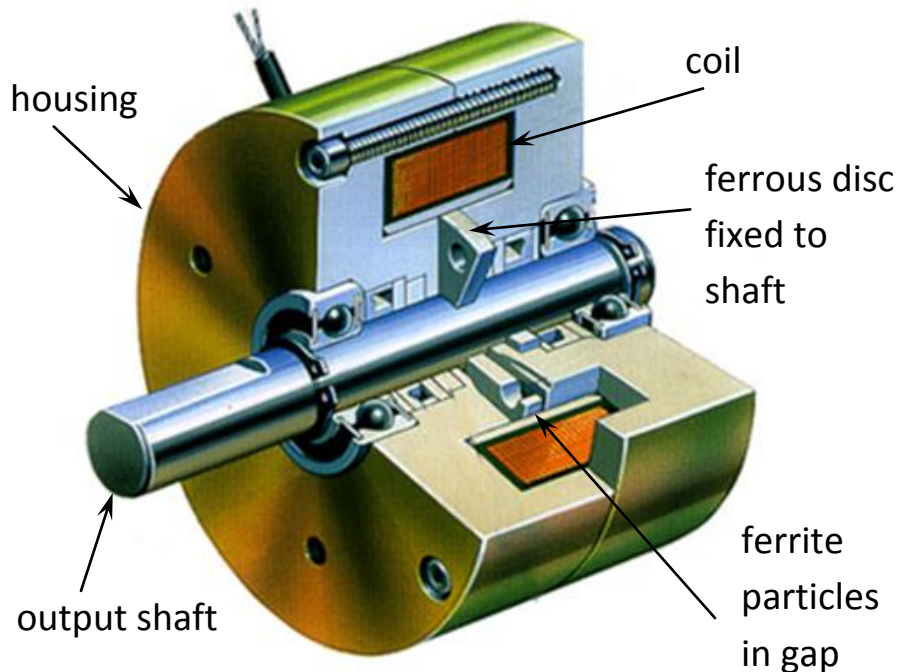


Figure 3-1. Sectioned view of a magnetic particle brake taken from PrecisionTork.com.

This paper presents the design of an electrically-actuated proportional brake that provides a significantly improved torque-to-weight ratio relative to a magnetic particle brake, while maintaining (or improving) dynamic range and response time. Importantly, unlike particle brakes, magnetorheological fluid brakes, or electrorheological fluid brakes, the proposed device can be designed in both a normally unlocked and normally locked configuration, which offers a greater number of design options for a given application. The approach utilizes a motor-driven ball screw, which compresses a

multiple-disc mechanism for resistive torque generation. Due to the amplification effects of a small ball screw lead and a large number of discs in the disc stack, the brake provides a resistive torque approximately three orders of magnitude larger than the motor torque. Due to the relatively thin discs used on the brake, the authors refer to the device as a wafer disc brake (WDB).

Note that electrically actuated multiple disc brakes and clutches are commercially available and used in heavy equipment applications (e.g., material handling). Such brakes, however, operate similarly to a magnetic particle brake, in that they utilize a stack of ferrous discs subjected to an electrically induced magnetic field. Such brakes are effective, but due to residual magnetism and sticking of plates, do not provide well-behaved proportional operation. Further, due to the nature of the attractive forces generated by a magnetic field, implementation of such brakes in a normally locked configuration would be a nontrivial task. The remainder of this paper describes the design of the (wafer disc) brake and characterizes and compares its performance to that of a commercially available magnetic particle brake of comparable size.

3. Wafer Disc Brake Design

3.1 *Brake Configuration*

The normally unlocked configuration of the WDB is shown in cross-section in Fig. 3-2. The normally unlocked brake consists of a stack of thin (0.25 mm) high-strength plastic wafers which are alternately coupled (through splines) to the brake stator and

rotor. A small brushless motor located inside the brake stator transmits a compressive force through a ball screw to the stack. Assuming relatively low friction in the ball screw, the stack is subjected to a compressive force which is proportional to the motor current. Due to the series arrangement of discs, the resistive torque on the rotor barrel is the product of the compressive force, the mean radius of contact, and the coefficient of friction, which is amplified by the number of interfaces between discs. Since the brake (as shown) contains 45 discs, the effective torque is increased by a gain of 44. Since the ball screw is back-drivable, the brake torque remains in proportion to the motor current, and thus is proportional in nature. A compression spring is located between the motor and ball screw nut to insure full torque release when no electrical power is supplied. Note that the brake as shown does not incorporate a central output shaft, as is typical in many brakes, but rather incorporates an annular rotor “barrel.” The use of an annular rotor (and the lack of a central shaft) is not fundamental to the brake design, but rather was opted for by the authors in order to better integrate the brake into a mechanism (i.e., similar to the use of a frameless motor). The WDB in its normally locked configuration is shown in cross-section in Fig. 3-3. The design of the normally locked brake is similar to the normally unlocked type, but the discs are preloaded with a compression spring. Applying current to the motor proportionally unloads the preload, such that full brake torque occurs at zero motor current, and minimum brake torque occurs at full motor current. Since the ball screw is back-drivable, the brake torque remains in inverse proportion to the motor current. Both configurations of the WDB appear the same from the outside. A photo of a fully functional wafer disc brake (which

has been alternately configured in both a normally locked and normally unlocked configuration) is shown in Fig. 3-4.

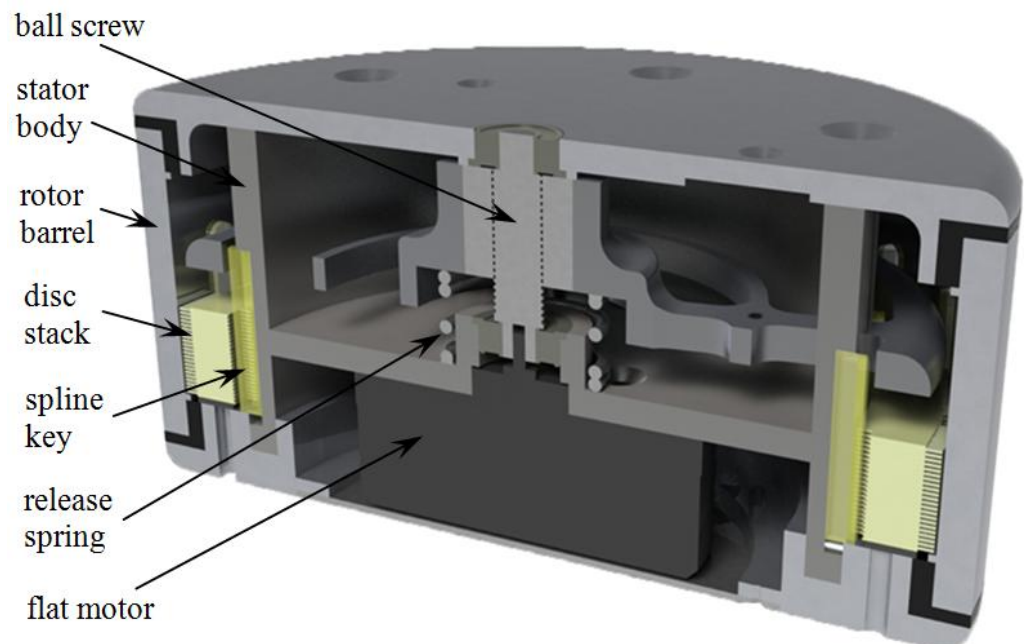


Figure 3-2. Sectioned view of normally unlocked wafer disc brake.

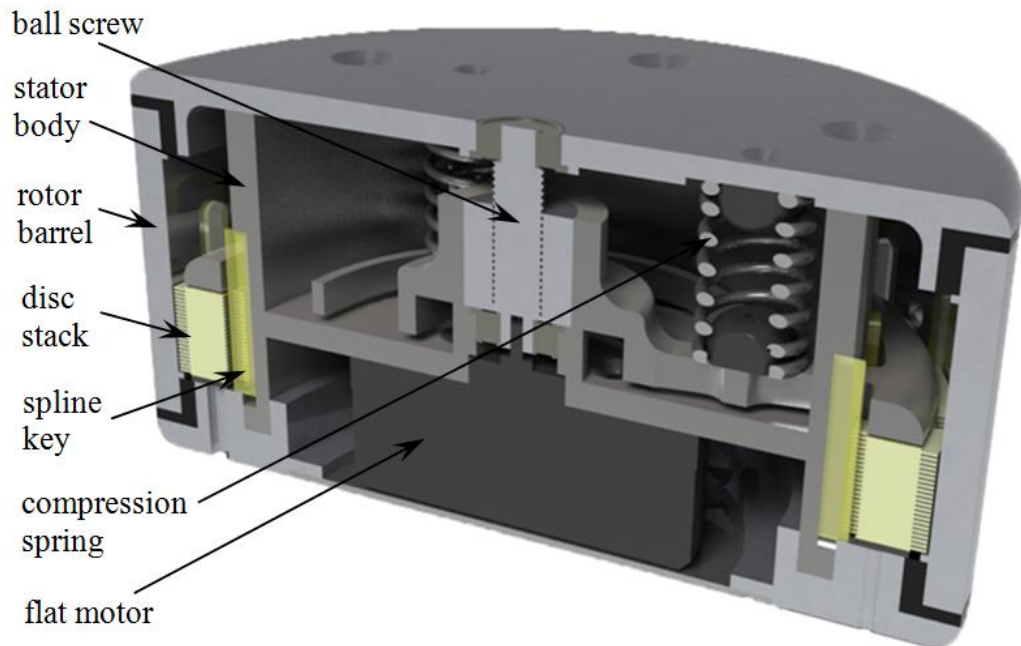


Figure 3-3. Sectioned view of normally locked wafer disc brake.



Figure 3-4. Fully functional wafer disc brake.

3.2 Design Relationships

One of the primary design objectives for the WDB is to generate a high torque output. As such, the relationships that govern the resistive torque capability are described here. We assume that the compressive force applied to the annular discs is evenly distributed, and thus that the compressive force results in a constant pressure applied across the annular area of the disc:

$$F = \pi P(r_o^2 - r_i^2) \quad (3-1)$$

where F is the compressive force, P is the pressure between discs, and ri and ro are the inner and outer radii of the discs, respectively. Assuming Coulomb friction between the discs, the resistive torque generated by the one disc interface is given by:

$$T = \int_{r_i}^{r_o} r \mu P (2\pi r dr) = \frac{2\pi \mu P}{3} (r_o^3 - r_i^3) \quad (3-2)$$

where T is the resistive torque and mu is the coefficient of friction (either static or dynamic, depending on whether or not the discs are moving relative to each other). Combining (3-1) and (3-2), and assuming a stack of discs, the resistive torque is given as a function of the compressive force by:

$$T = \frac{2\mu FN}{3} \frac{(r_o^3 - r_i^3)}{r_o^2 - r_i^2} \quad (3-3)$$

where N is the number of disc interfaces (i.e., between stator and rotor). Assuming that torque is proportional to current in the DC motor, and neglecting friction in the ball screw, the resistive torque can be written as a function of motor current as:

$$T = \frac{2\mu N k_t}{3l} \frac{(r_o^3 - r_i^3)}{r_o^2 - r_i^2} i \quad (3-4)$$

where l is the ball screw lead, k_t is the motor torque constant, and i is the motor current. Note that, in the case of a return spring (see Fig. 3-2), the resistive torque is somewhat less than that described by (3-4), since the compressive force F is decreased by the spring stiffness. As indicated by (3-4), maximizing the resistive torque requires maximizing both the output and input radii (e.g., a narrow ring will provide more torque than a wide ring, provided they have the same outer radius). Thus, a tradeoff becomes apparent between maximizing torque and maximizing surface area (which minimizes disc wear). However, the significant benefit of this dimensional phenomenon for this application is that rings may be used instead of solid discs. This fact combined with the

design of the brake such that the outer barrel serves as the rotating body (i.e., does not require a central shaft) allows all of the actuation and transmission components to be located concentrically within the disc stack, enhancing compactness of the design. The compression ring was designed with the aid of a finite element analysis of stress such that it was lightweight, while still maintaining sufficient strength to reliably transmit the forces from the ball screw to the disc stack. For a more detailed treatment of torque estimation from annular contact disc brakes and clutches, see [24].

A 30 W Maxon EC45 DC brushless flat motor was chosen to actuate the brake due to its thin profile and high torque. Importantly, the lack of a gearhead and the use of a ball screw instead of a lead screw allow the motor to remain fully backdrivable. As such, the brake is able to return to either its normally unlocked or normally locked state when the electrical power input is turned off (i.e., when the brake is powered down). A Faulhaber Microlinea ED513 ball screw was chosen based on its small lead (1.25 mm) and low profile ball nut design.

Selection of disc material and disc thickness was accomplished by a finite element analysis of disc stress and iterative testing of several different candidate materials. Key factors in material selection were high tensile strength, high coefficient of friction, and the ability to remain flat after fabrication. While a variety of materials have been shown to work effectively in the brake, including stainless steel, polyetherimide (Ultem), and polyetheretherketone (PEEK), the material chosen based on weight and performance for the brake characterization was wear resistant G-10

phenolic. This ultra high strength glass-epoxy laminate exhibits high dimensional stability over temperature, provides a relatively high coefficient of friction, and is treated to resist wear. The disc thickness was chosen to be 0.25 mm (0.010 in), which provided sufficient rigidity to resist buckling near the spline interfaces, which was found to be the primary mode of failure in thinner discs. The splines themselves were designed as keys inserted into keyways for ease of manufacturing. As an added benefit, this allowed flexibility in the selection of the materials used for the keys. In the design shown in Fig. 3-4, Ultem was chosen for the key material, which has a high tensile strength, a high maximum operating temperature, and an appropriate hardness to interface with the G-10. The geometrical configuration of the brake prototype, along with the values for the other design parameters given in (3-4), are given in Table 3-1. For the normally unlocked configuration, a return spring of stiffness $k=3.35$ N/mm was utilized, which deflects approximately 13 mm before the pressure plate contacts the disc stack, and thus the compressive force provided by the motor is decreased by approximately 44 N. Accounting for the force required to compress the spring, (4) indicates a predicted maximum static and dynamic torque of the wafer disc brake in the normally unlocked configuration of 83.1 N·m and 54.8 N·m, respectively.

Design Variable	Value
k_t	25.5 mN-m/A
i_{\max}	2.14 A
l	1.25 mm
μ_s	0.194
μ_k	0.128
N	44
r_i	39.4 mm
r_o	44.9 mm

Table 3-1. Results of the analytical and experimental design optimization.

3.3 *Special Considerations for the Normally Locked Design*

While operating in the normally locked configuration, the motor acts to release rather than impose compressive force on the disc stack, which essentially decreases rather than increases the resistive torque. In this case, a set of compression springs provides the compressive force on the disc stack. To release the brake, the electric motor must provide (through the ball screw) enough force to match the compressive force of the springs on the stack, and additionally to compress the springs another approximately 3 mm (i.e., the disc stack is not perfectly flat, and expands slightly axially when the compressive force is relieved). The maximum force applied to the stack by the springs must therefore be less than the maximum force applied by the motor and ball screw in the normally unlocked case, so that the brake can be fully unlocked. To minimize the amount of motor torque required for disc expansion, the brake design maximizes the linear space available to the springs such that the longest springs possible can be employed. Taking this approach allows the spring constant to be minimized (for

a given nominal stack force) which reduces the rate of increase of force as the springs are being compressed. Based on the parameters listed in Table 3-1, the motor and ball screw transmission can generate a maximum force of 274 N. The springs selected for the normally locked brake have a spring constant of 3.2 N/mm, and as such a compression of 3 mm (i.e., to fully relieve the disc stack) requires a force of approximately 10 N. Thus, the normally locked brake can apply a maximum of 264 N to the disc stack in the unpowered state, which is approximately 3.5% less than that of the normally unlocked brake at maximum power. Thus, the maximum static and dynamic torque for the normally locked brake in the unpowered state is predicted to be 80.2 N-m and 52.9 N-m, respectively.

4. Brake Control

Based on the idealized steady-state relationship described by (3-4), control of the current in the brushless motor would also provide control of the steady-state resistive brake torque. Despite this, the dynamic relationship between motor current and resistive brake torque is more complex, and includes the inertial effects of the ball screw and motor rotor, Coulomb friction in the transmission, and stiffness of the return spring and disc stack. The latter two physical effects constitute non-smooth nonlinearities, which complicate the open-loop control of brake torque. The non-smooth nature of Coulomb friction is evident. The non-smooth nature of the “load” stiffness is due to the fact that the discs are not perfectly flat, and as such, three distinct

load stiffnesses are present. Prior to contact with the discs, the load stiffness consists only of the return spring; once contact is made with the discs, the load stiffness is the combined effect of the return spring and the compliance of the non-flat discs; finally, once all discs are flattened by the compressive force of the motor/ball screw, the load stiffness increases considerably (i.e., the stiffness is essentially that of the “solid” annular disc stack). The load stiffness therefore can be modeled as piecewise linear stiffness consisting of three regimes: the non-contact regime (return spring only), the flattening regime, and the solid stack regime. As a result of these non-smooth nonlinearities, open-loop control failed to provide desirable control performance, in terms of accuracy and bandwidth. In order to improve torque tracking, an inner servo control loop was first added around the brushless motor, as shown in Fig. 3-5(a). This inner loop serves to compensate for the inertial dynamics and Coulomb friction in the transmission. Further, by providing improved output disturbance rejection, the inner loop mitigates the effects of the varying load stiffness on the stability of the closed loop. Note that, since the brushless motor incorporates Hall effect sensing for electronic commutation, implementation of the inner loop did not require the addition of any sensors. With the inner loop in place, accurate and robust tracking of the pressure plate motion is provided. However, due to the aforementioned tripartite stiffness, control of pressure plate motion does not provide known control of the compressive force. If the relationship between pressure plate motion and the compressive force were well characterized, the force could be controlled in an open-loop manner. However, there would still exist a significant nonlinearity between the compressive force and the

resistive torque, due to the nonlinear friction characteristics in the discs. As such, a resistive torque control outer loop was implemented around brake output torque, as shown in Fig. 3-5(b). Note that the implementation of the outer loop does require brake torque sensing. As shown subsequently, however, accurate and high bandwidth control of magnetic particle brake also requires a similar closed loop around the brake torque.

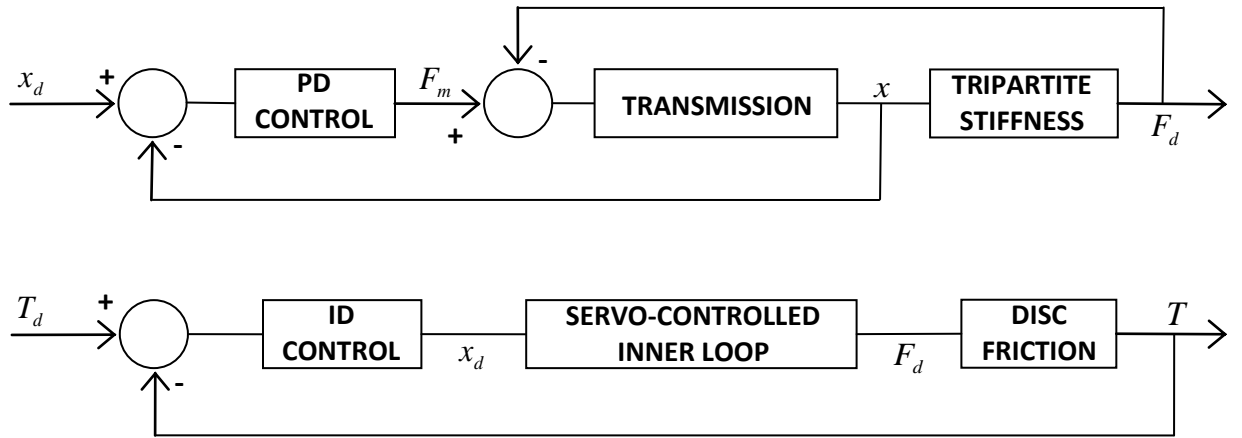


Figure 3-5. Schematic of wafer disc brake controller. (a) Servo control inner loop. (b) Torque control outer loop.

5. Performance Characterization

The wafer disc brake was tested in both operational configurations (normally unlocked and normally locked). The experimental setup used to test the brake torque is shown in Fig. 3-6. The brake barrel was driven at a constant rate with a DC motor (Kollmorgen model U12M4H) which was connected to the brake through a 90:1 transmission, in order to generate sufficient torque to drive the brake. Note that

resistive torque can only be measured when the brake shaft is moving. An encoder attached to the motor provided for closed-loop feedback control of motor velocity, so that velocity remained essentially constant, despite variation in brake torque. Brake torque was measured with a rotary torque transducer (Interface model T8 ECO) mounted between the motor and brake.

Figure 3-7 shows the maximum and minimum (low-end) dynamic (i.e., when the brake shaft is rotating) steady-state torques of the WDB, measured at a rotational speed of 20 rev/min (RPM). The average maximum torque of the brake was 30 N-m (265 in-lbs) with approximately 5% torque ripple. This maximum torque was lower than that predicted in Section II (i.e., approximately 55% of that predicted by the equations). However, torque values up to 40 N-m were achieved during sinusoid tracking trials. This indicates that in addition to the static or dynamic state of the brake rotor, maximum torque is affected by static friction (or stiction) when the ball screw is motionless. Thus, for the normally unlocked brake, the maximum average dynamic friction was 30 N-m when approached quasi-statically and 40 N-m when approached dynamically. The maximum static torque of the normally unlocked brake was 73 N-m. These values show better agreement with the expected values of 55 N-m and 83 N-m and the remaining difference may be attributed largely to uncertainty in the values for static and dynamic coefficient of friction for the G-10 disc material. The average minimum torque was 0.40 N-m (3.5 in-lbs), giving a dynamic range of approximately 1:100. The maximum dynamic torque of the normally locked brake was unable to be measured in either of the two ball screw operational regimes due to insufficiency in the

brake dynamometer. That is, both values were greater than 50 N-m, which is the maximum torque the experimental setup could measure under continuous rotation. The static torque was determined (as was the case for the normally unlocked brake) by providing manual assistance to increase the dynamometer torque to the brake and was measured at 74 N-m. As discussed previously, the normally locked brake torque was predicted to be slightly lower than that of the normally unlocked brake. This deviation from the predicted results is likely also explained by the ball screw friction exhibited between static and dynamic performance.

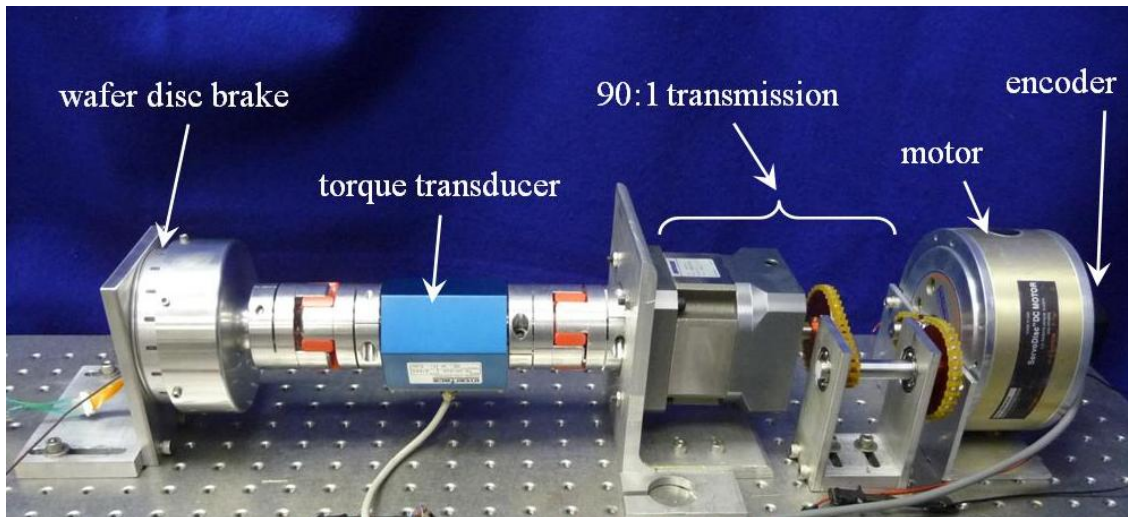


Figure 3-6. Experimental setup for testing of the wafer disc brake. Note that, since the output of the WDB is a barrel rather than a shaft, the brake is connected to the setup through a adapter, which transmits torque from the barrel to a central shaft.

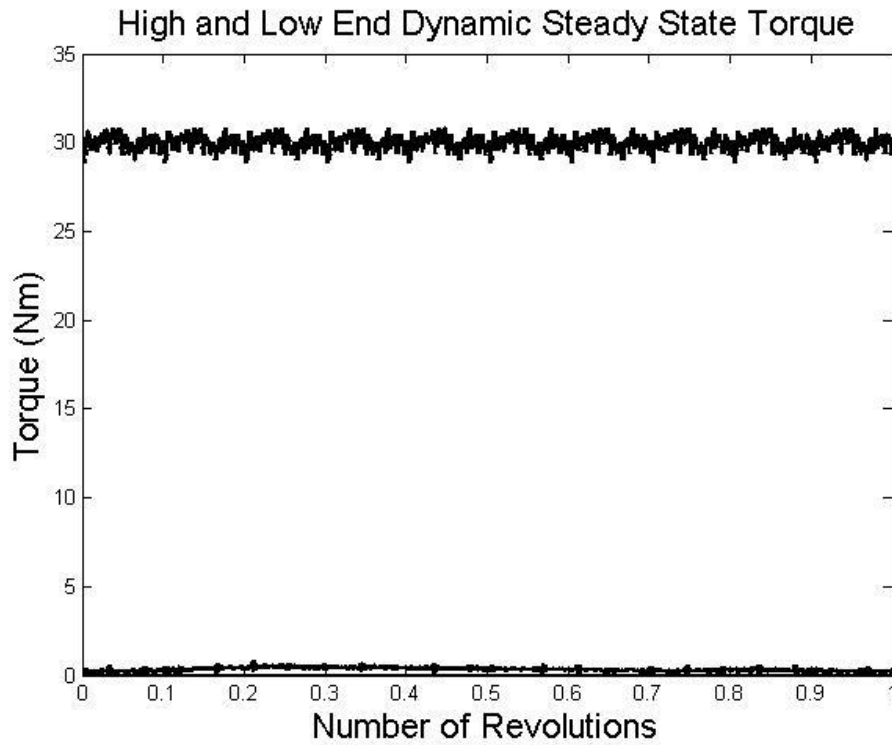


Figure 3-7. Maximum and minimum dynamic wafer disc brake torque in normally unlocked configuration for one revolution at a speed of 20 rev/min.

Figures 3-8 and 3-9 show sinusoid tracking capabilities of the normally unlocked and normally locked brake, respectively, for a peak-to-peak amplitude of 20 N-m, which is 50% of the full dynamic range of the normally unlocked brake. Figures 3-10 and 3-11 show rising and falling step responses for each brake configuration, also with a 20 N-m amplitude. Defining rise time as the amount of time required after a step command has been issued for the response to rise to 90% of the final steady-state step value, and the fall time as the reverse, the wafer disc brake demonstrates a rise time of 43 msec and a fall time of 39 msec in the normally unlocked configuration and 53 msec and 39 msec, respectively, in the normally locked configuration. Bandwidth plots for sinusoidal tracking of 20 N-m peak-to-peak commands are provided for each brake configuration

in Figs. 3-12 and 3-13, which indicate a -3 dB bandwidth of 11 Hz in the normally unlocked case and 10 Hz in the normally locked case.

An experiment was conducted to determine the power dissipation capacity of the wafer disc brake, the results of which are shown in Fig. 3-14. A thermocouple was connected inside the body of the brake to monitor the temperature. The brake speed and torque were incrementally increased and held for five minutes at a given power level before the brake temperature was recorded. Due to limitations in power generation from the dynamometer (Fig. 3-6), data could only be gathered for power dissipation up to 55 W (see Fig. 3-14). As such, based on this data, the temperature for increasing power dissipation was projected (using the quadratic trend indicated in the data). Based on these projections, power dissipation of 125 W would produce an internal brake temperature of 120 C (250 F), which is the maximum operating temperature of the brushless DC motor. It should be noted, however, prototype presented herein was not configured to maximize power dissipation, and as such, it is expected that some minor modifications (such as adding vents to the brake body) would result in improved capability for power dissipation.

An experiment was also conducted to determine the rate of wear of the discs. Specifically, the brake was run at a constant speed and torque over a given length of time, and the height (or thickness) of the disc stack was measured both before and after the experiment. The energy dissipation was measured by the dynamometer (based on shaft torque, speed, and duration of the experiment). Based on these measurements,

the rate of wear of the discs was determined to be 3.7 microns per kJ of energy dissipation. Based on the dimensions of the brake and the length of travel along the ball screw, the disc stack could tolerate approximately 1.5 mm of wear before performance would begin to degrade. For the case of G-10 discs, this equates to approximately 400 kJ of energy dissipation. If wear is of particular concern for a specific application, other disc materials could be chosen. For example, replacing the G-10 discs with a set of stainless steel discs would presumably provide greatly increased wear resistance, but would increase the brake weight from 0.67 kg to 0.81 kg.

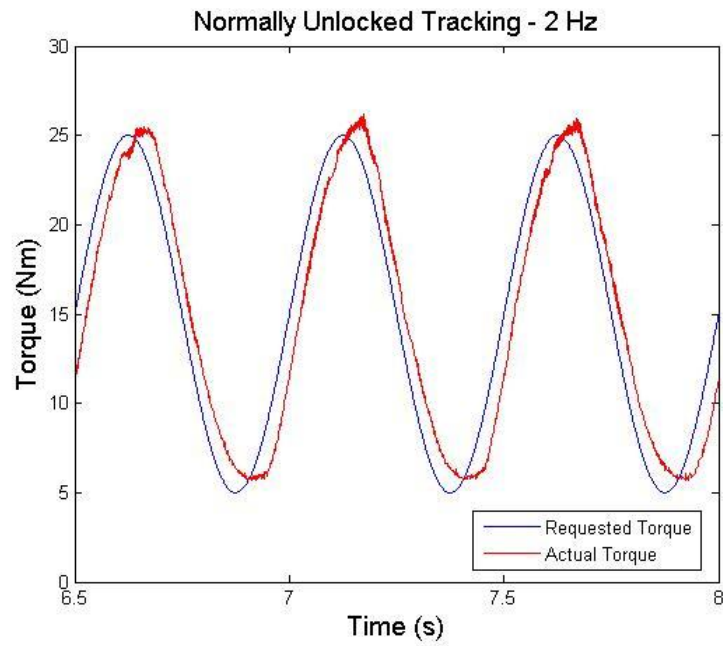


Figure 3-8. Normally unlocked brake sinusoid tracking with a peak-to-peak amplitude of 20 N-m (50% of full dynamic range).

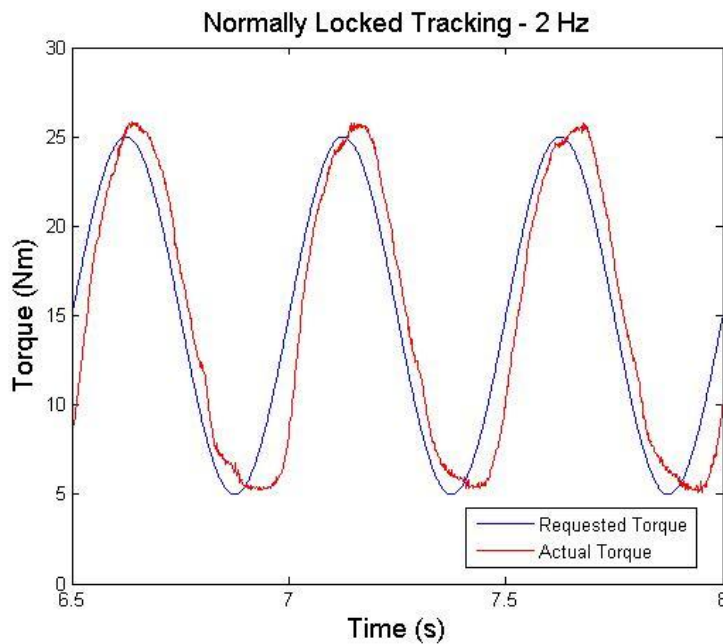


Figure 3-9. Normally locked brake sinusoid tracking with a peak-to-peak amplitude of 20 N-m (50% of full dynamic range).

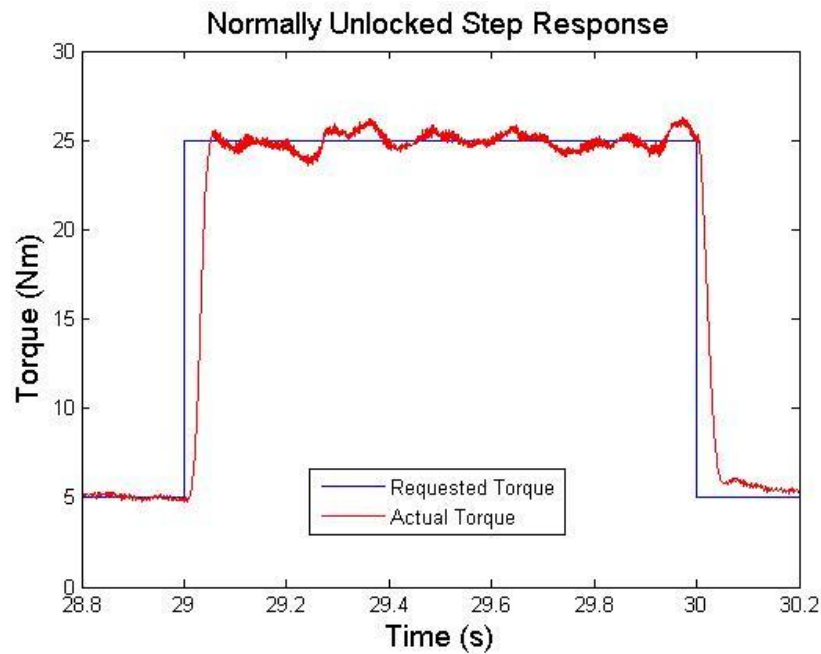


Figure 3-10. Normally unlocked brake rising and falling step response with an amplitude of 20 N-m (50% of full dynamic range).

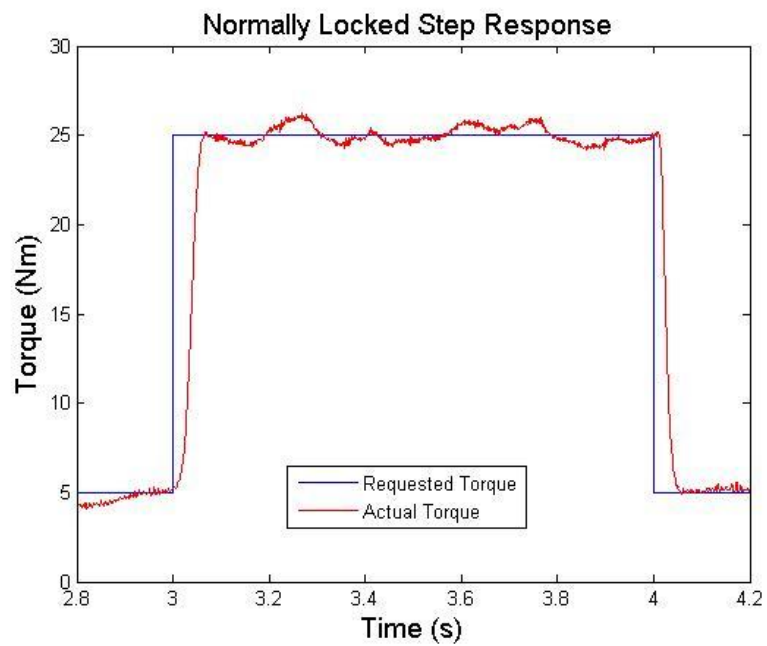


Figure 3-11. Normally locked brake rising and falling step response with an amplitude of 20 N-m (50% of full dynamic range).

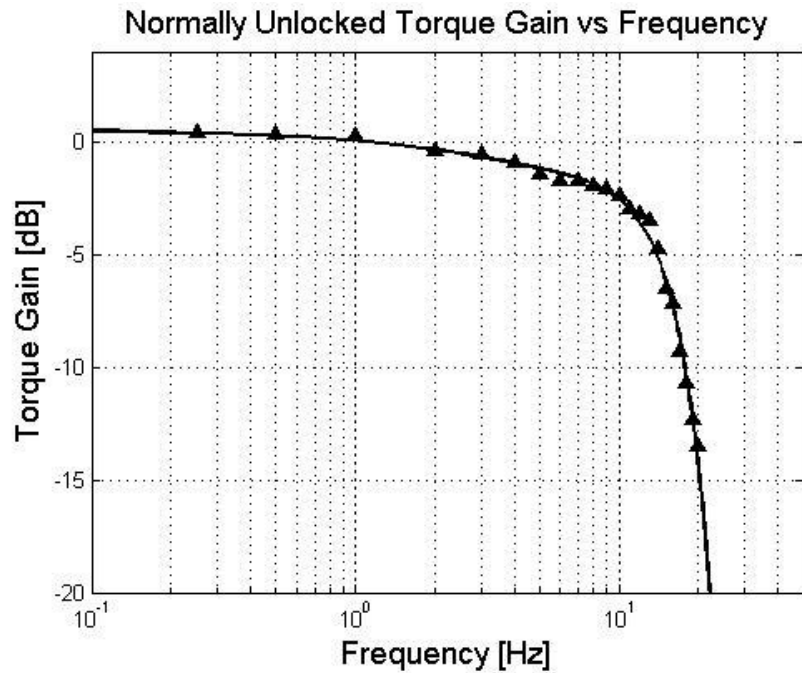


Figure 3-12. Normally unlocked torque gain vs. frequency for 20 N-m peak-to-peak oscillations (50% of full dynamic range) indicating a bandwidth of 11 Hz.

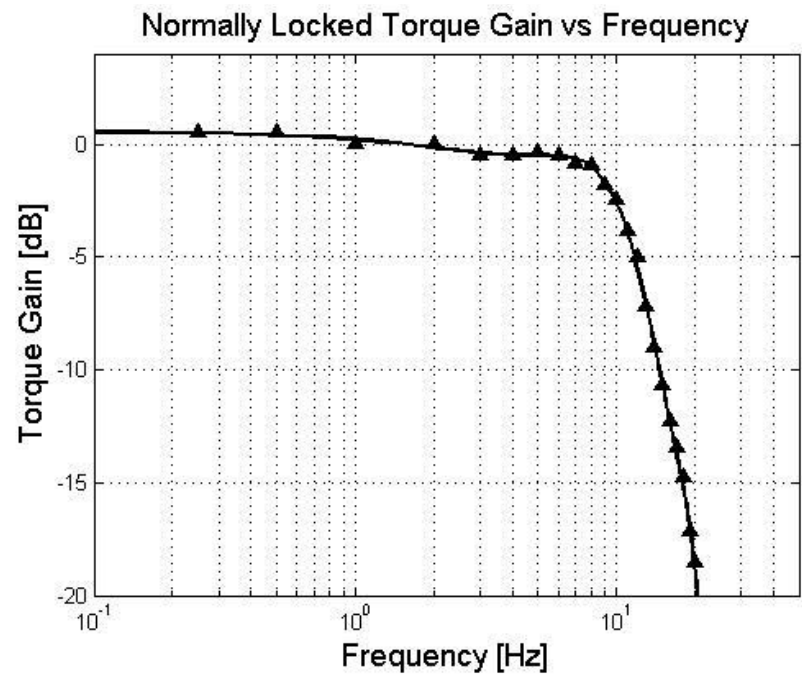


Figure 3-13. Normally locked torque gain vs. frequency for 20 N-m peak-to-peak oscillations (50% of full dynamic range) indicating a bandwidth of 10 Hz.

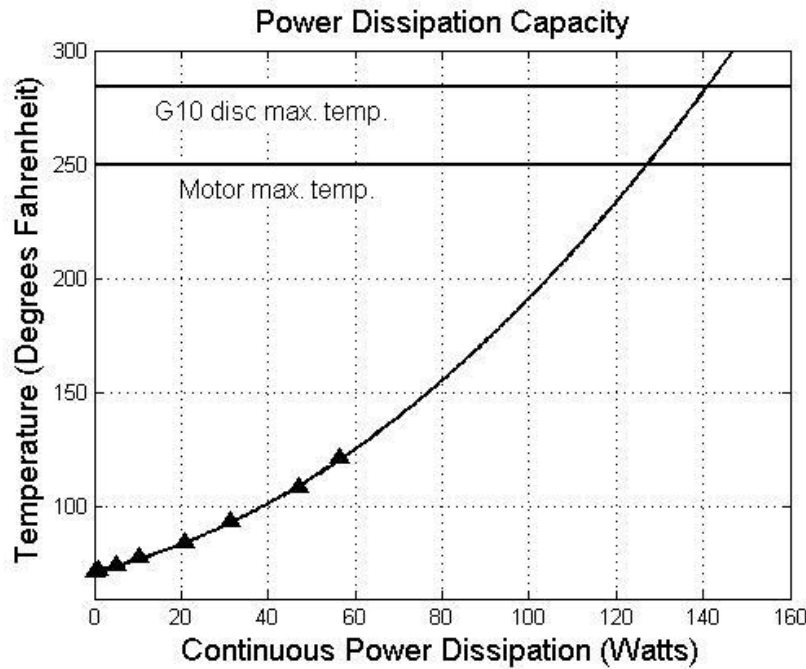


Figure 3-14. Wafer disc brake power dissipation capacity based on maximum permissible temperature, predicting a maximum power dissipation level of 125 W.

6. Comparison of Wafer Disc Brake and Magnetic Particle Brake

To the performance of the wafer disc brake in context, the performance characteristics were compared with those of a commercially available magnetic particle brake of comparable size. The particle brake utilized for the comparison was a Placid Industries model B115, which measures approximately 12.0 cm in diameter by 6.7 cm in length, as compared with the wafer disc brake which measures 10.2 cm in diameter and 4.8 cm in length. While possessing a similar size, it should be noted that the MPB has a mass of over five times that of the wafer disc brake, weighing 3.63 kg compared to 0.67 kg for the wafer disc brake.

The most obvious advantage of the wafer disc brake is the high torque capability relative to its weight. The 0.67 kg WDB provides a maximum dynamic torque of 40 N-m while the 3.63 kg MPB only provides 13 N-m. This gives the WDB a dynamic torque-to-weight ratio of about 60 compared to that of the MPB which is about 3.6. Thus, the wafer disc brake offers a torque-to-weight ratio of over 17 times that of a comparably sized magnetic particle brake. Additionally the WDB also provides a greater dynamic range, specifically 1:100 compared to the MPB's dynamic range of 1:46.

Figure 3-15 shows the step responses of both the wafer disc brake and the magnetic particle brake. Both operational modes of the WDB are represented and both control modes (open and closed-loop) of the MPB are represented. The rise times of the normally unlocked and normally locked brake (as previously presented) are 43 and 53 msec, respectively. The open-loop controlled MPB rise time is 420 msec, and the closed-loop MPB rise time is 43 msec. It should be noted, however, that the WDB step represents 20 N-m, while the MPB step represents 6.5 N-m of torque (i.e., both were characterized at 50% of their respective ranges). Thus, the WDB exhibits similar response speed to the MPB, but would be significantly faster if characterized in terms of a torque slew rate. The bandwidth of the MPB for tracking of steady-state sinusoidal commands (of 50% full scale torque) is 2 Hz and 22 Hz, respectively, for the open-loop and closed-loop controlled MPB. Thus, while the rise times of the WDB brakes are comparable to the closed-loop MPB, the latter demonstrates a higher bandwidth than the closed-loop controlled WDB (although both are on the same order).

As mentioned previously, a potential advantage of the WDB is a reduction in electrical power consumption for a given resistive torque. The steady-state power consumption for the WDB normalized by output resistive torque is 0.26 and 0.22 W/N-m for the normally unlocked and normally locked brakes, respectively. The MPB requires 0.87 W/N-m, and thus the WDB requires approximately one third the electrical power of the MPB for a given output resistive torque. Further, as previously stated, the normally locked version of the WDB may save additional power in cases that require greater than 50% duty cycle of resistive torque.

Finally, in comparing the torque ripple of both devices, the open-loop and closed-loop controlled MPB exhibits 2.7% and 1.5%, respectively, while the WDB (as previously mentioned) exhibits a torque ripple of approximately 5%. Table 3-2 summarizes the performance characteristics of the wafer disc brake versus those of the magnetic particle brake.

Normalized Step Responses of WDB and MPB

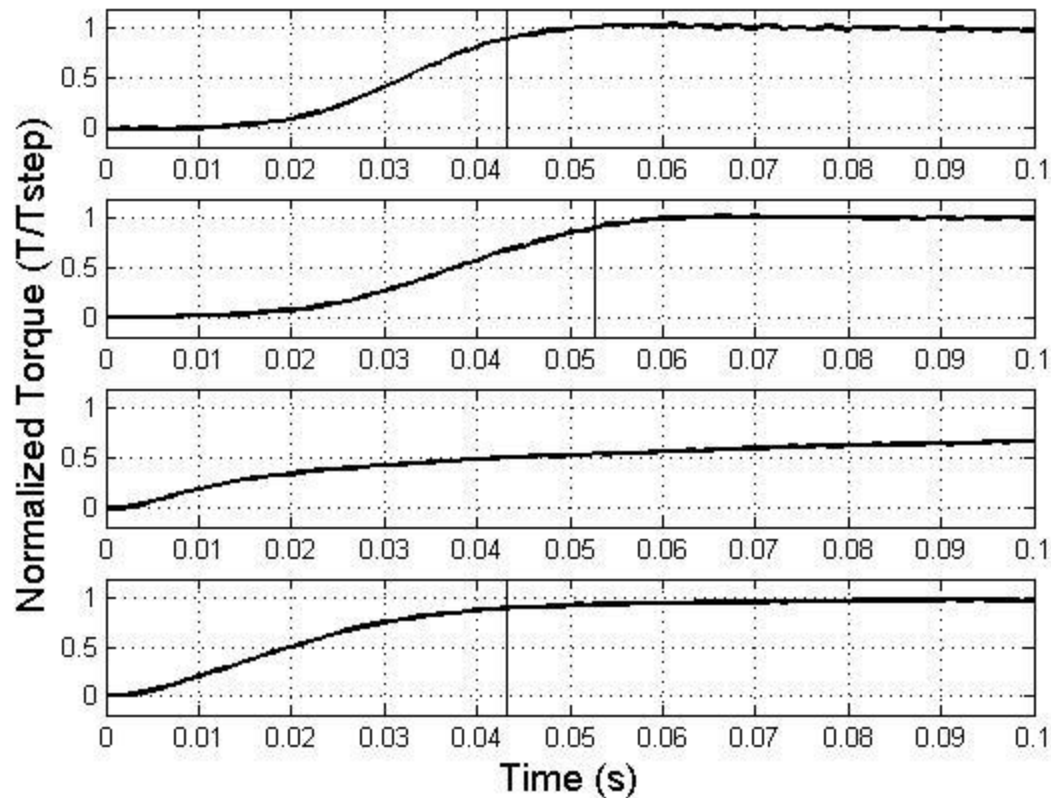


Figure 3-15. Normalized step responses of wafer disc brake and magnetic particle brake with step command initiation at time = 0 seconds. (a) Normally unlocked brake response ($T_{step} = 20$ N-m). (b) Normally locked brake response ($T_{step} = 20$ N-m). (c) Particle brake response in open-loop ($T_{step} = 6.5$ N-m). (d) Particle brake response in closed-loop ($T_{step} = 6.5$ N-m).

Characteristic	B115 MPB	Normally Unlocked WDB	Normally Locked WDB
Max Dynamic Torque [N-m](in-lbs.)	13.0 (115)	40 (354)	50+ (443+)
Max Static Torque [N-m](in-lbs.)	16.6 (147)	73 (646)	74 (655)
Min Torque [N-m](in-lbs.)	0.28 (2.5)	0.40 (3.5)	0.40 (3.5)
Torque Ripple [%],			
Open Loop Control	2.7	-	-
Closed Loop Control	1.5	5.0	5.0
Dynamic Torque-to-Weight [N-m/kg]	3.58	59.7	74.6+
Dynamic Range	1:46	1:100	1:125+
Rise Time [s], Open Loop Control	0.420	-	-
Closed Loop Control	0.043	0.043	0.053
Bandwidth for \pm 25% FS Oscillations [Hz]			
Open Loop Control	2	-	-
Closed Loop Control	22	11	10
Steady-State Power Consumption (Normalized by torque) [W/N-m]	0.87	0.26	0.22
Max Continuous Power Dissipation [W]	55	125	125
Weight [kg](lbs.)	3.63 (8.0)	0.67 (1.48)	0.67 (1.48)
Diameter [mm](in)	120 (4.71)	102 (4.00)	102 (4.00)
Length [mm](in)	66.8 (2.63)	47.6 (1.88)	47.6 (1.88)

Table 3-2. Comparison of the B115 magnetic particle brake with the wafer disc brake.

7. Conclusion and Recommendations

The authors have presented a design for an electrically actuated proportional brake, called a wafer disc brake (WDB), that offers some advantages relative to a magnetic particle brake (MPB, considered the benchmark of such devices). Specifically, the WDB exhibits a torque-to-weight ratio that is (more than) an order of magnitude larger than the MPB, while requiring less than one third of the steady-state electrical power for a given level of resistive torque. Further, unlike the MPB (and most other previously reported devices), the WDB can be configured in a normally unlocked or normally locked configuration.

The WDB also has some disadvantages relative to an MPB. One potential disadvantage of the WDB is disc wear, although this could be mitigated with the use of more wear-resistant discs (such as stainless steel or ceramic). The WDB also exhibits greater torque ripple relative to the MPB. As discussed herein, control of the WDB is more complex than control of the MPB, although accurate torque tracking and good dynamic performance requires an outer torque loop for both. Finally, as currently designed, the WDB is likely more expensive to produce than a MPB.

8. References

- [24] R. J. Farris, Hugo A. Quintero, Thomas J. Withrow, and Michael Goldfarb, "Design and Simulation of a Joint-Coupled Orthosis for Regulating FES-Aided Gait" *Robotics and Automation, 2009 IEEE International Conference on* , pp.1916-1922, May 2009.
- [25] R. J. Farris, Hugo A. Quintero, Thomas J. Withrow, and Michael Goldfarb, "Design of a Joint-Coupled Orthosis for FES-Aided Gait" *Rehabilitation Robotics, 2009 IEEE International Conference on* , pp.246-252, April 2009.
- [26] M. Goldfarb, W. Durfee, K. Korkowski, and B. Harrold. Evaluation of a Controlled-Brake Orthosis for FES-Aided Gait, *IEEE Transactions on Neural Systems and Rehabilitative Engineering*, vol. 11, no. 3, pp. 241-248, 2003.
- [27] M. Goldfarb and W. Durfee. Design of a Controlled-Brake Orthosis for Regulating FES-Aided Gait. *IEEE Transactions on Rehabilitation Engineering*, vol. 4, no. 1, pp. 13-24, 1996.
- [28] B. Weinberg et al., "Design, Control and Human Testing of an Active Knee Rehabilitation Orthotic Device," *Robotics and Automation, 2007 IEEE International Conference on* , pp.4126-4133, 10-14 April 2007
- [29] J. Chen and W. Liao, "Design and control of a Magnetorheological actuator for leg exoskeleton," *Robotics and Biomimetics, 2007. ROBIO 2007. IEEE International Conference on* , pp.1388-1393, Dec. 2007

- [30] B. Aeyels, W. Van Petegem, J. Vander Sloten, G. Van der Perre, and L. Peeraer, "EMG-based finite state approach for a microcomputer-controlled above-knee prosthesis," Proceedings for the IEEE Engineering in Medicine and Biology 17th Annual Conference, vol. 17, no. 2, pp. 1315-1316, Sep. 1995.
- [31] W. S. Harwin, L. O. Leiber, G. P. G. Austwick, and C. Dislis, "Clinical potential and design of programmable mechanical impedances for orthotic applications," Robotica, vol.16, pp. 523-530, Sep.-Oct. 1998.
- [32] H. Herr, and A. Wilkenfeld, "User-Adaptive Control of a Magnetorheological Prosthetic Knee," Industrial Robot: An International Journal. 2003; 30: 42-55.
- [33] J. Furusho et al., "Development of Shear Type Compact MR Brake for the Intelligent Ankle-Foot Orthosis and Its Control; Research and Development in NEDO for Practical Application of Human Support Robot," Rehabilitation Robotics, 2007. ICORR 2007. IEEE 10th International Conference on , pp.89-94, June 2007
- [34] Changhyun Cho; Jae-Bok Song; Munsang Kim, "Energy-Based Control of a Haptic Device Using Brakes," Systems, Man, and Cybernetics, Part B: Cybernetics, IEEE Transactions on, vol.37, no.2, pp.341-349, April 2007
- [35] Jinung An; Dong-soo Kwon, "Haptic experimentation on a hybrid active/passive force feedback device," Robotics and Automation, 2002. Proceedings. ICRA '02. IEEE International Conference on , vol.4, pp. 4217-4222, 2002
- [36] Ying Jin; Furusho, J.; Kikuchi, T.; Oda, K.; Takashima, S., "A basic study on passive force display and rehabilitation system with redundant brakes," Complex Medical Engineering, 2009. CME. ICME International Conference on , pp.1-6, 9-11 April 2009
- [37] M. Sakaguchi, et al., "Passive force display using ER brakes and its control experiments," Virtual Reality, 2001. Proceedings. IEEE , pp.7-12, 17-17 March 2001
- [38] ZhiDong Wang; Fukaya, K.; Hirata, Y.; Kosuge, K., "Control Passive Mobile Robots for Object Transportation - Braking Torque Analysis and Motion Control," Robotics and Automation, 2007 IEEE International Conference on , pp.2874-2879, 10-14 April 2007.
- [39] N.M. Mayer, F. Farkas, and M. Asada, "Balanced walking and rapid movements in a biped robot by using a symmetric rotor and a brake," Mechatronics and Automation, 2005 IEEE International Conference , vol.1, pp. 345-350, 29 July-1 Aug. 2005.
- [40] Ahn Kyoung Kwan; Tran Hai Nam; Yoon Young Il, "New approach to design MR brake using a small steel roller as a large size magnetic particle," Control,

Automation and Systems, 2008. ICCAS 2008. International Conference on , pp.2640-2644, 14-17 Oct. 2008.

- [41] B. Kavlicoglu, F. Gordaninejad, and C. Evrensel, "A Semi-Active, High-Torque, Magnetorheological Fluid Limited Slip Differential Clutch," Journal of Vibration and Acoustics, vol.128, issue5, pp.604-611, Oct. 2006.
- [42] K. Karakoc, E. J. Park, and A. Suleman, Design considerations for an automotive magnetorheological brake, Mechatronics, vol.18, issue8, Pages 434-447, Oct. 2008.
- [43] W.H. Li, and H. Du, "Design and Experimental Evaluation of a Magnetorheological Brake," The International Journal of Advanced Manufacturing Technology, vol.21, issue7, pp.508-515, May 2003.
- [44] Gosline, and V. Hayward, "Eddy Current Brakes for Haptic Interfaces: Design, Identification, and Control," Mechatronics, IEEE/ASME Transactions on , vol.13, no.6, pp.669-677, Dec. 2008.
- [45] D. Senkal, and H. Gurocak, "Compact MR-brake with serpentine flux path for haptics applications," EuroHaptics conference, 2009 and Symposium on Haptic Interfaces for Virtual Environment and Teleoperator Systems. World Haptics 2009. Third Joint , pp.91-96, 18-20 March 2009.
- [46] M. Gogola, and M. Goldfarb, "Design of a PZT-actuated proportional drum brake," Mechatronics, IEEE/ASME Transactions on , vol.4, no.4, pp.409-416, Dec 1999.
- [47] W. C. Orthwein, Clutches and Brakes Design and Selection, Second Ed., Chapter 5, Carbondale, IL, Marcel Dekker, Inc., 2004.

APPENDIX A

PART LIST AND DRAWINGS

TABLE A-1. Wafer Disc Brake Fabricated and Modified Parts.

Part No.	Name	Description	Quantity
1	Stator Tube	7075 aluminum central brake body	1
2	Rotor Barrel	7075 aluminum outer brake body	1
3	Top Cap	7075 aluminum	1
4	Bottom Cap	7075 aluminum	1
5	Compression Star	7075 aluminum force transmission member	1
6	Motor Cover	301 stainless steel disc to enclose the brake	1
7	Stator Disc	Laser-cut from 0.010" G-10 wear resistant film	23
8	Rotor Disc	Laser-cut from 0.010" G-10 wear resistant film	22
9	Spring Guide	ABS plastic hemispheres to hold normally locked springs in place	6
10	Disc Spacer	ABS plastic disc to position the disc stack vertically	1
11	Stator Key	Laser-cut "stator splines" from 1/8" Ultem sheet	18
12	Rotor Key	Laser-cut "rotor splines" from 1/8" Ultem sheet	18
13	DU Radial Bearing	Cut from 56DU32 GGB DU dry bearing	2
14	DU Thrust Bearing	Water-jet cut from DI0594x5.00 GGB DU flat strip material	2
15	Motor	#200142 Maxon EC 45 flat 30 W brushless motor	1
16	Ball Screw and Nut	Faulhaber Microlinea ED513X / V501X precision ball screw and nut	1

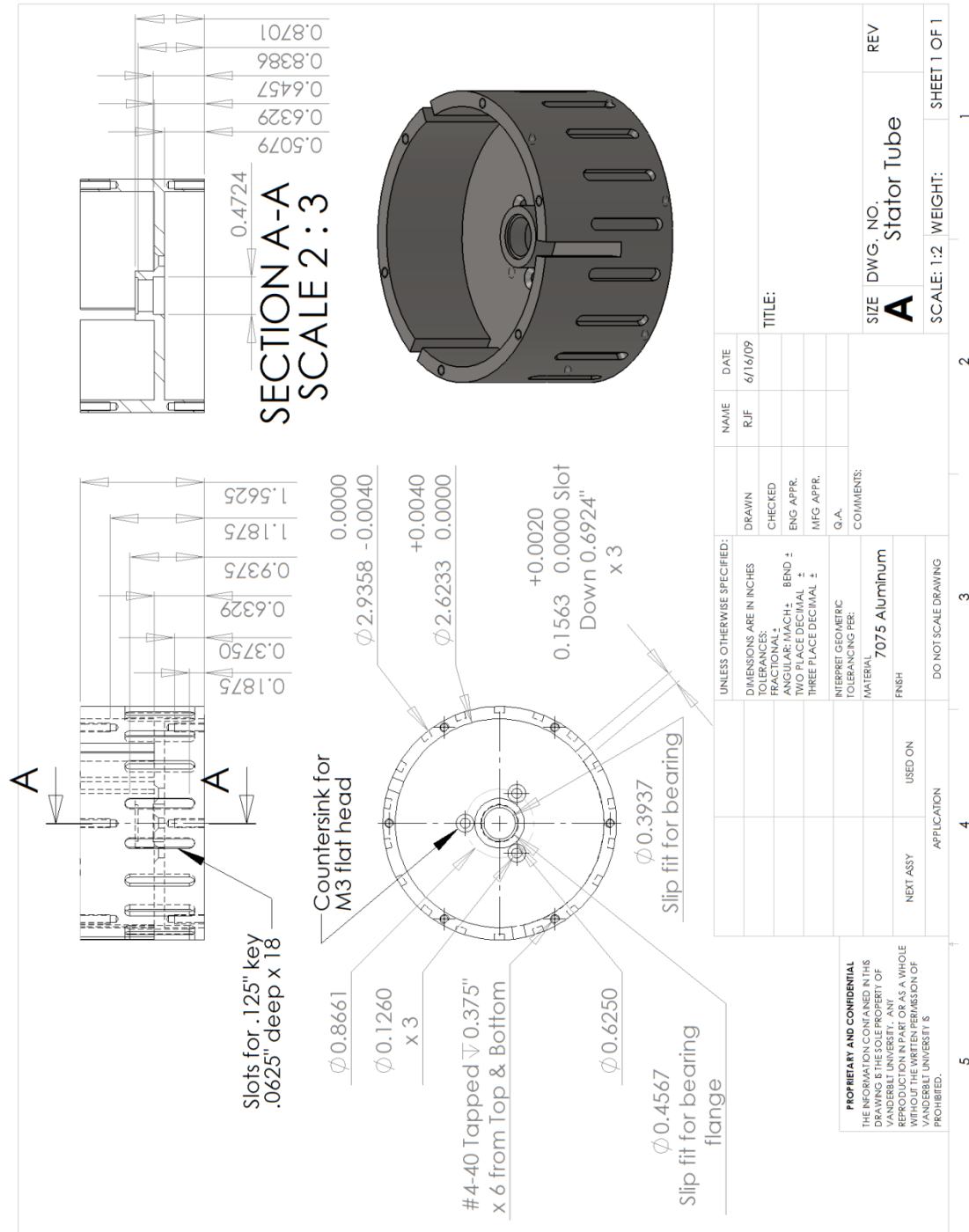


Figure A-1. Stator tube detail drawing.

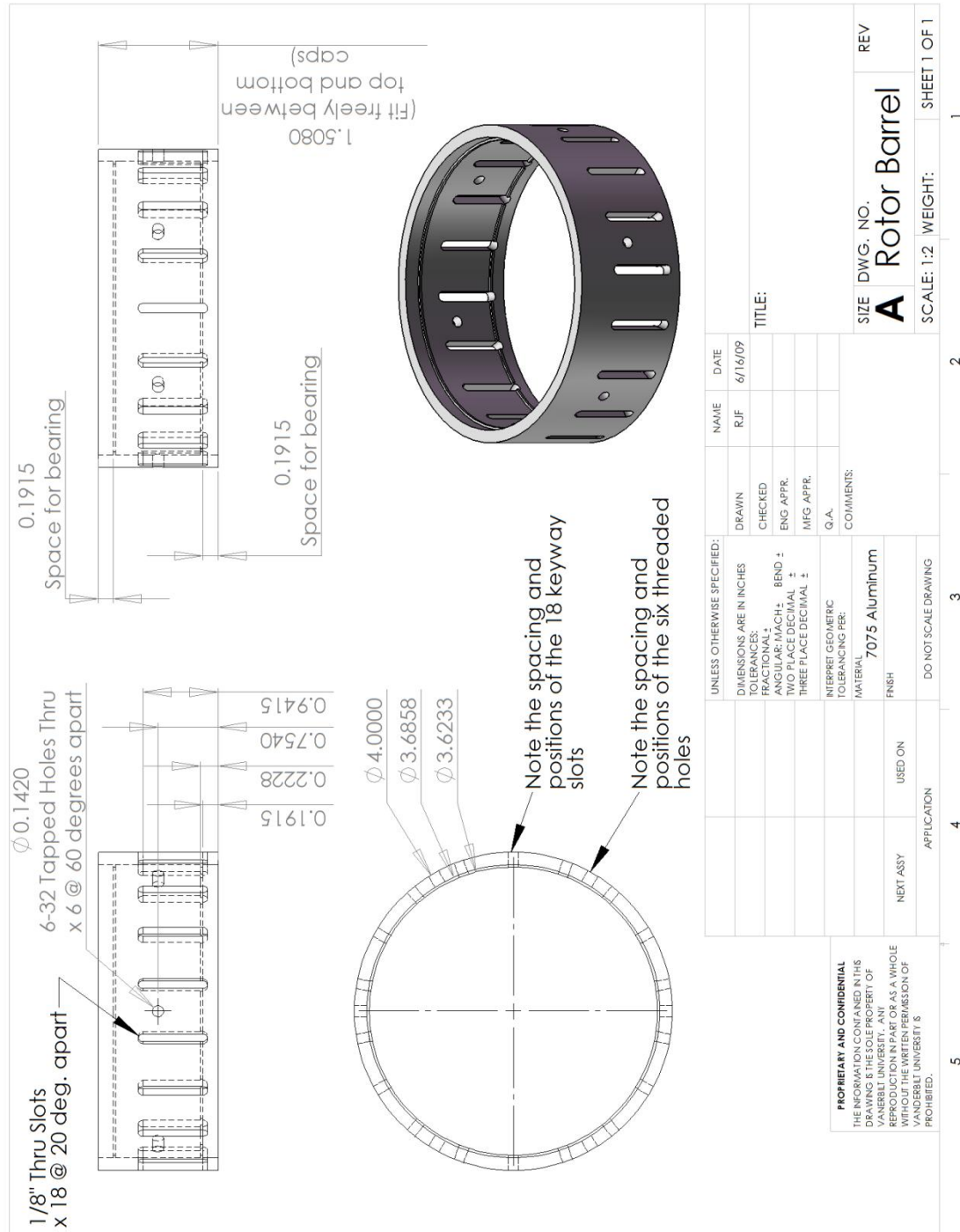


Figure A-2. Rotor barrel detail drawing.

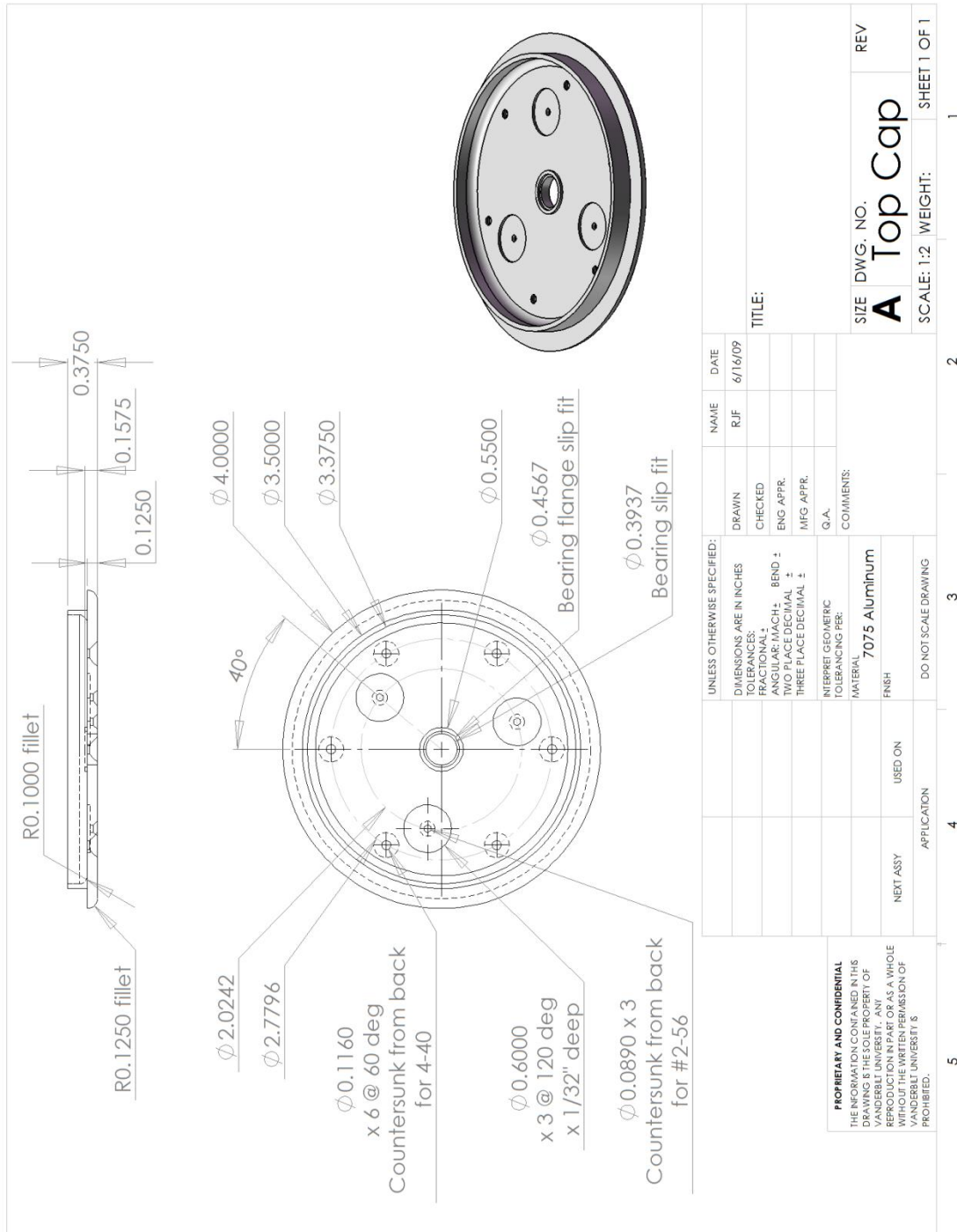


Figure A-3. Top cap detail drawing.

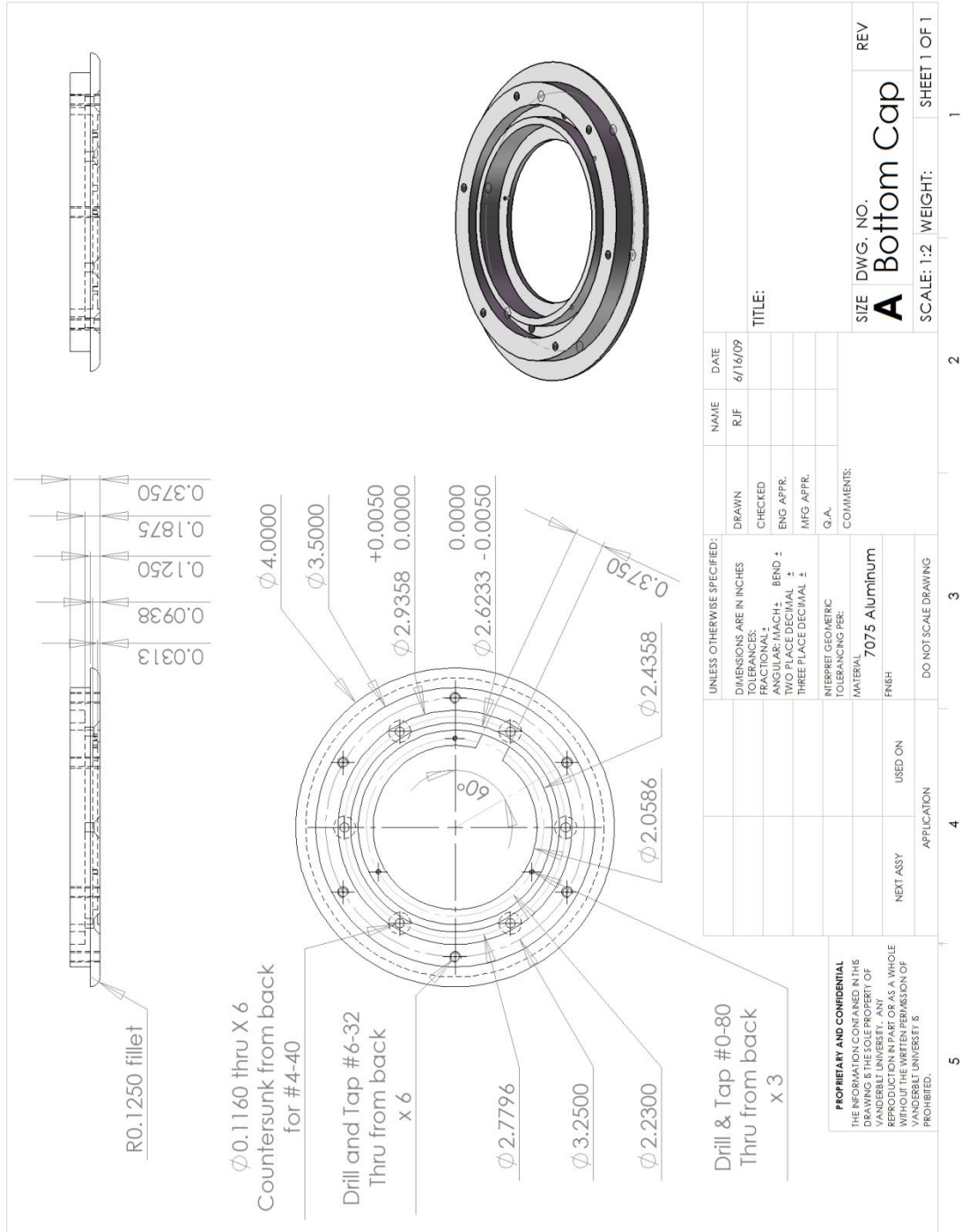


Figure A-4. Bottom cap detail drawing.

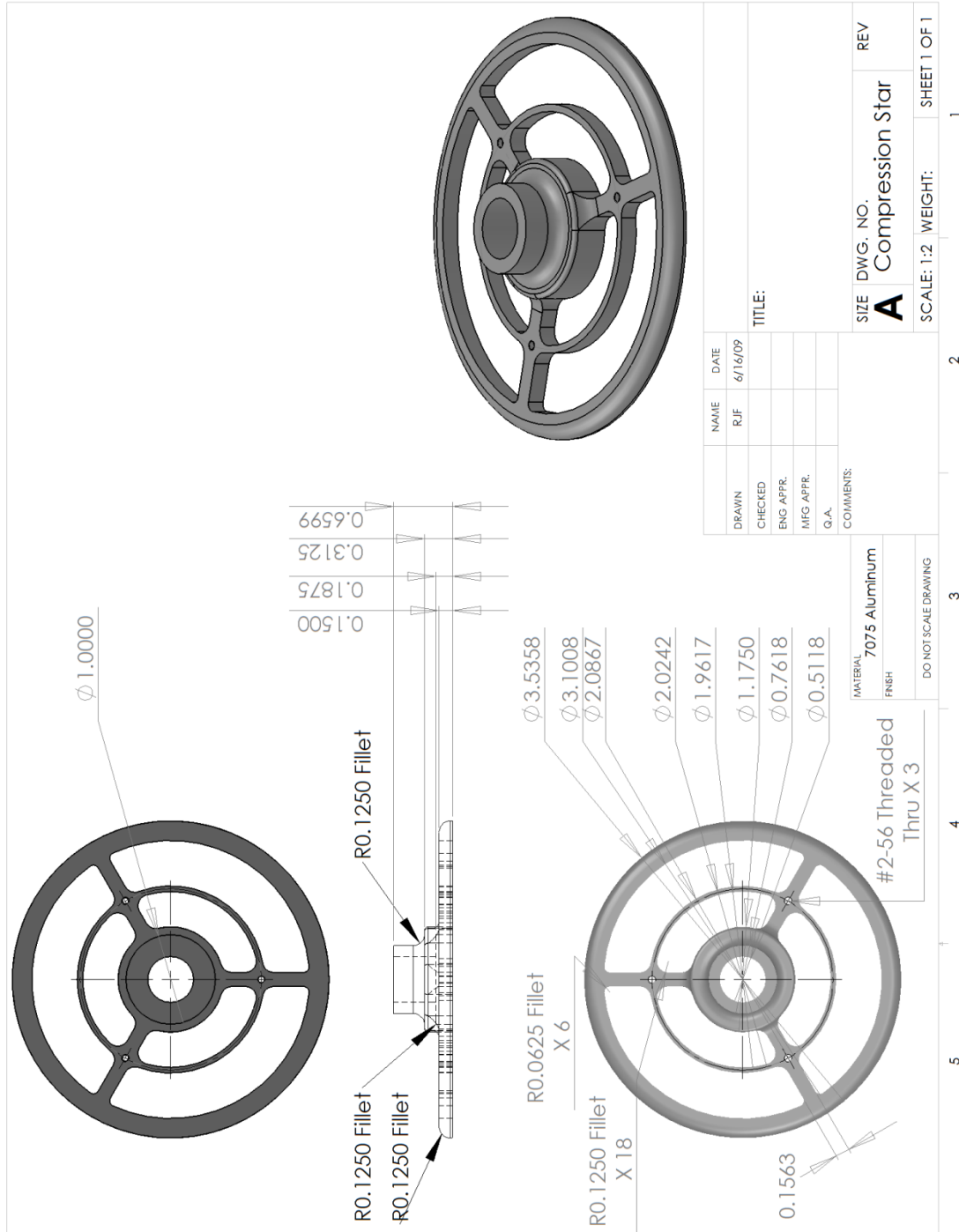


Figure A-5. Compression star detail drawing.

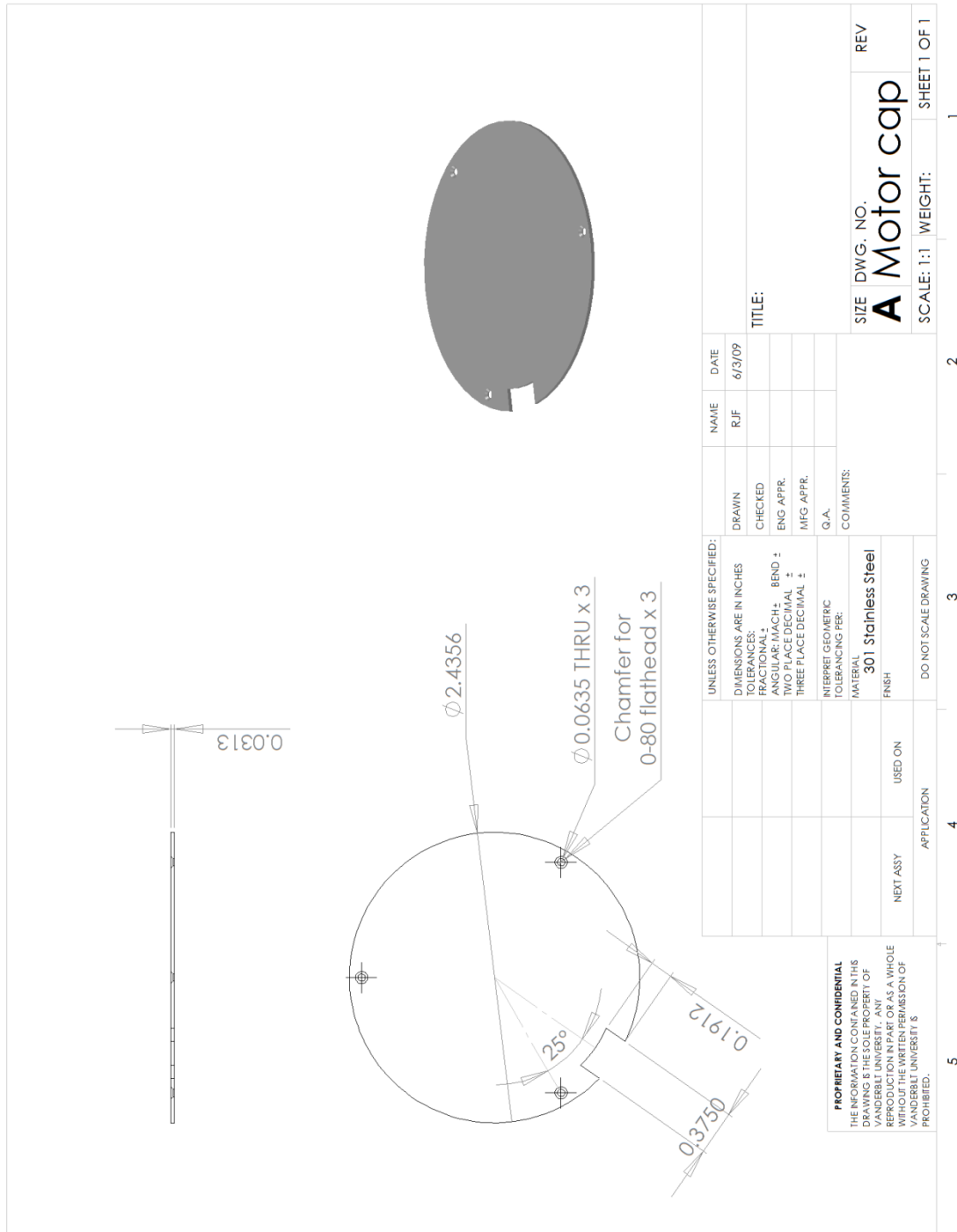


Figure A-6. Motor cap detail drawing.

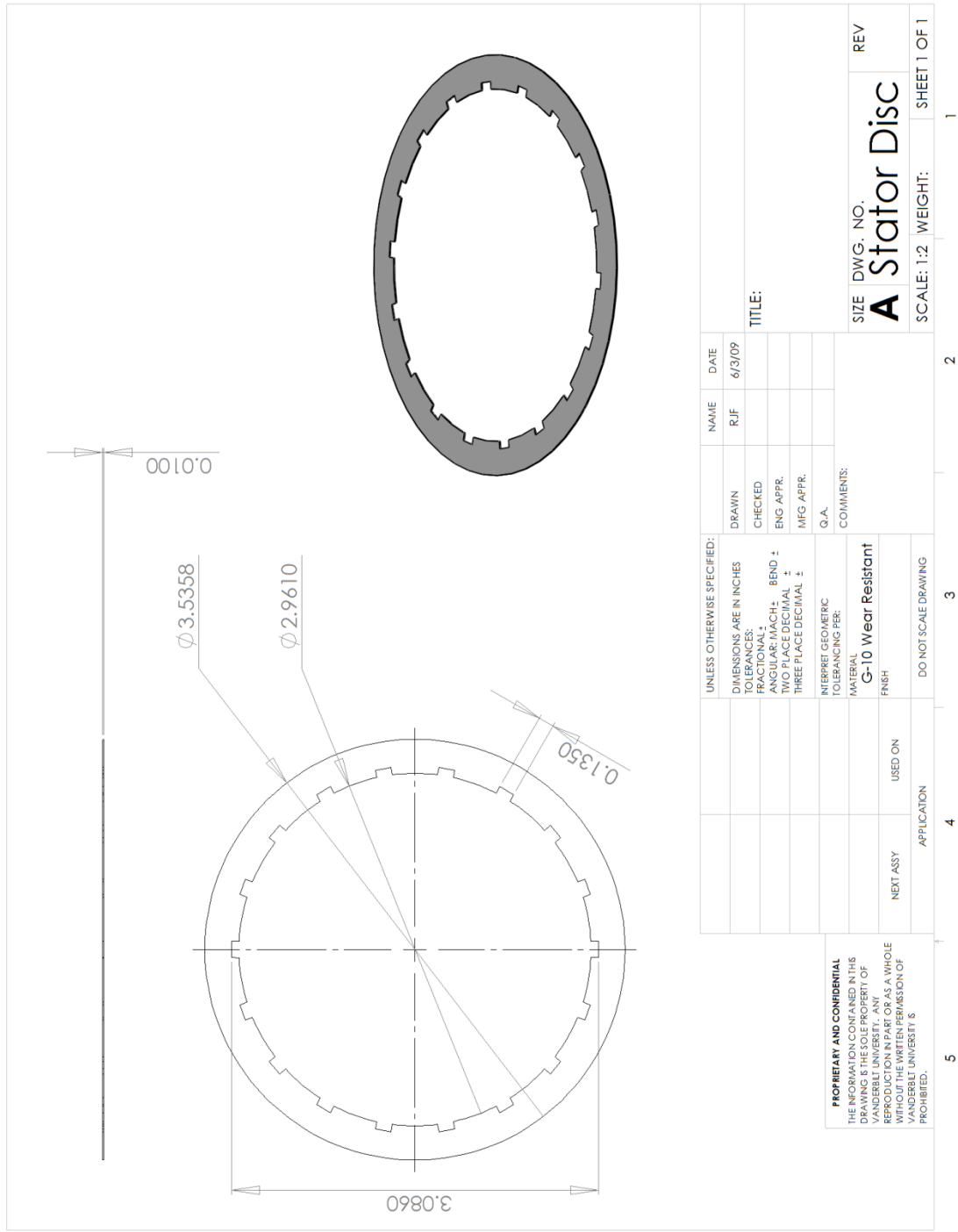


Figure A-7. Stator disc detail drawing.

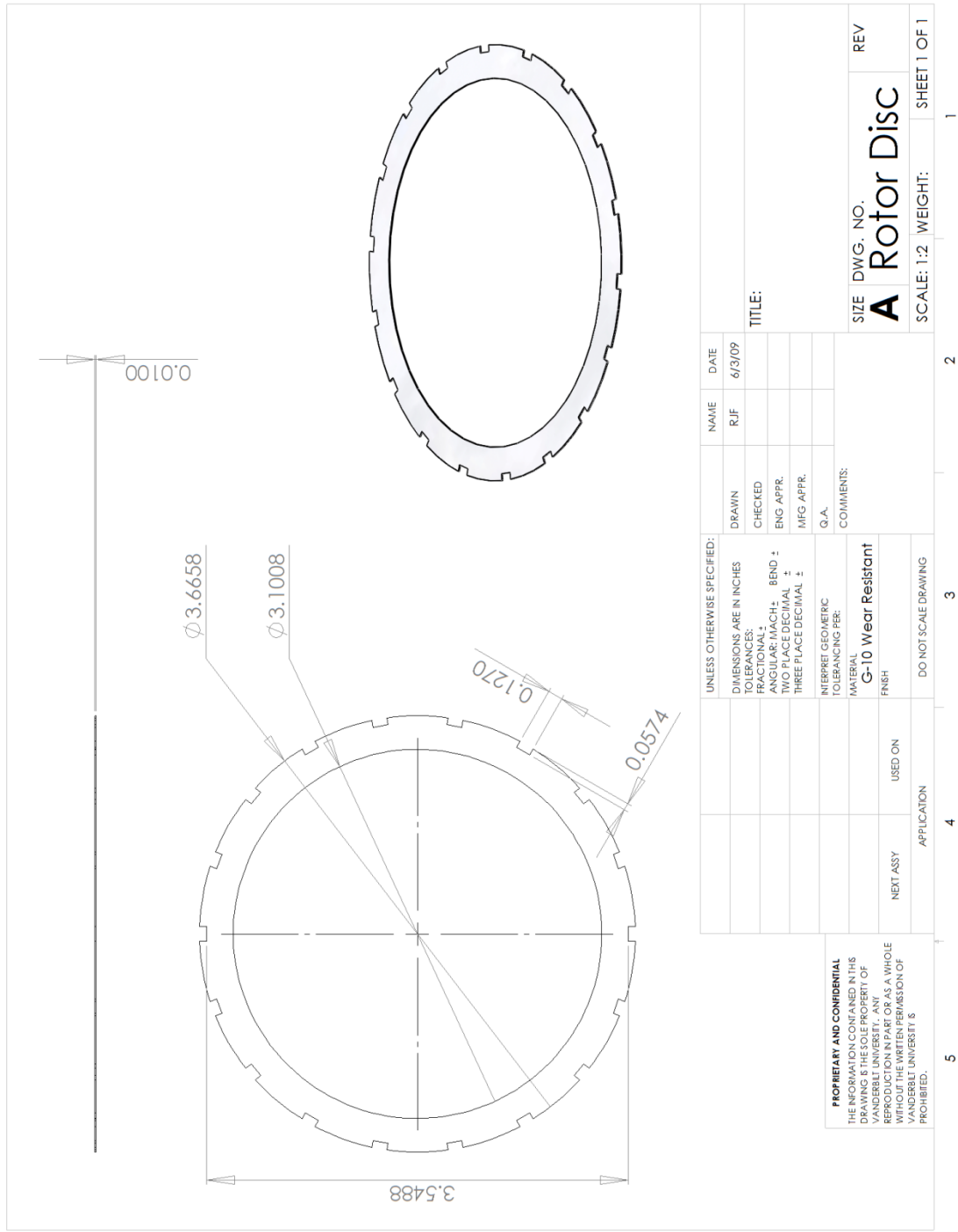


Figure A-8. Rotor disc detail drawing.

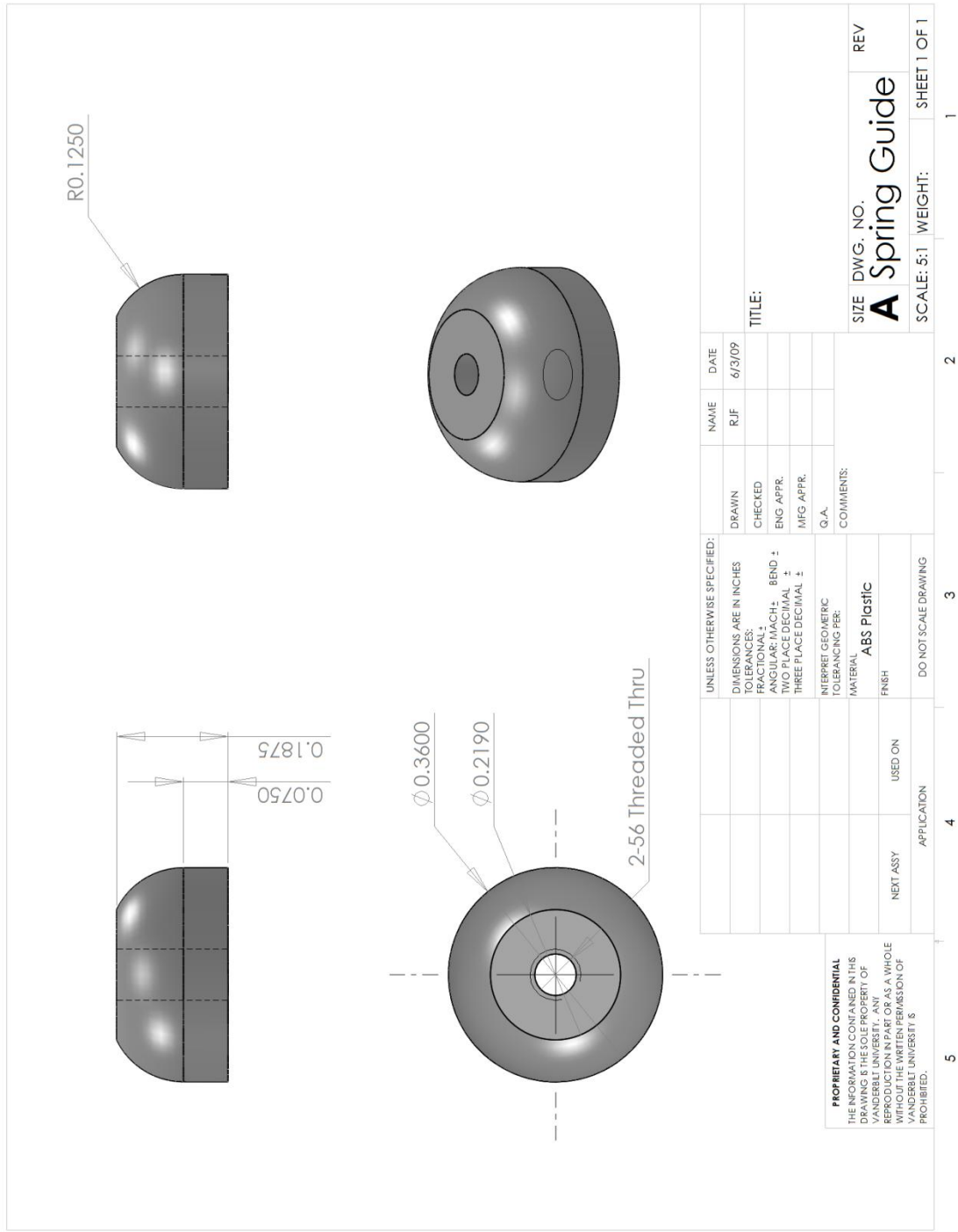


Figure A-9. Spring guide detail drawing.

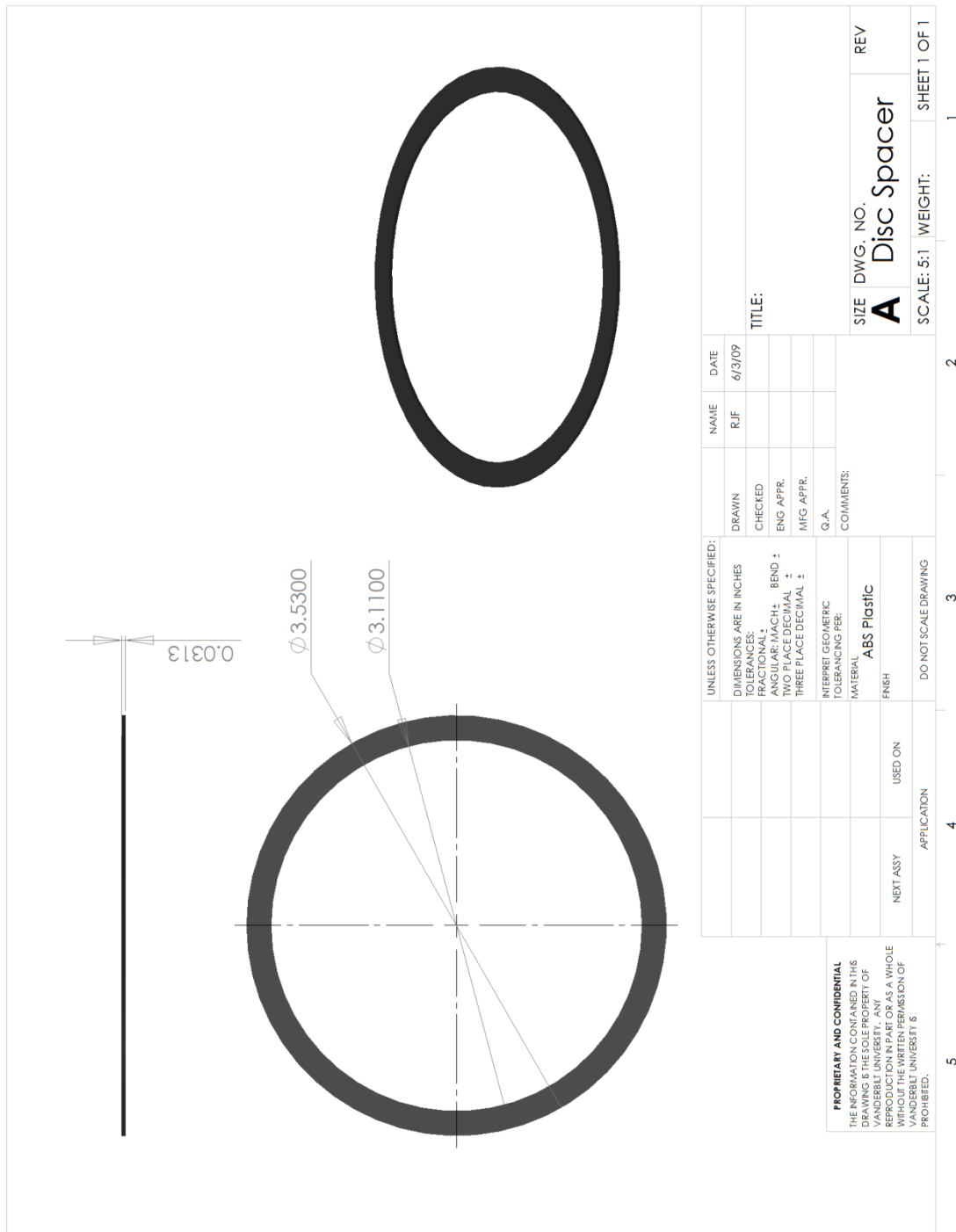


Figure A-10. Disc spacer detail drawing.

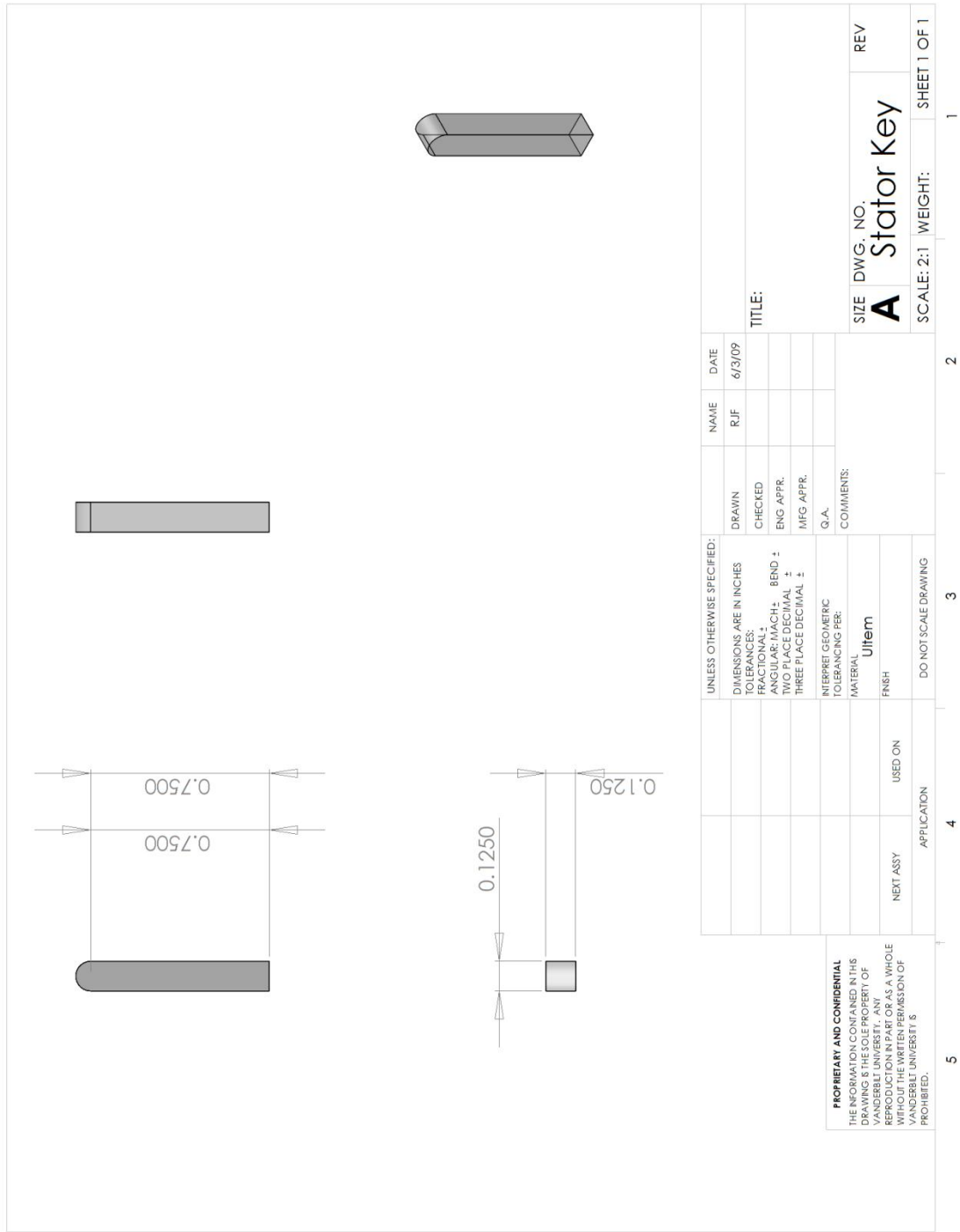


Figure A-11. Stator key detail drawing.

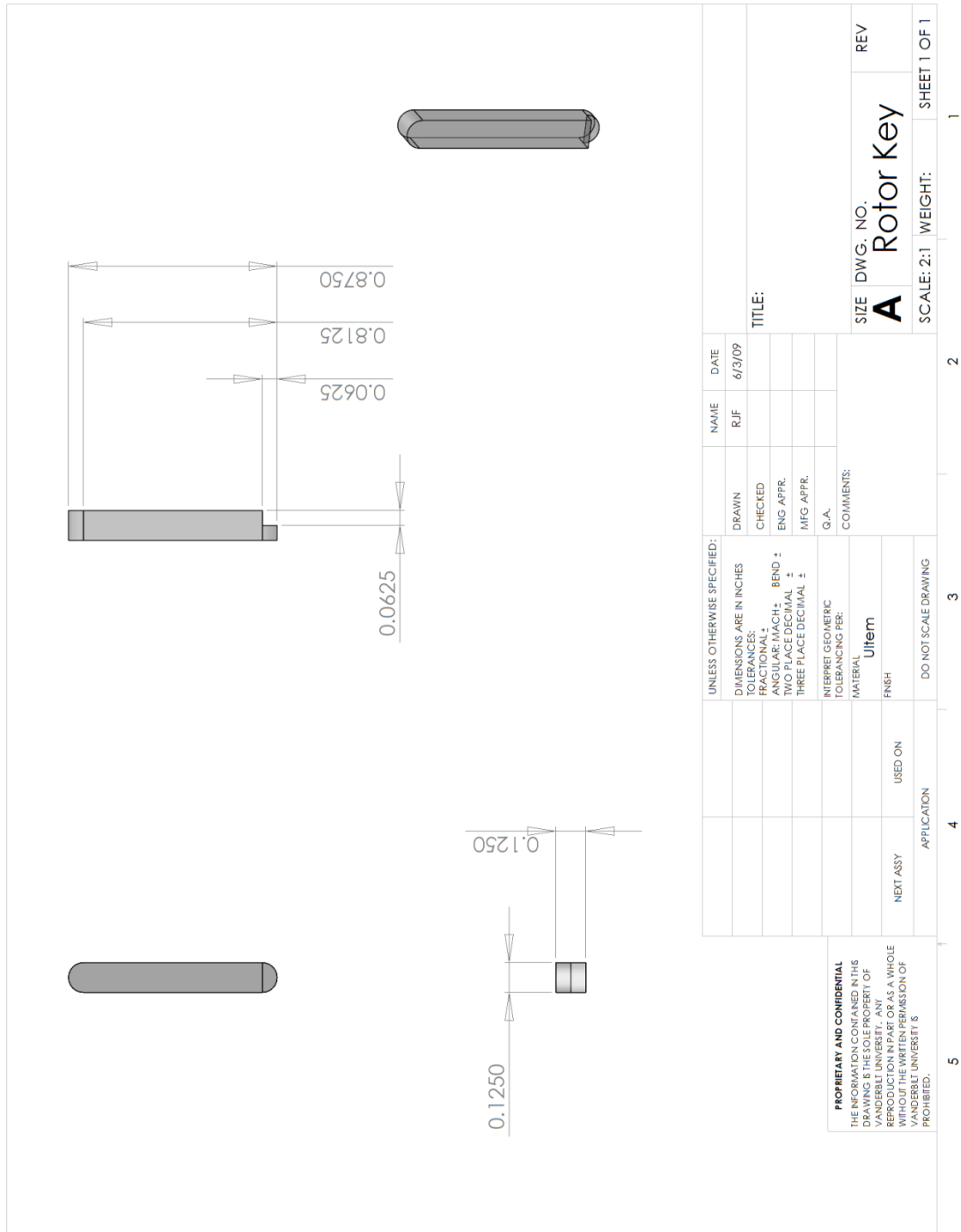


Figure A-12. Rotor key detail drawing.

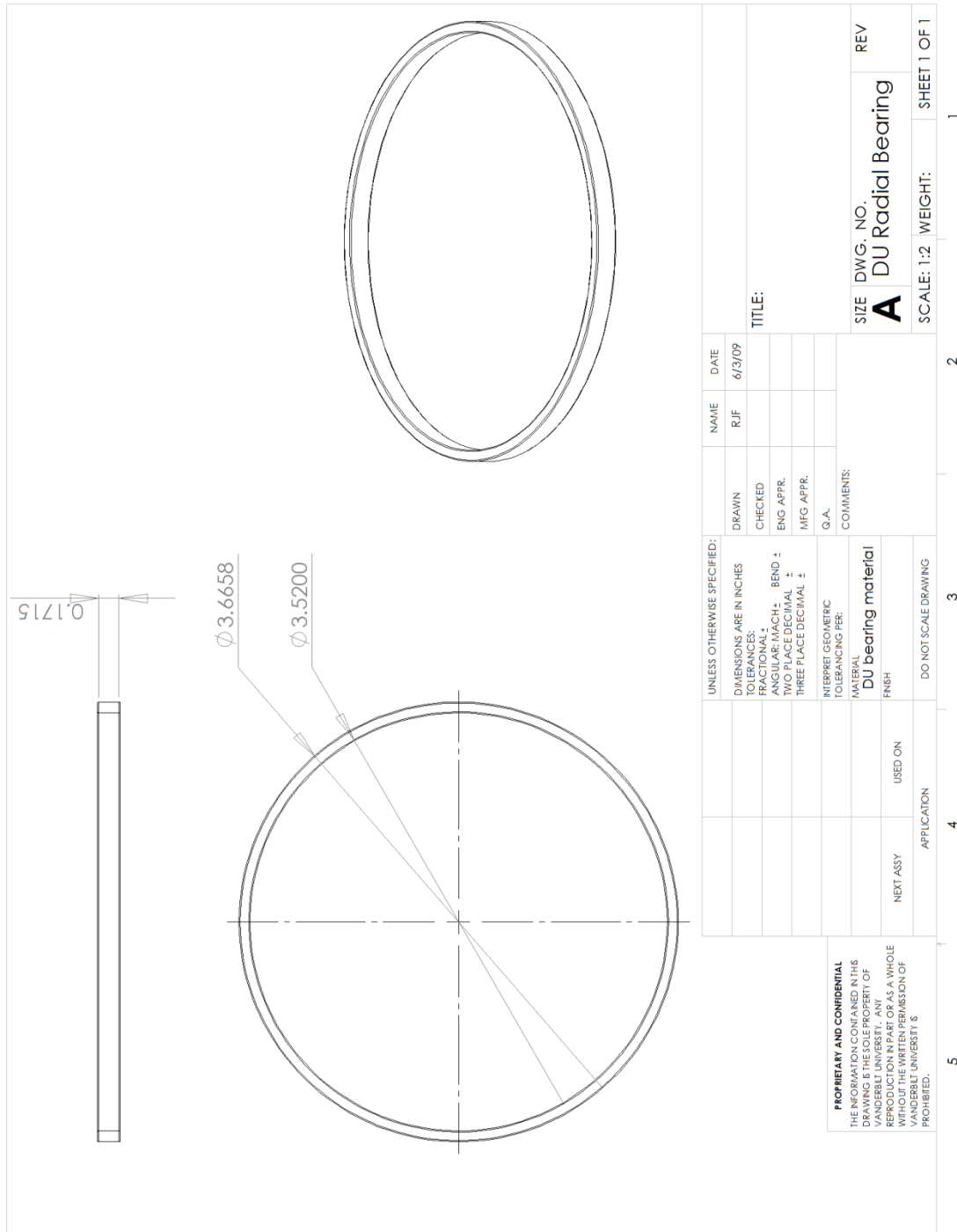


Figure A-13. DU radial bearing detail drawing.

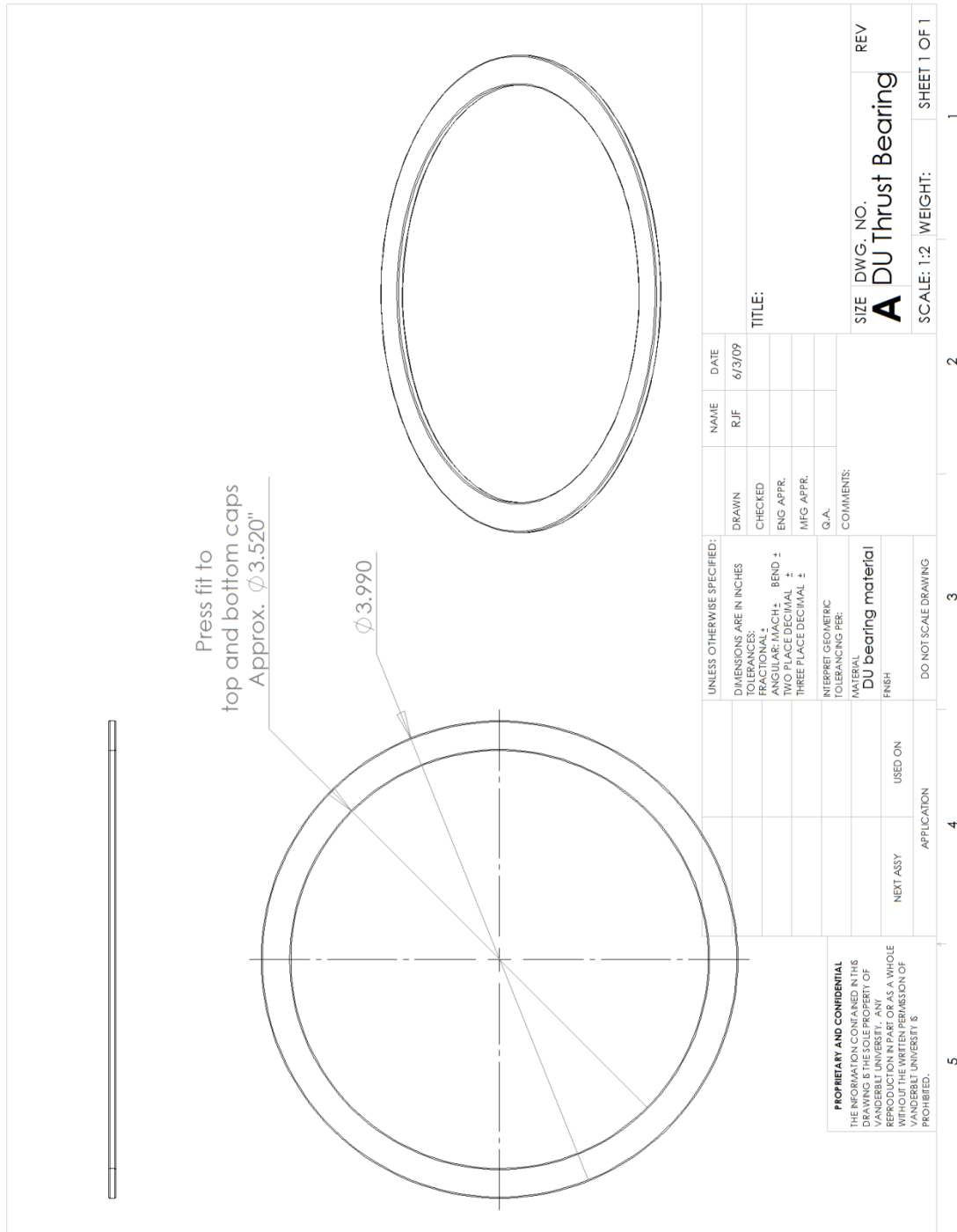


Figure A-14. DU thrust bearing detail drawing.

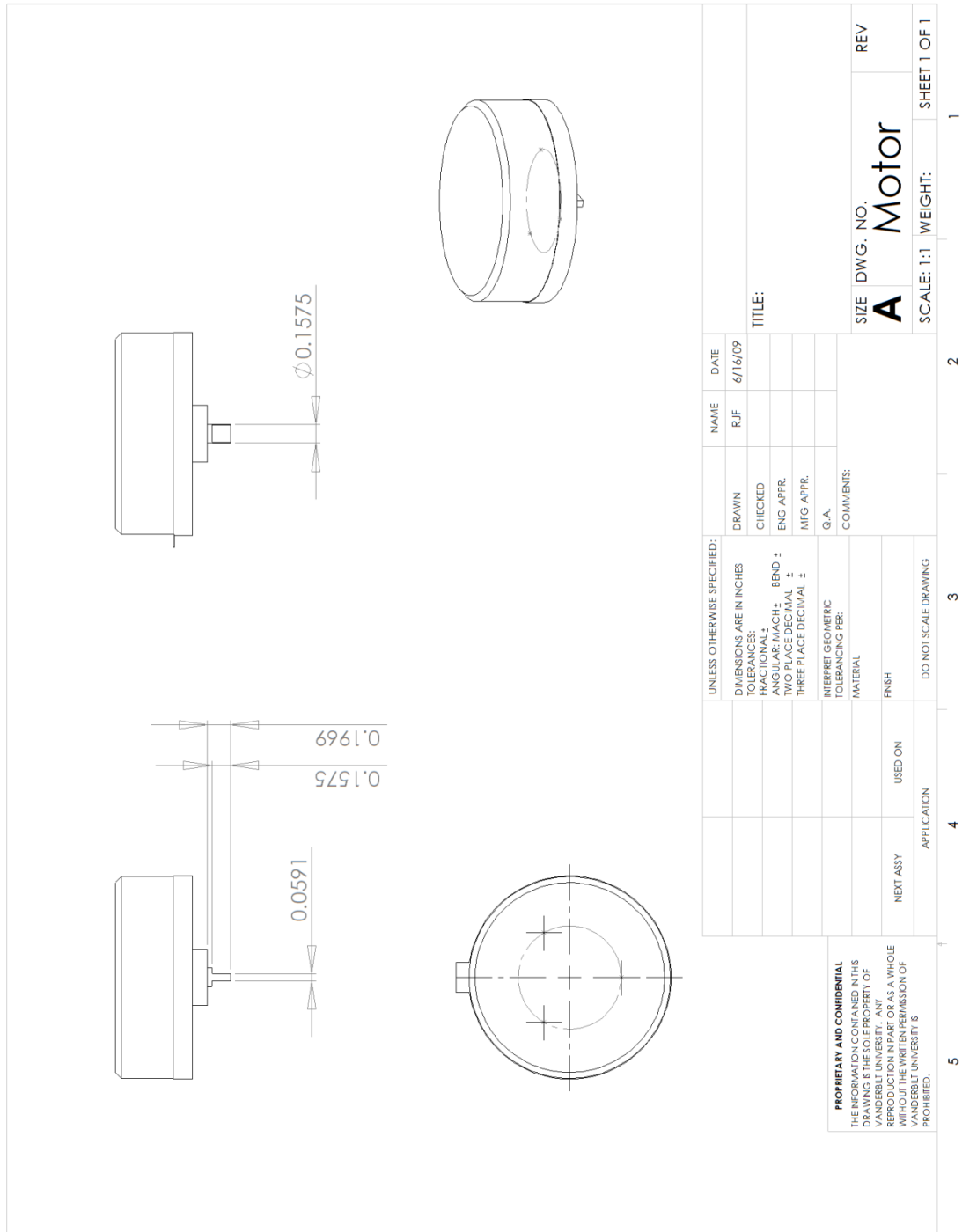


Figure A-15. Motor alteration detail drawing.

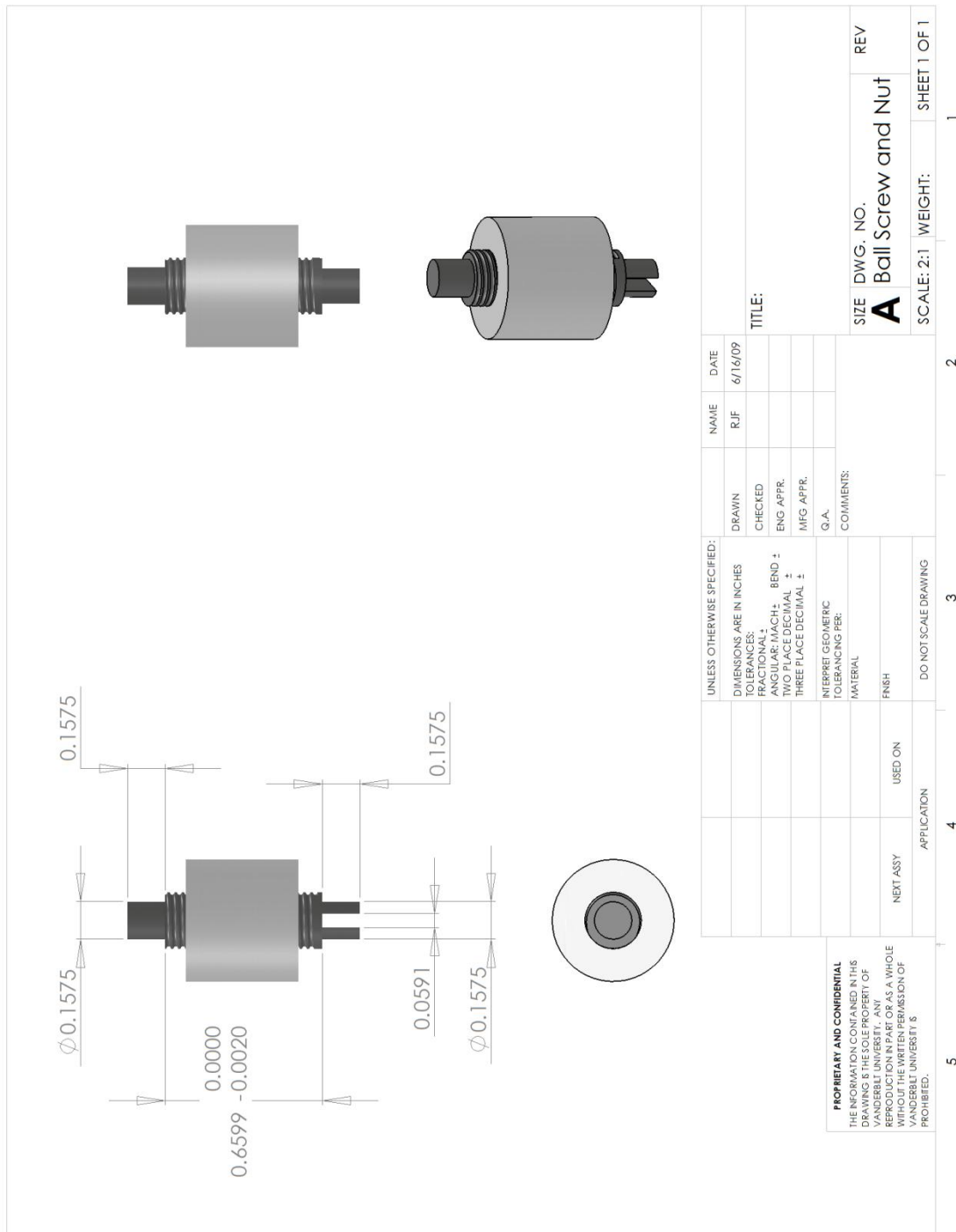


Figure A-16. Ball screw alteration detail drawing.

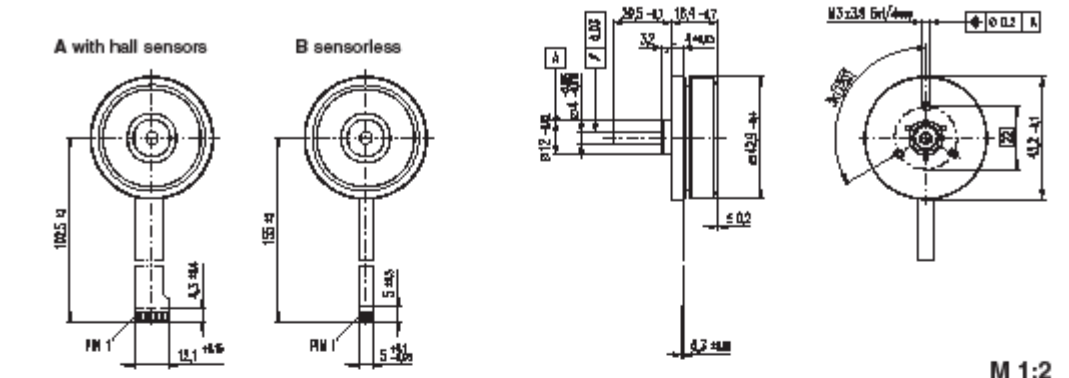
APPENDIX B

COMPONENT LIST AND DATA SHEETS

TABLE B-1. Wafer Disc Brake Purchased Components.

Component No.	Name	Description	Quantity
1	Motor	#200142 Maxon EC 45 flat 30 W brushless motor	1
2	Ball Screw and Nut	Faulhaber Microlinea ED513X / V501X precision ball screw and nut	1
3	DU Radial Bearing	56DU32 GGB DU dry bearing	2
4	DU Thrust Bearing	GGB DU flat strip material	2
5	Flanged Ball Bearing	ABEC-5 flanged double shielded stainless steel	2
5	Normally Unlocked Spring	Spring tempered steel compression spring; 5/8" long, 19.10 lbs./inch	1
6	Normally Locked Spring	302 stainless steel compression spring; 1-1/2" long, 18.33 lbs./inch	3

EC 45 flat Ø45 mm, brushless, 30 Watt



M 1:2

Stock program
Standard program
Special program (on request)

Order Number

A with Hall sensors	200142	330281	330282	
B sensorless	200180	330283	330284	

Motor Data

Values at nominal voltage

1 Nominal voltage	V	12.0	12.0	24.0	24.0	36.0	36.0
2 No load speed	rpm	4370	4360	4370	4370	4760	4760
3 No load current	mA	151	150	75.8	75.2	56.9	56.9
4 Nominal speed	rpm	2880	2820	2850	2840	3210	3210
5 Nominal torque (max. continuous torque)	mNm	50.0	54.3	58.8	57.5	70.6	69.5
6 Nominal current (max. continuous current)	A	2.14	2.00	1.07	1.05	0.893	0.882
7 Stall torque	mNm	255	219	253	243	380	389
8 Starting current	A	10.0	8.57	4.96	4.77	5.38	5.22
9 Max. efficiency	%	77	76	77	77	81	81
Characteristics							
10 Terminal resistance phase to phase	Ω	1.20	1.40	4.84	5.04	6.70	6.9
11 Terminal inductance phase to phase	mH	0.580	0.580	2.24	2.24	4.29	4.29
12 Torque constant	mNm / A	25.5	25.5	51.0	51.0	70.6	70.6
13 Speed constant	rpm / V	374	374	187	187	135	135
14 Speed / torque gradient	rpm / mNm	17.8	20.6	17.8	18.5	12.8	13.2
15 Mechanical time constant	ms	17.1	19.9	17.2	17.9	12.4	12.8
16 Rotor inertia	gcm²	02.5	02.5	02.5	02.5	02.5	02.5

Specifications

Thermal data

17 Thermal resistance housing-ambient	4.23 K/W
18 Thermal resistance winding-housing	4.57 K/W
19 Thermal time constant winding	13.2 s
20 Thermal time constant motor	186 s
21 Ambient temperature	-40 ... +100°C
22 Max. permissible winding temperature	+125°C

Mechanical data (preloaded ball bearings)

23 Max. permissible speed	10000 rpm
24 Axial play at axial load	< 5.0 N 0 mm
	> 5.0 N typ. 0.14 mm preloaded
25 Radial play	
26 Max. axial load (dynamic)	4.8 N
27 Max. force for press fits (static)	50 N
(static, shaft supported)	1000 N
28 Max. radial loading, 7.5 mm from flange	5.5 N

Other specifications

29 Number of pole pairs	8
30 Number of phases	3
31 Weight of motor	88 g

Values listed in the table are nominal.

Connection with hall sensors

Pin 1: 4.8 ... 18 VDC

Pin 2: Hall sensor 3°

Pin 3: Hall sensor 1°

Pin 4: Hall sensor 2°

Pin 5: GND

Pin 6: Motor winding 3

Pin 7: Motor winding 2

Pin 8: Motor winding 1

"Internal pull-up (7 ... 18 V) on pin 1

Wiring diagram for Hall sensors see page 32

Adaptor Order Number Order Number

see p. 308 220300 220310

Connector Article number Article number

AMP 1-487951-1 487951-4

MOLEX 52207-1190 52207-0490

MOLEX 52080-1110 52080-0410

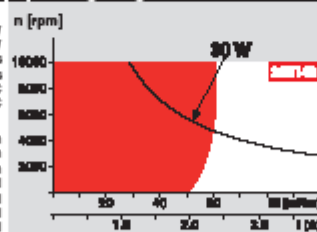
Pin for design with Hall sensors:

FPC, 11 pole, pitch 1.0 mm, top contact style

Pin for design with Hall sensors:

FPC, 11 pole, pitch 1.0 mm, top contact style

Operating Range



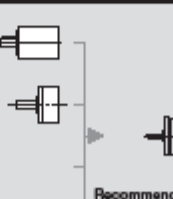
Comments

Continuous operation
In observation of above listed thermal resistance (lines 17 and 18) the maximum permissible winding temperature will be reached during continuous operation at 25°C ambient.
- Thermal limit.

Short term operation
The motor may be briefly overloaded (recuring).

Assigned power rating

maxon Modular System



Overview on page 16 - 21

Recommended Electronics:
DECS 50/5 Page 288
DEC 24/3 289
DEC 50/5 289
DEC Module 24/2 289
DECV 50/5 295
EPOS Module 38/2 302
EPOS 24/1 302
EPOS 24/5 303
EPOS P 24/5 306
Notes 20

May 2009 edition / subject to change

maxon EC motor 195

Figure B-1. Motor data sheet.

NEW

Miniature Ball Screws

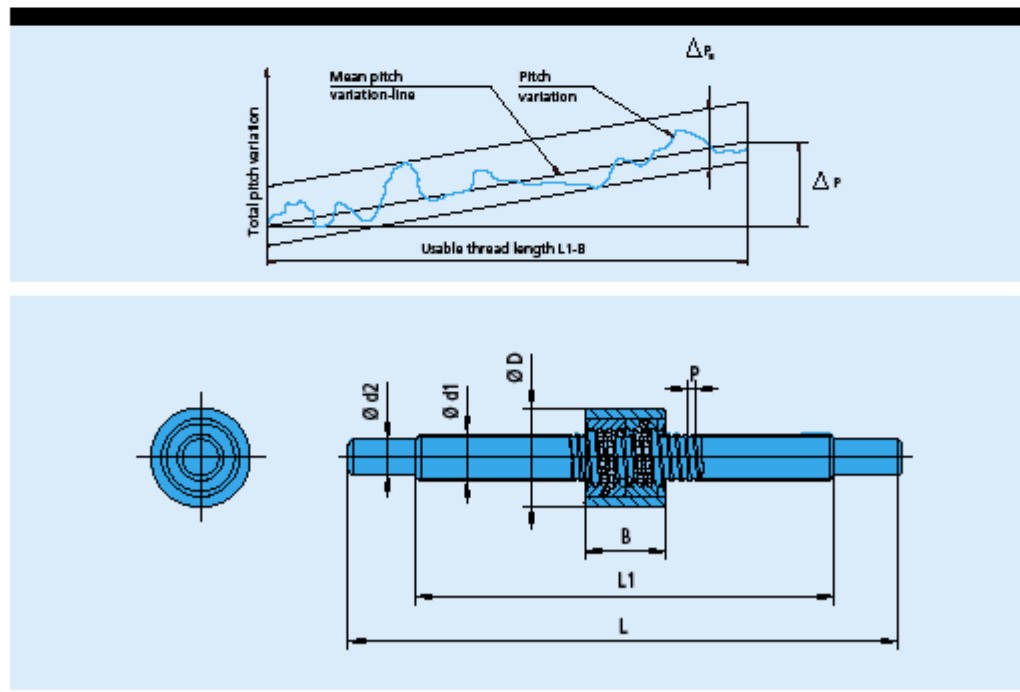
High-precision

Material:
Stainless steel

Series ED...X / V...X

		ED 410X V 404X	ED 513X V 501X	ED 616X V 601X	ED 822X V 801X	ED 1028X V 1001X	
Nut	D	10	13	16	22	28	mm
	B	10	12	14	18	22	mm
Ø balls		0,794	1,000	1,191	1,588	2,000	mm
Screw	d1	4,25	5,8	7,4	10,5	13,6	mm
	P	1,0	1,25	1,5	2,0	2,5	mm
	d2	3	4	6	8	10	mm
	L	70	100	140	190	260	mm
	L1	50	75	110	150	210	mm
Axial load ratings							
- dynamic	Gd	439	671	968	1659	2544	N
- static	Gs	178	299	471	879	1396	N
Technical data							
Tolerance of outside diameter of nut	D	0	0	0	0	0	µm
		-6	-6	-6	-9	-9	µm
Tolerance of the bearing shaft diameter	d2	0	0	0	0	0	µm
		-8	-8	-8	-8	-8	µm
max. pitch variation per L1*	ΔP_{L1}	5	5	5	5	5	µm
max. band width	ΔP_s	5	5	5	5	5	µm
max. eccentricity of the nut on the screw		10	10	12	14	16	µm
Average efficiency		80 - 85	80 - 87	80 - 89	81 - 91	83 - 92	%
Standard axial play		0 - 5	0 - 5	0 - 5	0 - 5	0 - 5	µm
Zero backlash		on request					

* Above are standard specifications. The precision can be increased on request.
 Special executions are available on request.
 Note: The nut must not be removed from the shaft.



Specifications subject to change without notice.

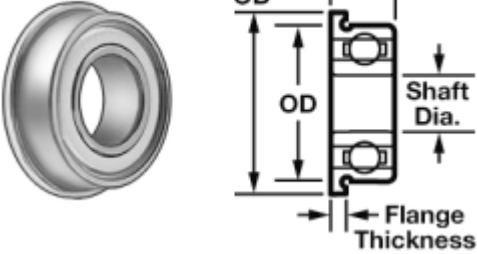
Edition 16.08.2004

www.mpsag.com

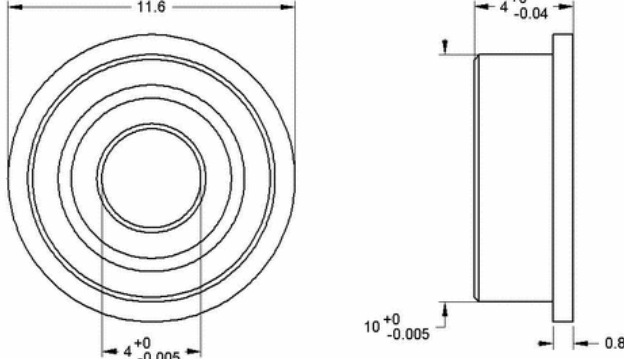
Figure B-2. Ball screw data sheet.

DU®	Characteristics	Applications															
 	<p>Dry bearing material with good wear and friction performance over a wide range of loads, speeds and temperature conditions</p> <p>DU® also performs well with lubrication</p> <p>Available from stock in a wide range of standard sizes</p>	<ul style="list-style-type: none"> Industrial: Lifting equipment, hydraulic pumps and motors, pneumatic equipment, medical equipment, textile machinery, agricultural equipment, scientific equipment, drying ovens, office equipment, etc. 															
Availability	Composition & Structure	Operating Conditions															
<ul style="list-style-type: none"> Ex Stock Standard cylindrical bushes, flanged bushes, thrust washers, flanged washers, strip To order Non-standard parts 	Steel + porous bronze sinter + PTFE + Pb	<table border="1"> <tr> <td></td><td>dry</td><td>very good</td></tr> <tr> <td></td><td>oiled</td><td>good</td></tr> <tr> <td></td><td>greased</td><td>fair</td></tr> <tr> <td></td><td>water</td><td>fair</td></tr> <tr> <td></td><td>process fluid</td><td>fair</td></tr> </table>		dry	very good		oiled	good		greased	fair		water	fair		process fluid	fair
	dry	very good															
	oiled	good															
	greased	fair															
	water	fair															
	process fluid	fair															
Bearing Properties	Unit	Value	Microsection														
Dry			 <p>PTFE + Pb</p> <p>Sinter bronze</p> <p>Steel</p>														
Maximum sliding speed U	m/s	2,5															
Maximum PU factor	N/mm² * m/s = W/mm²	1,8															
Coefficient of friction f	–	0,02 - 0,25															
General																	
Maximum temperature Tmax	°C	+280															
Minimum temperature Tmin	°C	-200															
Maximum load P static	N/mm²	250															
Maximum load P dynamic	N/mm²	140															
Shaft surface finish Ra (Dry Operation)	µm	0,4 ± 0,1															
Shaft hardness	HB	> 200															

Figure B-3. DU bearing data sheet.



Part Number:	7804K129
Type	Ball Bearings
Ball Bearing Style	Flanged Double Shielded
Ball Bearing Type	General Purpose
System of Measurement	Metric
For Shaft Diameter	4 mm
Outside Diameter	10 mm
Width	4 mm
Flange Outside Diameter	11.6 mm
Flange Thickness	.8 mm
ABEC Precision Bearing Rating	ABEC-5
Dynamic Radial Load Capacity, lbs.	132
Dynamic Radial Load Capacity Range, lbs.	6 to 250 lbs.
Maximum rpm	56,000
Maximum rpm Range	30,001 to 60,000
Temperature Range	-65° to +250° F
Bearing Material	Stainless Steel
Stainless Steel Material Type	Type 440C Stainless Steel
Shield Material	300 Series Stainless Steel
Specifications Met	Not Rated
Note	Bearings are lubricated.





McMASTER-CARR	CAD.	PART NUMBER	7804K129
http://www.mcmaster.com		© 2007 McMaster-Carr Supply Company	
Type 440C Stainless Steel Flanged Double Shielded Ball Bearing			
Unless otherwise specified, dimensions are in millimeters. Information in this drawing is provided for reference only.			

Figure B-4. Flanged ball bearing data sheet.

Part Number:	9637K31
Type	Continuous-Length Compression Springs
Material	Steel
Steel Type	Spring-Tempered Steel
System of Measurement	Inch
Outside Diameter	.781"
Wire Size	.062"
Overall Length	11"
Ends	Open
Wire Type	Round Wire
Coils Per Inch	4
Constant	57.2
Note	To determine how many inches long your spring should be, take the spring constant and divide it by the number of coils per inch. Then take this value and divide it by your desired spring rate in lbs./inch. To cut spring, use an abrasive cutoff saw.
Specifications Met	Not Rated

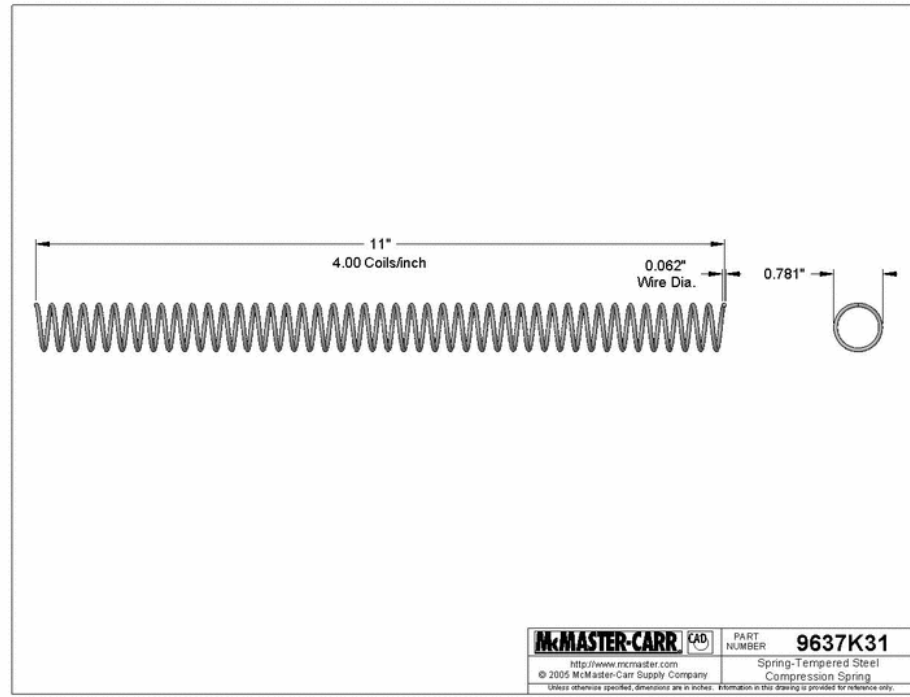
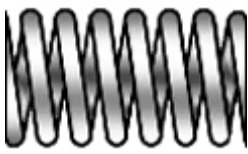


Figure B-5. Normally unlocked spring data sheet.



Part Number: [9435K152](#)

Type	Precision Compression Springs
Material	Stainless Steel
Stainless Steel Type	Type 302 Stainless Steel
System of Measurement	Inch
Outside Diameter	.48"
Outside Diameter Tolerance	$\pm .008"$
Wire Size	.055"
Overall Length	1-1/2"
Compressed Length	.565"
Ends	Closed and Ground
Wire Type	Round Wire
Load	13.19 lbs.
Deflection at Load	.72"
Rate	18.33 lbs./inch
Rate Tolerance	$\pm 8\%$ lbs./in.
Specifications Met	Federal Specification (FED)
Federal Specification	QQ-P-35

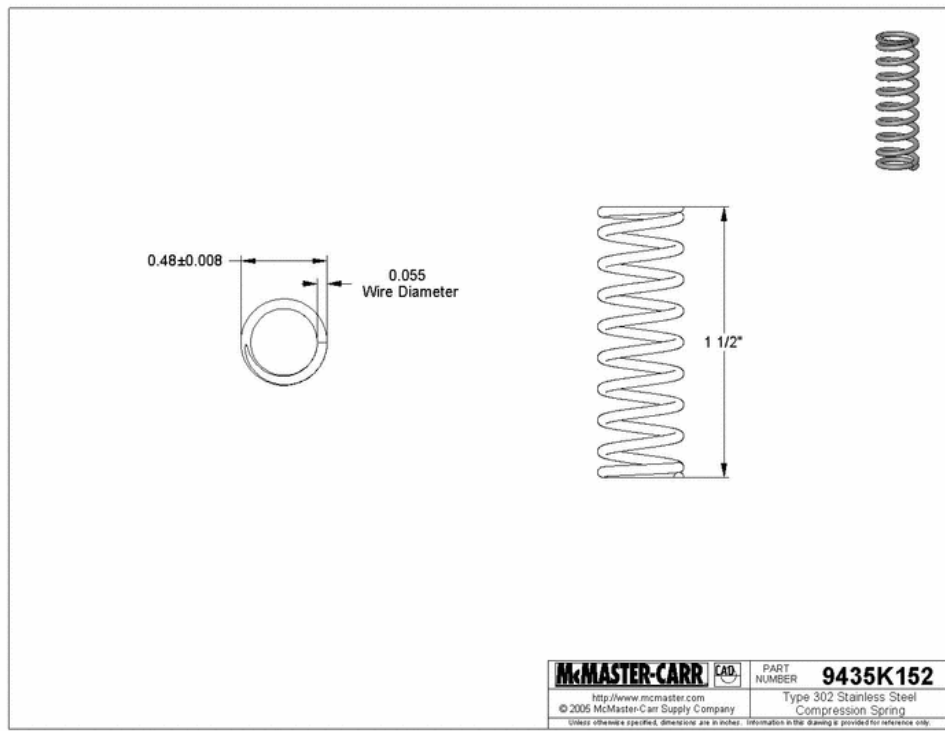


Figure B-6. Normally locked spring data sheet.

APPENDIX C

MATLAB SIMULINK MODELS

Wafer Disc Brake and Dynamometer Controller

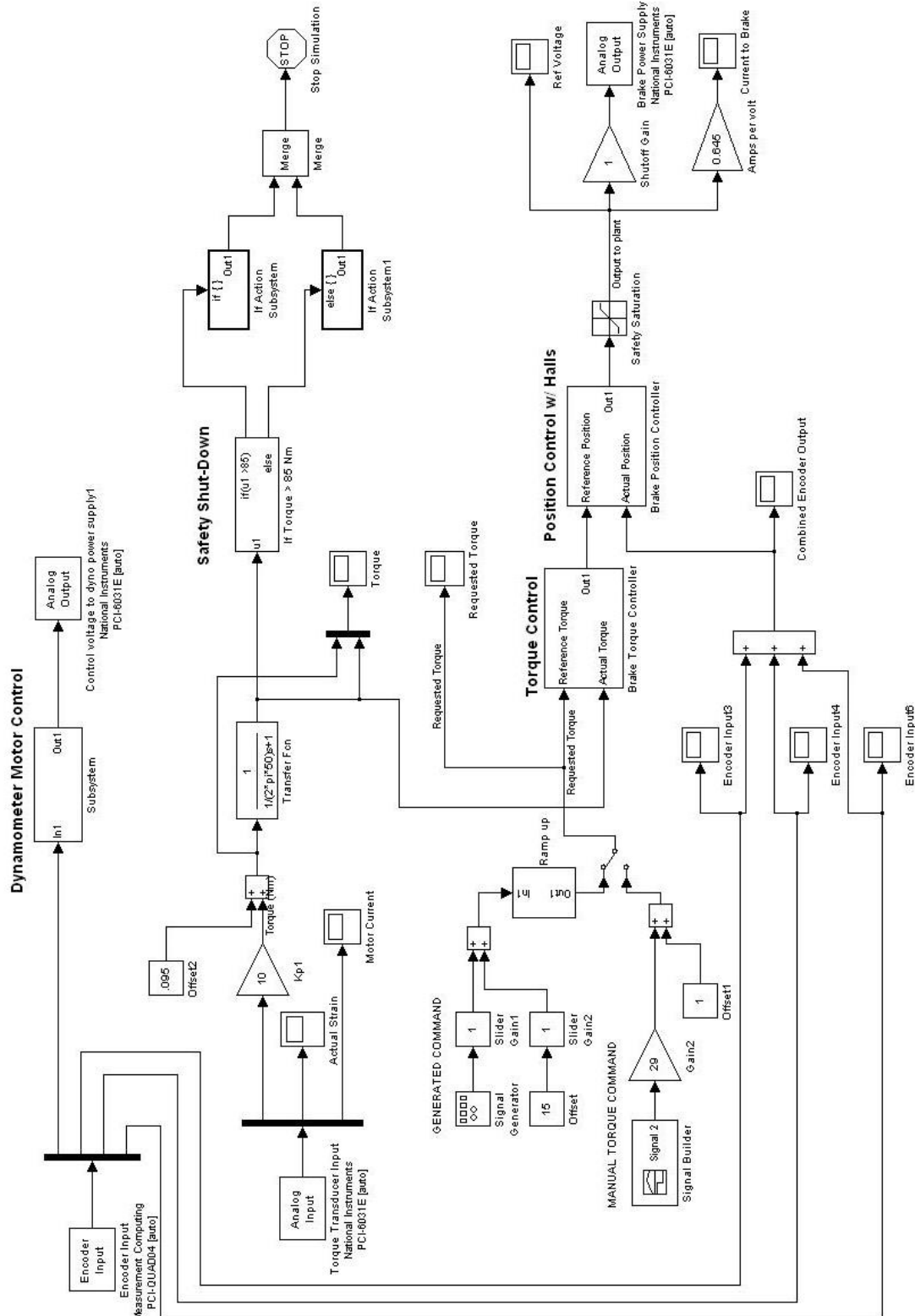


Figure C-1. Simulink diagram of wafer disc brake and dynamometer controller.

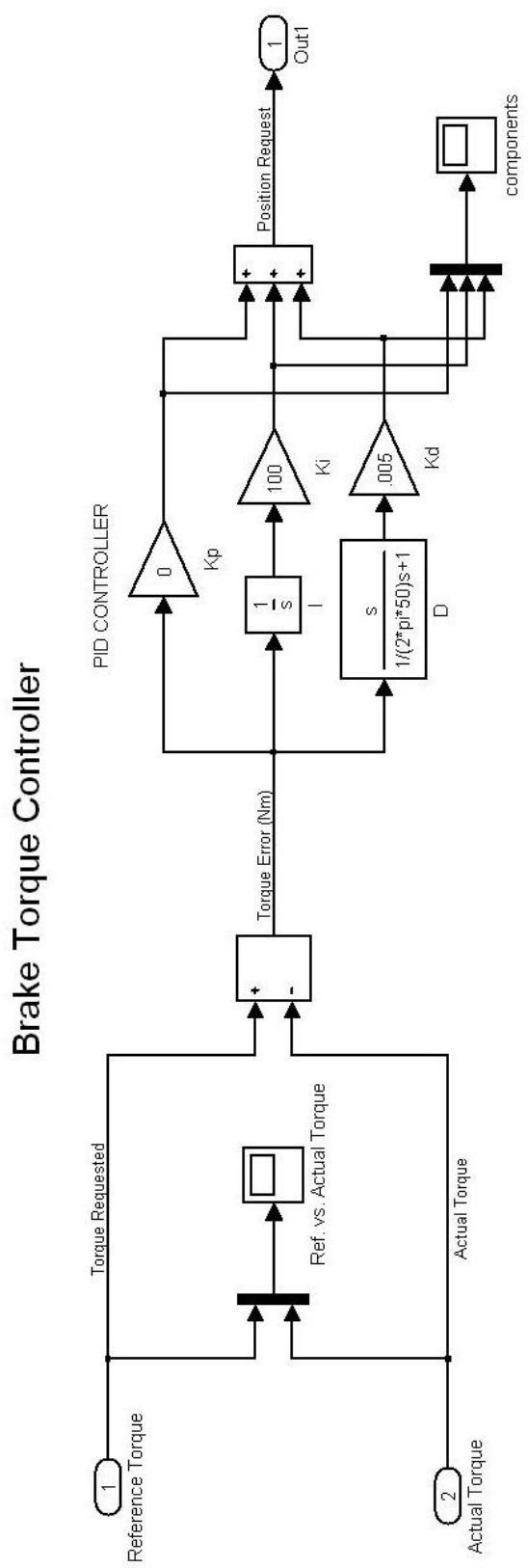


Figure C-2. Simulink diagram of brake torque controller.

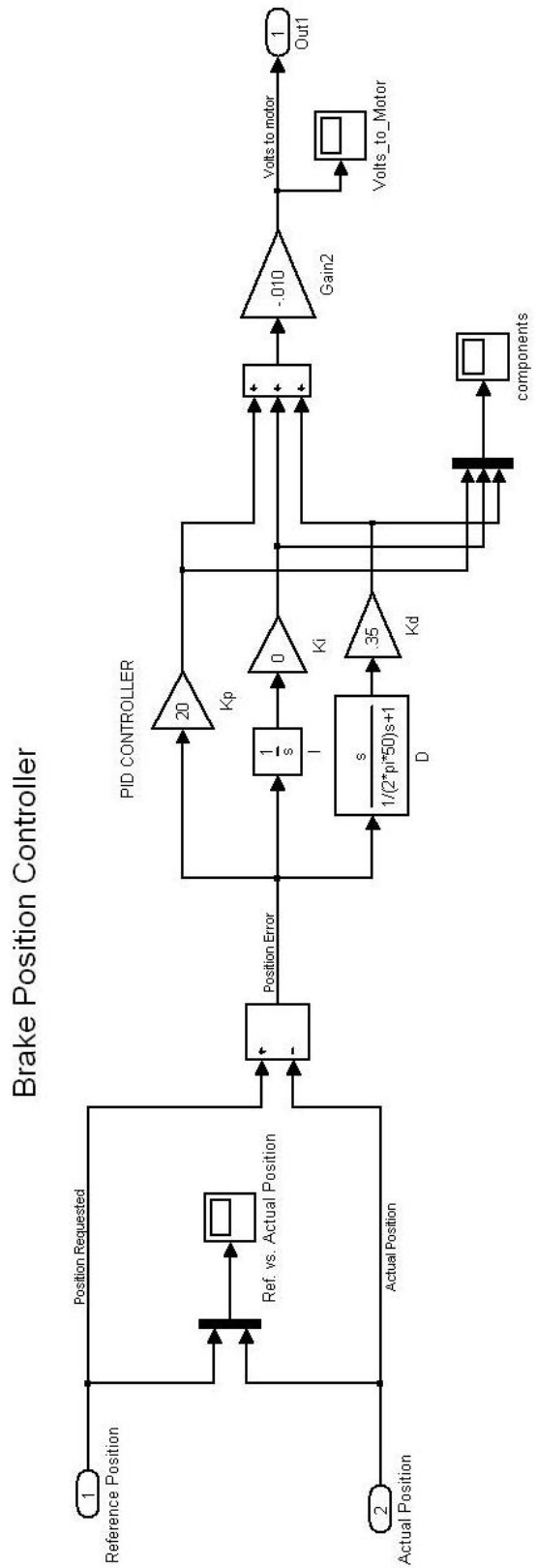


Figure C-3. Simulink diagram of brake position controller.

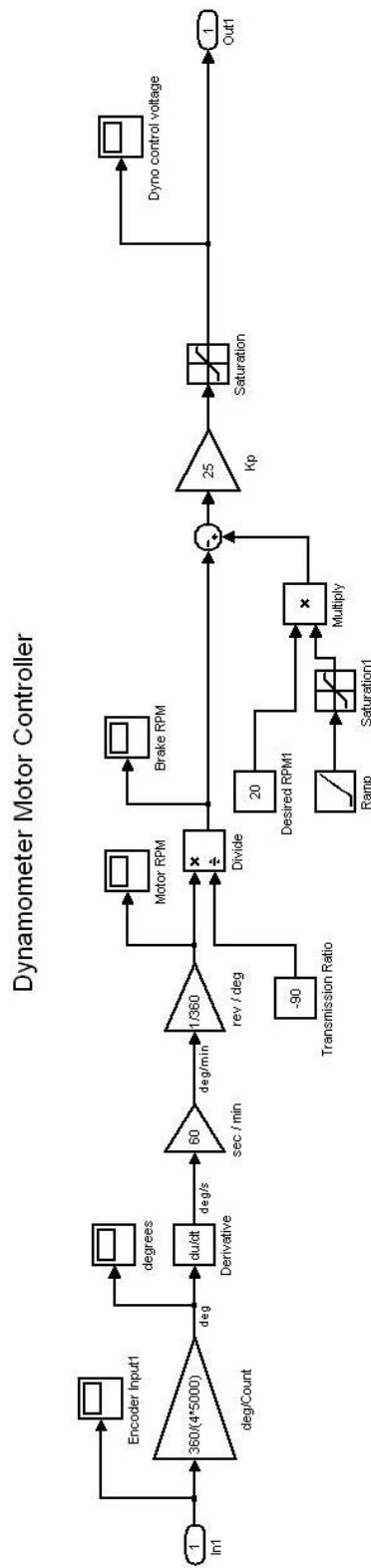


Figure C-4. Simulink diagram of dynamometer motor controller.

APPENDIX D

MANUSCRIPT II: DESIGN AND SIMULATION OF A JOINT COUPLED ORTHOSIS FOR REGULATING FES-AIDED GAIT

Ryan J. Farris, Hugo A. Quintero, Thomas J. Withrow, and Michael Goldfarb

Department of Mechanical Engineering

Vanderbilt University

Nashville, TN 37235

Accepted as a Technical Paper to the

2009 IEEE International Conference on Robotics and Automation

1. Abstract

A hybrid functional electrical stimulation (FES)/orthosis system is being developed which combines two channels of (surface-electrode-based) electrical stimulation with a computer-controlled orthosis for the purpose of restoring gait to spinal cord injured (SCI) individuals (albeit with a stability aid, such as a walker). The orthosis is an energetically passive, controllable device which 1) unidirectionally couples hip to knee flexion; 2) aids hip and knee flexion with a spring assist; and 3) incorporates sensors and modulated friction brakes, which are used in conjunction with electrical stimulation for the feedback control of joint (and therefore limb) trajectories. This paper describes the hybrid FES approach and the design of the joint coupled orthosis. A dynamic simulation of an SCI individual using the hybrid approach is described, and results from the simulation are presented that indicate the promise of the JCO approach.

2. Introduction

Previous studies have demonstrated that functional electrical stimulation (FES) can effectively restore legged mobility to spinal cord injured (SCI) individuals (with the help of a stability aid), and that such legged mobility can provide significant physiological and psychological benefits to SCI users [1-18]. Despite this, two significant factors have hindered FES-aided gait systems from restoring gait to SCI individuals. The first is the rapid muscle fatigue that results from artificially stimulated muscle contraction [19], and the second is the inadequate control of joint torques necessary to

produce reliable and repeatable limb motion and body support. The former (which significantly influences the latter), is due primarily to the synchronous nature in which artificial stimulation recruits motor units (i.e., is due to lack of neural specificity in the stimulation interface). The net effect is that, when stimulated at a high level of effort and high duty cycle, the muscle quickly (i.e., over tens of seconds) loses its ability to generate force [12]. Both issues (rapid onset of fatigue and poor controllability) can potentially result in collapse of the individual, a condition that is unacceptable in any viable gait restoration system. Additionally, FES-aided gait systems (and especially surface-based systems) generally provide stimulation for degrees of freedom in the sagittal plane, but do not provide control over several other degrees-of-freedom associated with gait, such as hip abduction and adduction in the frontal plane. A lack of control authority in this plane can result in one foot crossing in front of the other (i.e., scissoring), which is a condition that is not easily rectified by the user, and in fact often requires external assistance.

Due primarily to these challenges (i.e., the potential of collapse from muscle fatigue and the need to guide uncontrolled degrees of freedom), hybrid systems, which combine FES with an orthosis, appear to offer the greatest promise for commercially viable gait restoration systems. As such, recent efforts by various researchers have focused (and are focusing) on the development of hybrid systems (e.g., [20-23]). This paper describes a hybrid FES approach that addresses the shortcomings of muscle fatigue and limb trajectory control. The approach utilizes surface stimulation of only the quadriceps muscle group of each leg, along with an energetically passive, controllable

orthosis which 1) unidirectionally couples hip to knee flexion; 2) aids hip and knee flexion with a spring assist; and 3) incorporates sensors and modulated friction brakes, which are used in conjunction with electrical stimulation for the feedback control of joint (and therefore limb) trajectories.

3. Joint-Coupled Controlled-Brake Orthosis (JCO)

The authors are developing a joint-coupled controlled brake orthosis (JCO), shown in Fig. D-1, for regulating FES-aided gait. The JCO incorporates multiple features, which serve multiple functions. First, the JCO incorporates unidirectional joint coupling between knee and hip flexion, such that knee flexion generates hip flexion. Since the coupling is unidirectional, however, knee extension does not generate hip extension. The JCO also includes a biasing spring, such that the knee joint (and due to coupling, also the hip joint) is biased toward an equilibrium position in which both the knee joint and the hip joint are flexed. The combination of the (unidirectional) joint coupling and the biasing spring enables knee flexion, hip flexion, and knee extension, all from surface stimulation of only the quadriceps muscle group of each leg. The quadriceps muscle group is among the most powerful and easiest (in the lower limb) to access via surface stimulation, and thus provides a convenient source of metabolic power for gait. In addition to the joint coupling and biasing spring, the JCO incorporates controllable friction brakes at both knees and hips, which can either independently lock these joints (i.e., to provide for “isometric” muscle contraction), or can modulate the resistive torque at each joint for purposes of controlling limb motion. The JCO also contains angle

(and thus also angular velocity) sensing at both hips and knee, which provide essential information for purposes of feedback control of limb motion. Finally, the JCO constrains motion along uncontrolled degrees-of-freedom (e.g., ankle flexion and hip adduction) which enhances the controllability and stability of gait.

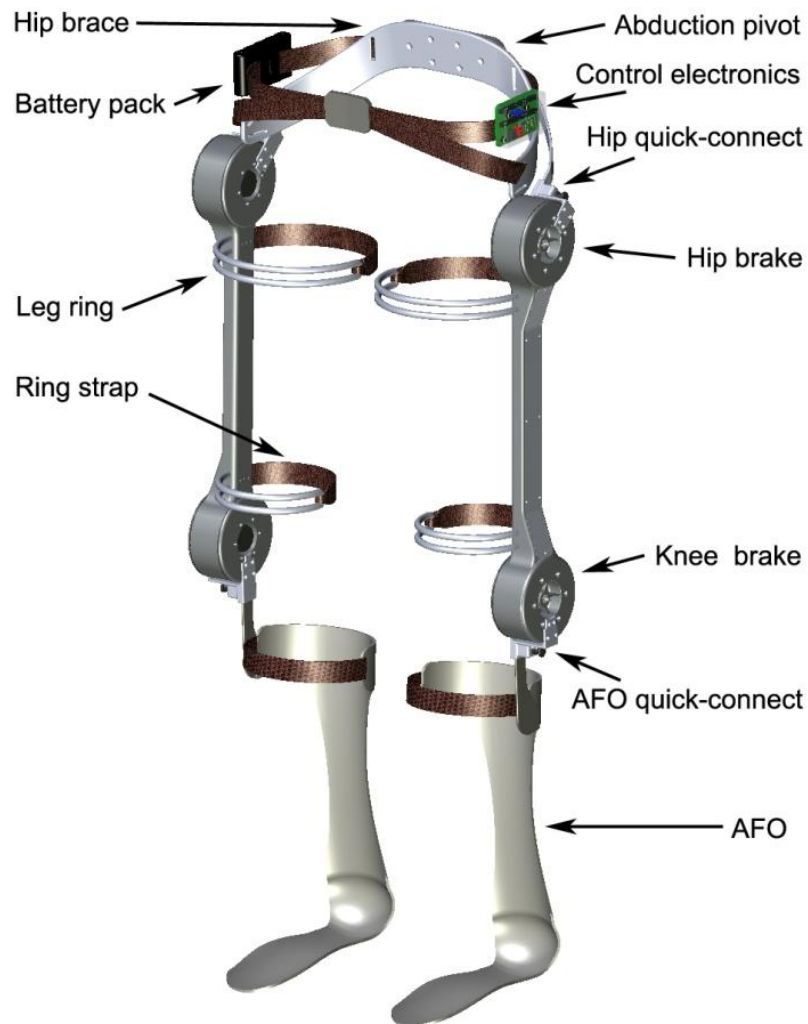


Figure D-1. Solid model of JCO concept.

3.1 *The JCO Gait Sequence*

The gait control approach is described subsequently in the section on gait control and simulation, but is described briefly here to motivate the design of the JCO. Postural stability during gait is provided by a stability aid, such as a walker. The knee of each leg is locked by the controllable friction brakes during stance. Swing is initiated by unlocking the swing leg knee brake, which releases the energy in the biasing spring, which flexes the knee joint and (due to the joint coupling) also flexes the hip joint. During the second half of the swing phase, the hip is locked by the hip brake while the knee is extended by stimulating the quadriceps group. This knee extension (due to stimulation of the quadriceps) does not, however, generate ipsilateral hip extension, since the (cable-based) coupling is unidirectional. Once the knee is fully extended, it remains locked (by the knee brake) during the stance phase of gait.

3.2 *Joint Coupling Design*

The purpose of the joint coupling is to provide hip flexion necessary to generate forward leg motion, which is otherwise a challenge, due to the inaccessibility of the deep hip flexor muscles via surface stimulation. The JCO design incorporates a Bowden cable which spans the inside of the femur link and attaches to the hip and knee rotors on either end (see Fig. D-2). Cable crimps are used in the hip brake as hard stops in only one direction of rotation, which provides unidirectional coupling of knee flexion to hip flexion. During knee extension, the distal end of the inner Bowden cable winds around the inner hip brake rotor without inducing concurrent hip extension.

As previously mentioned, the power for knee (and therefore hip) flexion is provided by the quadriceps, but is stored in an extension spring housed within the femur tube (also in Fig. D-2). This spring is attached to the returning end of the Bowden cable which is wrapped around the knee brake rotor, thus creating a torque in the direction of knee flexion as determined by the spring stiffness, equilibrium point, and preload (against a joint hard stop).

3.3 *Wafer Disc Brakes*

A key component of the JCO is the wafer disc brake, which serves a threefold purpose: 1) provide added safety via the normally “locked” design of the knee brake, which will prevent the wearer from falling should the device lose power; 2) increase muscle efficiency by locking joints during phases of gait when they are normally static, thus taking the burden of support off the leg muscles, reducing muscle fatigue and allowing longer walking times; and 3) smooth and control leg trajectories for a more natural and repeatable gait by utilizing the brakes as variable dampers controlled in relation to joint angle feedback. A previous effort to create a controlled brake orthosis [20, 24, 25] utilized magnetic particle brakes, which require electrical power to impose resistive torque. In the event of a power failure, the brakes (and thus the orthosis joints) remain unlocked, which could result in collapse and serious injury to the individual. The authors have developed a new type of brake, called a wafer disc brake (WDB), which provides approximately 45 times the torque-to-weight ratio of state-of-the-art magnetic particle brakes, and importantly, can be designed in either a “normally locked” mode or

“normally unlocked” mode. Since the knee joints should fail in a locked mode, as previously mentioned, the knee brakes are thus of the normally locked type. Since the hip brakes are used primarily for trajectory control and are characterized by relatively low duty cycle operation, the hip brakes are of the normally unlocked type. Designing knee brakes to be normally locked and hip brakes to be normally unlocked both minimizes electrical power consumption (based on data from [25], and importantly prevents collapse during an electrical power failure. The normally unlocked WDB, which was designed for the hip joint, consists of a stack of thin high-strength plastic wafers which are alternatively coupled (through splines) to the brake stator and rotor. A small brushless motor located inside the brake shaft transmits a compressive force through a ball screw to the stack. Assuming relatively low friction in the ball screw, the stack is subjected to a compressive force which is proportional to the motor current. Due to the series arrangement of discs, the resistive torque on the rotor is the product of the compressive force, the mean radius of contact, and the coefficient of friction, which is amplified by the number of interfaces between discs. Since the hip brake contains 61 discs, the effective hip torque is increased by a gain of 60. The net result is a proportional brake that provides a significantly greater torque-to-weight ratio than a state-of-the-art magnetic particle brake. Since the ball screw is back-drivable, the brake torque remains in proportion to the motor current, and thus is proportional in nature. The normally locked type of WDB, which is used for the knee joint, is shown in cross-section in Fig. D-3. A photo of the corresponding assembled prototype is shown in Fig. D-4. The design is similar to the normally unlocked type, but the discs are preloaded

with a compression spring. Applying current to the motor proportionally unloads the preload, such that full brake torque occurs at zero motor current, and minimum brake torque occurs at full motor current. Since the ball screw is back-drivable, the brake torque remains in inverse proportion to the motor current.

A first-generation prototype of the knee brake has been constructed and tested. The mass of this brake is 0.73 kg. The brake was experimentally measured to provide a maximum torque of 50.7 N-m, which provides a resistive torque-to-weight ratio of 69.4 N-m/kg. In comparison, a state-of-the-art magnetic particle brake (MPB) in a similar size range provides a torque of 1.7 N-m with a mass of 1.14 kg, and as such has a resistive torque-to-weight ratio of 1.5 N-m/kg (e.g., Placid Industries model no. B15). As such, the WDB has a torque-to-weight ratio approximately 45 times greater than the MPB. Experimental measurements further indicate a minimum torque of 0.16 N-m (i.e., the brake dynamic range is between approximately 0.16 and 50 N-m). For both brakes, the torque varies linearly (and inversely, for the knee brake) with input current.

3.4 Ankle Support

The JCO utilizes an ankle-foot-orthosis (AFO) at the ankle, which is sufficiently compliant to allow dorsiflexion during the stance phase of gait, but sufficiently stiff to prevent foot drop during the swing phase of gait. Current gait simulations indicate a stiffness of 15 Nm/rad (for a 75 kg user) provides an appropriate balance between these objectives.

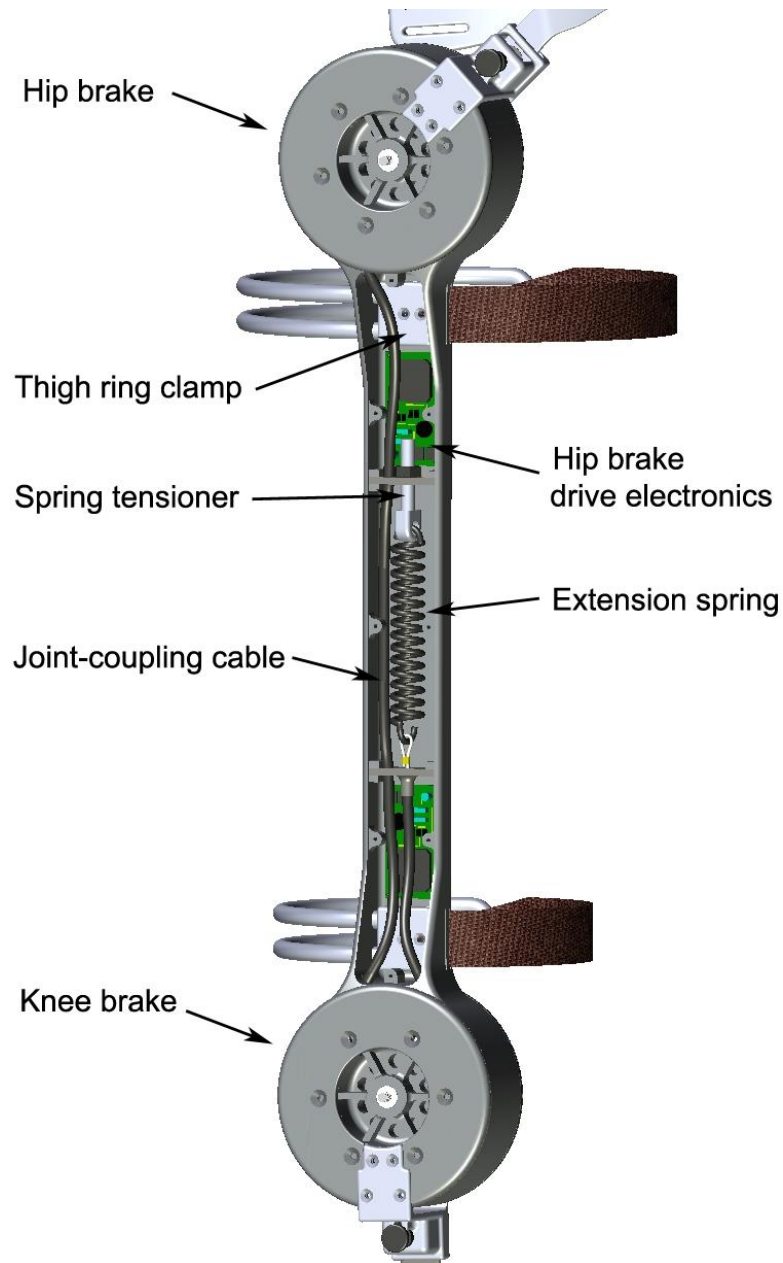


Figure D-2. Femur link detail.

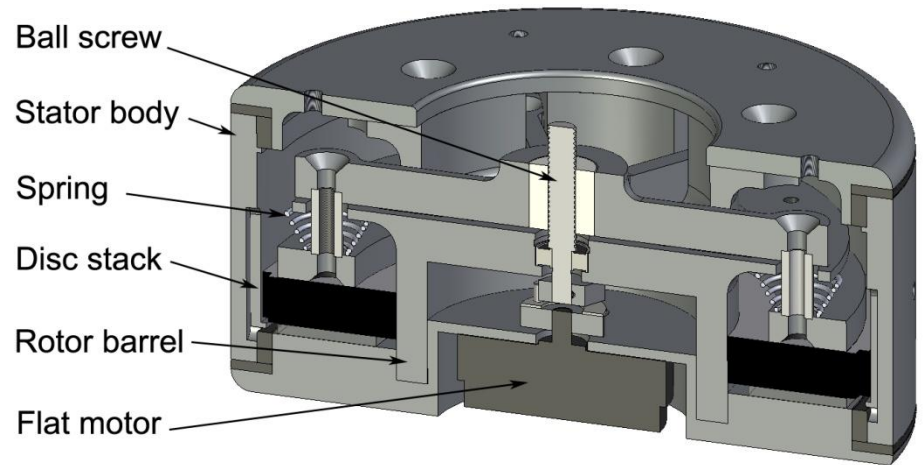


Figure D-3. Cross-section of normally locked knee brake.

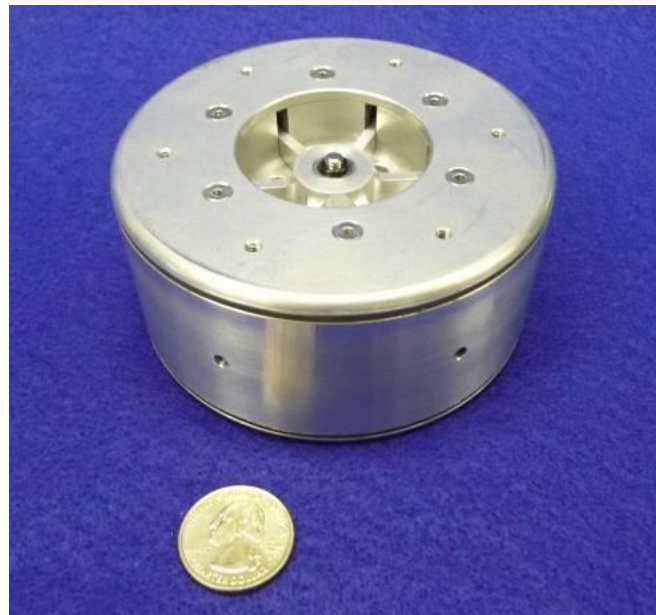


Figure D-4. Fully functional knee brake prototype.

3.5 *Mass and Inertia*

The total orthosis mass as shown in Fig. D-1, based on the solid model and prototypes of the brakes, is approximately 6 kg (13 lbs). Approximately one half of the orthosis weight is located on the pelvis, and thus does not add significantly to the rotational inertia or gravitational loads of the lower limbs. The rotational inertia of the distal link of the orthosis about the knee joint is approximately 5% of a typical shank inertia, while the inertia of the proximal link about the hip joint is about 10% of a typical thigh inertia.

4. Gait Control and Simulation

A dynamic simulation of an SCI individual walking with the JCO and a walker was conducted to 1) validate that the proposed approach can provide a safe and stable gait, 2) develop a robust gait controller, 3) explore variation of primary JCO design parameters, namely, the joint coupling transmission ratio and the spring stiffness, preload, and equilibrium point, 4) assess the magnitude of torque and duty cycle of stimulation required of the quadriceps group (which will help characterize the extent of expected muscle fatigue), and 5) assess the load borne by the arms (through the walker) relative to that carried by the legs.

The dynamic simulator has two main parts — the human body model and the gait controller. The human body model is based in classical rigid body dynamics and is composed of seven segments and six articulations in three dimensional space, as shown in Fig. D-5. The associated geometric and inertial parameters normalized to a body

height and mass, as given by [26], are listed in Table 1. The spatial model has 12 degrees of freedom, which is reduced to fewer when the feet are in contact with the ground. The model is influenced by 10 inputs, 6 of which are produced by the hybrid orthosis system (i.e., torques in the sagittal plane for both ankles, knees, and hips, applied by a combination of muscle stimulation and JCO input), and 4 of which result from the interaction between the user and the walker (i.e., one torque in the sagittal plane and three forces, all applied symmetrically at the shoulder joints, which are located atop the torso link). Note that the floor is modeled in the vertical direction as a unidirectional stiff spring and damper, such that the feet do not penetrate significantly into the floor (i.e., foot/floor penetration is on the order of a millimeter). In the horizontal direction, the foot/floor interaction is governed by Coulomb friction, where the coefficient of friction is assumed to be 0.3.

4.1 Walker Model

The user walks with the JCO on a flat and level surface with the aid of a regular walker. Note that the use of a walker assumes sufficient upper limb function to do so. The shoulder force in the frontal plane is modeled as a spring and damper with equilibrium point at the vertical orientation, which stabilizes the torso in the frontal plane (i.e., prevents “falling” in that plane). The remaining shoulder inputs, which are all sagittal plane inputs, are constrained by the nature of the walker. Specifically, the vertical force is restricted to act only in the upward direction (i.e., the user cannot pull up on the walker); the horizontal force is restricted by the coefficient of friction

between the walker and floor (assumed to be 0.3) and the vertical force; and the horizontal force and shoulder moment are additionally constrained by the structural stability (i.e., tipping point) of the walker.

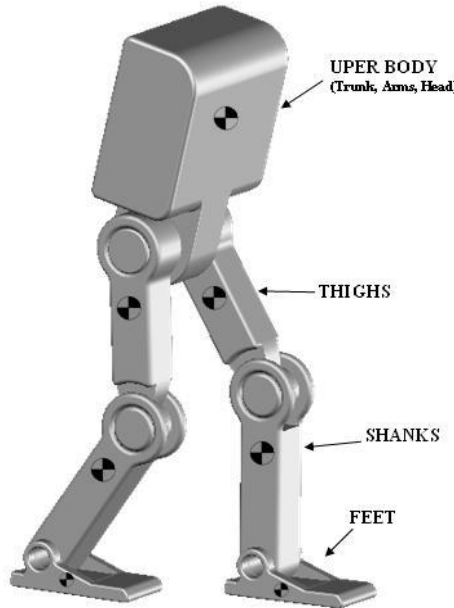


Figure D-5. Dynamic simulation solid model, showing the six joint degrees of freedom.

Table D-1. Simulation parameters.

Segment	Relative Length * (l / L)	Distance to Mass Center **	Relative Mass * (m / M)	Relative Inertia (I / L)
Upper Body	0.29	0.64	0.65	0.50
Thigh	0.23	0.43	0.11	0.32
Shank	0.22	0.40	0.05	0.30
Foot	0.13	0.25	0.02	0.48

* L = High, M= Mass of subject

** The distance is a fraction of the segment longitude

All units are in the MKS system

4.2 Orthosis Model

Since the JCO utilizes an AFO at the ankles, ankle inversion/eversion is not considered, while flexion/extension torques are modeled as a torsional spring and damper about zero degrees of flexion. Thus, the ankle is not a “controlled” degree of freedom. The knee torques result from a combination of quadriceps stimulation, joint coupling, the knee joint spring, and the resistive torque of the brake. These are combined as described in the gait controller below. The hip torques result from the joint coupling and the hip brakes. Specifically, the hip joint coupling is modeled as a flexor torque that has the function to maintain the hip angle equal to the knee angle (in the case of a knee-angle/hip-angle coupling ratio of 1:1), although only in extension. In the model, the abduction-adduction movement is locked in the zero position. Note that the orthosis allows hip abduction/adduction with a limit stop on excessive adduction (to prevent crossing over). This degree of freedom was not modeled in the simulation, since frontal plane dynamics are assumed to be controlled by the user via the walker, and thus are represented as a simplified single degree-of-freedom (i.e., rotation in the frontal plane).

4.3 Control Algorithm

In the proposed system, two controllers are simultaneously active, which are the JCO controller (i.e., brakes and electrical stimulation) and the user controller, which governs interaction with the walker through the arms (i.e., shoulder forces and torques). The control algorithm is a loop consisting of four states (Fig. D-6):

4.4 S1 : State 1

In the initial condition, both knee brakes are locked in zero degrees of flexion. The support leg is in front of the swing leg. The upper body can rotate freely at the hips. The user rotates the upper body forward to an angle of 20 degrees, at which point the support hip brake is locked. At that moment the center of mass is in front of the support foot, which causes forward motion and a rotation around the front foot. The controller switches to the next state when the support leg is vertical and the user has raised the torso using the walker.

4.5 S2 : State 2

The swing knee brake is unlocked; this allows the spring to flex the knee, and the hip is concurrently flexed due to the joint coupling. During this state, the user maintains control of upper body orientation to approximately vertical. The stance hip brake allows hip extension (and not flexion) to zero degrees (at which point it will lock), while the stance knee brake remains locked. The controller switches to the next state when the difference between hip angles ceases to increase.

4.6 S3 : State 3

The swing hip is locked while the swing knee is extended via quadriceps stimulation. The stance knee remains locked while the stance hip does not allow extension beyond zero degrees. The controller switches to the next state when the swing knee is fully extended.

4.7 S4 : State 4

The swing knee is locked and the swing foot lands due to gravity and user arm control. The stance hip is free. The swing hip allows flexion such that the upper body leans forward 20 degrees from the vertical (as in state 1). The swing leg is now in front and becomes the stance leg; as such the system is returned to state 1 and ready for another step.

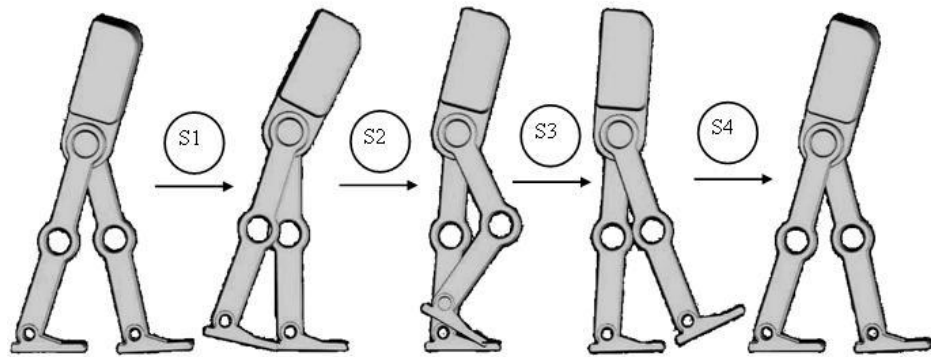


Figure D-6. Simulation states.

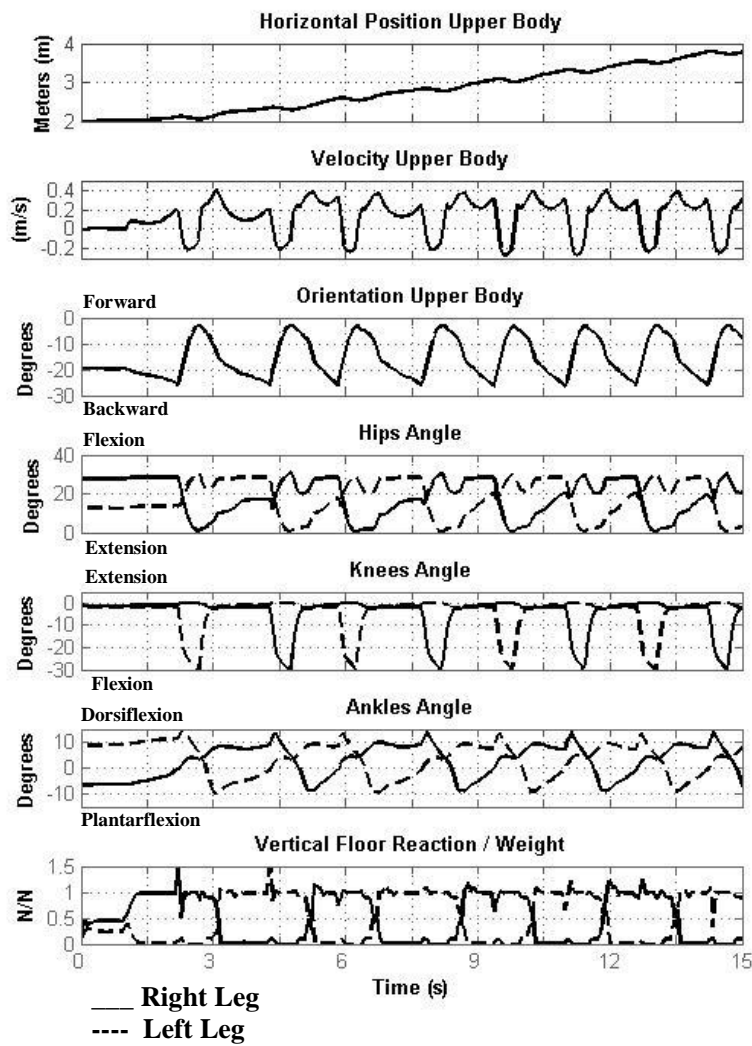


Figure D-7. Simulation results.

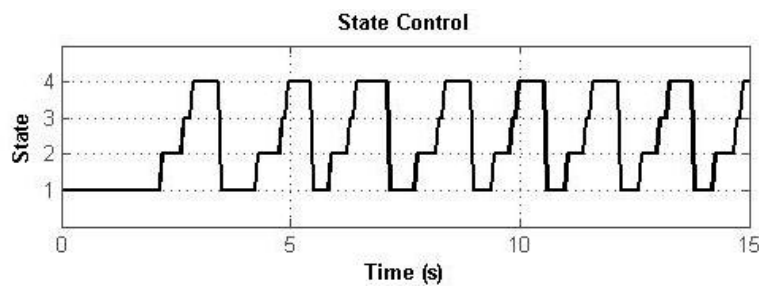


Figure D-8. Procession of simulation states.

4.8 *Simulation Results*

A simulation of the JCO and gait controller was conducted using the parameters given in Table 1, for a user of height L=1.7m and mass M=65kg. Figure D-7 shows the results of fifteen seconds of simulation, including position and joint angle data and ground reaction force data. A video of the simulated walk is included in the supporting material. Note that the user starts from rest, and remains at rest for the first second of the simulation. The cadence of the resulting gait was 34 steps per minute and the average velocity was 0.2 m/s. The upper body never leans backward and the maximum forward inclination is around 25 degrees. The simulation further indicates that nearly all the weight is carried by the legs, and thus the approach results in minimal weight bearing on the arms (i.e., the arms are used chiefly for stabilization and not for support purposes). Finally, Fig. D-8 shows the evolution of states through the simulation. As indicated in the figure, the duration of electrical stimulation (stage 3), is small compared with total cycle. The ratio is 0.1:3.5 seconds, which equates to a quadriceps duty cycle of approximately 3%.

5. Preliminary Experiments

The authors have conducted preliminary experiments to test the joint coupling concept, and to assess the extent of fatigue imposed by the bias spring and joint coupling. A simple, one-legged version of the orthosis was created which included one-to-one joint coupling between the hip and knee, an adjustable extension spring for knee flexion, potentiometers on the hip and knee joints for angle measurement, and a locking

knee joint with quick release pin. Experiments were conducted to 1) determine if the spring and joint coupling could provide sufficient knee and hip flexion in the context of stride, and 2) determine if the quadriceps could repeatably provide the power necessary to overcome the spring and extend the lower leg without significant fatigue. The first experiment (see Fig. D-9) involved positioning an able-bodied subject in stance such that the leg wearing the orthosis was in the rear and ready to begin stride. The spring was loaded and the knee was locked in the extended position by means of a quick connect pin. As the pin was pulled by an assistant, the leg swung forward in knee and hip flexion as shown in Figs. D-9 and D-10. At the peak of hip flexion, the quadriceps was stimulated, which fully extended the knee and—in this test, due to the absence of a hip brake—allowed the hip to extend as well, dropping the foot to the ground. The results of this experiment showed that joint angles comparable to those typical in healthy subjects could be obtained involuntarily with the JCO system (see Fig. D-10).

The second experiment involved conducting extended sets of pulsed quadriceps stimulation at a duty cycle of 15%—conservative according to simulations. Ten subjects underwent three five minute periods of stimulation with a rest period in between each trial of three minutes. Results from this preliminary fatigue testing showed that muscle output decreased 7% over five minutes for all the trials combined and averaged. As such, the quadriceps appears to be quite capable of providing sustained power for the proposed hybrid approach without significant degradation of performance.



Figure D-9. FES/JCO generated gait sequence experiment.

Frame 1: Right leg is locked in shown position. Assistant pulls pin to unlock the knee joint. **Frames 2-5:** Once pin is pulled, the spring pulls the knee into flexion and the joint coupling therefore pulls the hip into flexion as well. Frame 5 is the final resting state under no muscle contraction. **Frames 6-8:** The quadriceps is stimulated by a momentary push button switch on the walker handle. This causes the knee to extend and therefore relieve the joint coupling, allowing the hip to extend also. Frame 8 is the final resting position of the leg after it has rejoined the ground after stride.

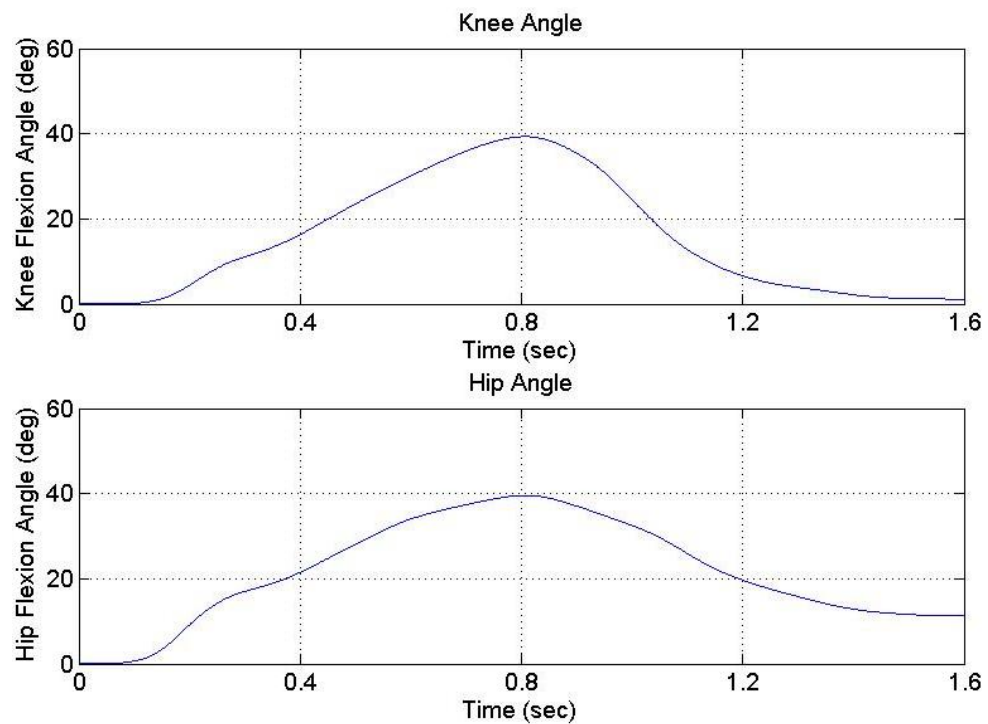


Figure D-10. Joint angle data during gait experiment shown in Fig. D-9.

6. Conclusion

A joint-coupled controlled brake orthosis (JCO) has been designed as part of a hybrid FES/orthosis system for restoring gait to spinal cord injured individuals. This device will 1) unidirectionally couple hip to knee flexion; 2) aid hip and knee flexion with a spring assist; and 3) incorporate sensors and modulated friction brakes, which are used in conjunction with electrical stimulation for the feedback control of joint (and therefore limb) trajectories. Dynamic simulations and a one-legged prototype of the orthosis were used to validate the design concepts and aid in the design development. The results of these efforts showed that robust walking can be achieved via the orthosis without significant muscle fatigue. Future work includes characterization of the latest brake prototype, development of a fully functional, two-legged JCO, control design and the addition of on-board electronics, and clinical trials of the JCO system.

7. References

- [1] Axelson PW, Gurski D, and Lasko-Harvill A. "Standing and its importance in spinal cord injury management." In Proceedings of the RESNA 10th Annual Conference, pp. 477-479, 1987.
- [2] Gruner J, Glaser RM, Feinberg SD, Collins SR, and Nussbaum NS. "A system for evaluation and exercise-conditioning of paralyzed leg muscles." J. Rehabilitation R&D, vol. 20, no. 1, pp. 21-30, 1983.
- [3] Turk R and Obreza P. "Functional electrical stimulation as an orthotic means for the rehabilitation of paraplegic patients." Paraplegia, vol. 23, no. 6, p. 345, 1985.
- [4] Phillips L, Ozer M, Axelson P, and Chizek H. "Spinal cord injury: A guide for patient and family." Raven Press, 1987.

- [5] Ragnarsson K. "Physiologic effects of functional electrical stimulation induced exercises in spinal cord-injured individuals." *Clin. Orthop. Rel. Res.*, vol. 233, pp. 53-63, 1988.
- [6] Kaplan P, Gandhavadi B, Richards L, and Goldschmidt J. "Calcium balance in paraplegic patients: Influence of injury duration and ambulation." *Archives of Physical Medicine and Rehabilitation*, vol. 59, pp. 447-450, 1978.
- [7] Odeen I and Knutsson E. "Evaluation of the effects of muscle stretch and weight load in patients with spastic paraparesis." *Scandinavian Journal of Rehabilitative Medicine*, vol. 13, pp. 117-121, 1981.
- [8] Triolo RJ and Bogie K, "Lower Extremity Applications of Functional Neuromuscular Stimulation After Spinal Cord Injury," *Topics in Spinal Cord Injury Rehabilitation*, vol. 5, pp. 44-65, 1999.
- [9] Creasey GH, Ho CH, Triolo RJ, Gater DR, DiMarco AF, Bogie KM, and Keith MW, "Clinical applications of electrical stimulation after spinal cord injury," *J Spinal Cord Med*, vol. 27, pp. 365-75, 2004.
- [10] Cybulski G, Penn R, and Jaeger R, "Lower extremity functional neuromuscular stimulation in cases of spinal cord injury," *Neurosurgery*, vol. 15, pp. 132-146, 1984.
- [11] Muller EA. "The influence of training and inactivity on muscle strength." *Archives of Physical Medicine and Rehabilitation*, vol. 51, p. 449, 1978.
- [12] Pacy PJ, Evans RH, and Halliday D. "Effect of anaerobic and aerobic exercise promoted by computer regulated functional electrical stimulation (FES) on muscle size, strength and histology in paraplegic males." *Prosthetics and Orthotics International*, vol. 11, no. 2, p. 78, 1987.
- [13] Pacy PJ, Hesp R, Halliday D, Kath D, Cameron G, and Reeve J. "Muscle and bone in paraplegic patients, and the effect of functional electrical stimulation." *Clinical Science*, vol. 75, pp. 481-487, 1988.
- [14] Stefancic M, Kralj A, Turk R, Bajd T, Benko H, and Segal J. "Neurophysiological background of the use of functional electrical stimulation in paraplegia." *Electromyogr. Clin. Neurophysio.*, vol. 26, nos. 5/6, p. 433, 1986.
- [15] Gallien P, Brissot R, Eyssette M, Tell L, Barat M, Wiart L, Petit H. "Restoration of gait by functional electrical stimulation for spinal cord injured patients. Paraparesis.", vol. 33, pp. 660-664, 1995.

- [16] Brissot R, Gallien P, Le Bot MP, Beaubras A, Laisne D, Beillot J, Dassonville J. "Clinical experience with functional electrical stimulation-assisted gait with Parastep in spinal cord-injured patients." *Spine.*, vol. 25, no. 4, pp. 501-508, 2000.
- [17] Guest RS, Klose KJ, Needham-Shropshire BM, Jacobs PL. "Evaluation of a training program for persons with SCI paraplegia using the Parastep 1 ambulation system: part 4. Effect on physical self-concept and depression." *Arch Phys Med Rehabil.*, vol. 78, no. 8, pp. 804-807, 1997.
- [18] Nash MS, Jacobs PL, Montalvo BM, Klose KJ, Guest RS, Needham-Shropshire BM. "Evaluation of a training program for persons with SO paraplegia using the Parastep 1 ambulation system: part 5. Lower extremity blood flow and hyperemic response to occlusion are augmented by ambulation training." *Arch Phys Med Rehabil.*, vol. 78, no. 8, pp. 808-814, 1997.
- [19] Benton L, Baker L, Bowman B, and Waters R. "Functional Electrical Stimulation: A Practical Guide, 2nd edition." Professional Staff Association, Rancho Los Amigos Rehabilitation Engineering Center, Rancho Los Amigos Hospital, Downey CA, 1981.
- [20] Goldfarb M, Durfee W, Korkowski K, and Harrold B. "Evaluation of a Controlled-Brake Orthosis for FES-Aided Gait," *IEEE Transactions on Neural Systems and Rehabilitation Engineering*, vol. 11, no. 3, pp. 241-248, 2003.
- [21] Kobetic R, Marsolais EB, Triolo RJ, Davy DT, Gaudio R, and Tashman S, "Development of a hybrid gait orthosis: a case report," *J Spinal Cord Med*, vol. 26, pp. 254-8, 2003.
- [22] To CS, Kirsch RF, Kobetic R, and Triolo RJ. "Simulation of a functional neuromuscular stimulation powered mechanical gait orthosis with coordinated joint locking." *IEEE Transactions on Neural Systems and Rehabilitation Engineering*, vol. 13, no. 2, pp. 227-235, 2005.
- [23] Durfee W and Rivard A, "Design and simulation of a pneumatic, stored energy, hybrid orthosis for gait restoration," *J Biomech Eng*, vol. 127, pp. 1014-9, 2005.
- [24] Goldfarb M. "A controlled brake orthosis for FES-aided gait." PhD Thesis, Massachusetts Institute of Technology, 1994.
- [25] Goldfarb M and Durfee W. "Design of a Controlled-Brake Orthosis for Regulating FES-Aided Gait." *IEEE Transactions on Rehabilitation Engineering*, vol. 4, no. 1, pp. 13-24, 1996.
- [26] Winter DA. "The biomechanics and motor control of human gait: normal, elderly and pathological," University of Waterloo Press, 2nd ed, 1991.

APPENDIX E

MANUSCRIPT III: DESIGN OF A JOINT-COUPLED ORTHOSIS FOR FES-AIDED GAIT

Ryan J. Farris, Hugo A. Quintero, Thomas J. Withrow, and Michael Goldfarb

Department of Mechanical Engineering

Vanderbilt University

Nashville, TN 37235

Accepted as a Technical Paper to the

2009 IEEE International Conference on Rehabilitation Robotics

1. Abstract

A hybrid functional electrical stimulation (FES)/orthosis system is being developed which combines two channels of (surface-electrode-based) electrical stimulation with a computer-controlled orthosis for the purpose of restoring gait to spinal cord injured (SCI) individuals (albeit with a stability aid, such as a walker). The orthosis is an energetically passive, controllable device which 1) unidirectionally couples hip to knee flexion; 2) aids hip and knee flexion with a spring assist; and 3) incorporates sensors and modulated friction brakes, which are used in conjunction with electrical stimulation for the feedback control of joint (and therefore limb) trajectories. This paper describes the hybrid FES approach and the design of the joint coupled orthosis. Preliminary experiments are presented which test the joint coupling concept and assess the extent of quadriceps fatigue imposed by the bias spring and joint coupling.

2. INTRODUCTION

Previous studies have demonstrated that functional electrical stimulation (FES) can effectively restore legged mobility to spinal cord injured (SCI) individuals (with the help of a stability aid), and that such legged mobility can provide significant physiological and psychological benefits to SCI users [1-18]. Despite this, two significant factors have hindered FES-aided gait systems from restoring gait to SCI individuals. The first is the rapid muscle fatigue that results from artificially stimulated muscle contraction [19], and the second is the inadequate control of joint torques necessary to

produce reliable and repeatable limb motion and body support. The former (which significantly influences the latter), is due primarily to the synchronous nature in which artificial stimulation recruits motor units (i.e., is due to lack of neural specificity in the stimulation interface). The net effect is that, when stimulated at a high level of effort and high duty cycle, the muscle quickly (i.e., over tens of seconds) loses its ability to generate force [12]. Both issues (rapid onset of fatigue and poor controllability) can potentially result in collapse of the individual, a condition that is unacceptable in any viable gait restoration system. Additionally, FES-aided gait systems (and especially surface-based systems) generally provide stimulation for degrees of freedom in the sagittal plane, but do not provide control over several other degrees-of-freedom associated with gait, such as hip abduction and adduction in the frontal plane. A lack of control authority in this plane can result in one foot crossing in front of the other (i.e., scissoring), which is a condition that is not easily rectified by the user (i.e., is likely to require external assistance).

Due primarily to these challenges (i.e., the potential of collapse from muscle fatigue and the need to guide uncontrolled degrees of freedom), hybrid systems, which combine FES with an orthosis, appear to offer the greatest promise for commercially viable gait restoration systems. As such, recent efforts by various researchers have focused (and are focusing) on the development of hybrid systems (e.g., [20-23]). This paper describes a hybrid FES approach that utilizes surface stimulation of only the quadriceps muscle group of each leg, along with an energetically passive, controllable orthosis (see Fig. E-1) which 1) unidirectionally couples hip to knee flexion; 2) aids hip

and knee flexion with a spring assist; and 3) incorporates sensors and modulated friction brakes, which are used in conjunction with electrical stimulation for the feedback control of joint (and therefore limb) trajectories.

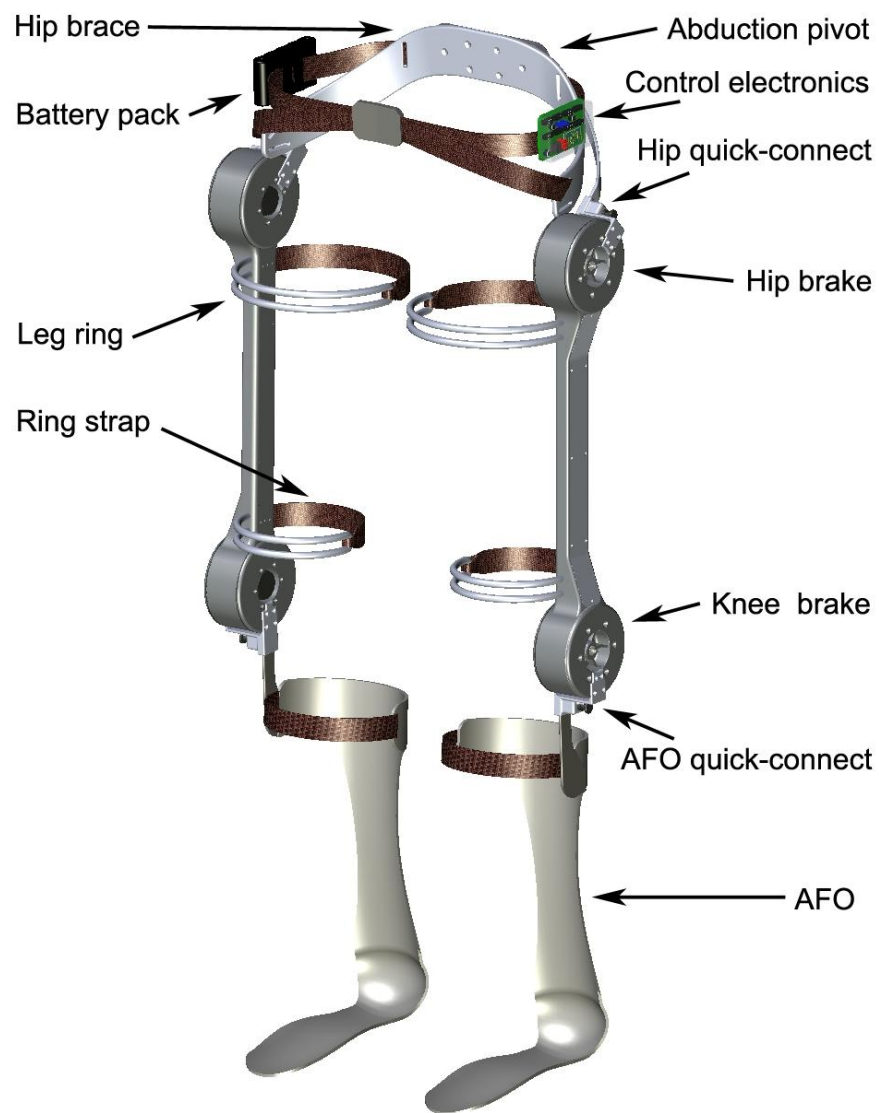


Figure E-1. Solid model of JCO concept.

3. Joint-Coupled Controlled-Brake Orthosis (JCO)

The authors are developing a joint-coupled controlled brake orthosis (JCO) for regulating FES-aided gait. The JCO incorporates multiple features, which serve multiple functions. First, the JCO incorporates unidirectional joint coupling between knee and hip flexion, such that knee flexion generates hip flexion. Since the coupling is unidirectional, however, knee extension does not generate hip extension. The JCO also includes a biasing spring, such that the knee joint (and due to coupling, also the hip joint) is biased toward an equilibrium position in which both the knee joint and the hip joint are flexed. The combination of the (unidirectional) joint coupling and the biasing spring enables knee flexion, hip flexion, and knee extension, all from surface stimulation of only the quadriceps muscle group of each leg. The quadriceps muscle group is among the most powerful and easiest (in the lower limb) to access via surface stimulation, and thus provides a convenient source of metabolic power for gait. In addition to the joint coupling and biasing spring, the JCO incorporates controllable friction brakes at both knees and hips, which can either independently lock these joints (i.e., to provide for “isometric” muscle contraction), or can modulate the resistive torque at each joint for purposes of controlling limb motion. The JCO also contains angle (and thus also angular velocity) sensing at both hips and knee, which provide essential information for purposes of feedback control of limb motion. Finally, the JCO constrains motion along uncontrolled degrees-of-freedom (e.g., ankle flexion and hip adduction) which enhances the controllability and stability of gait.

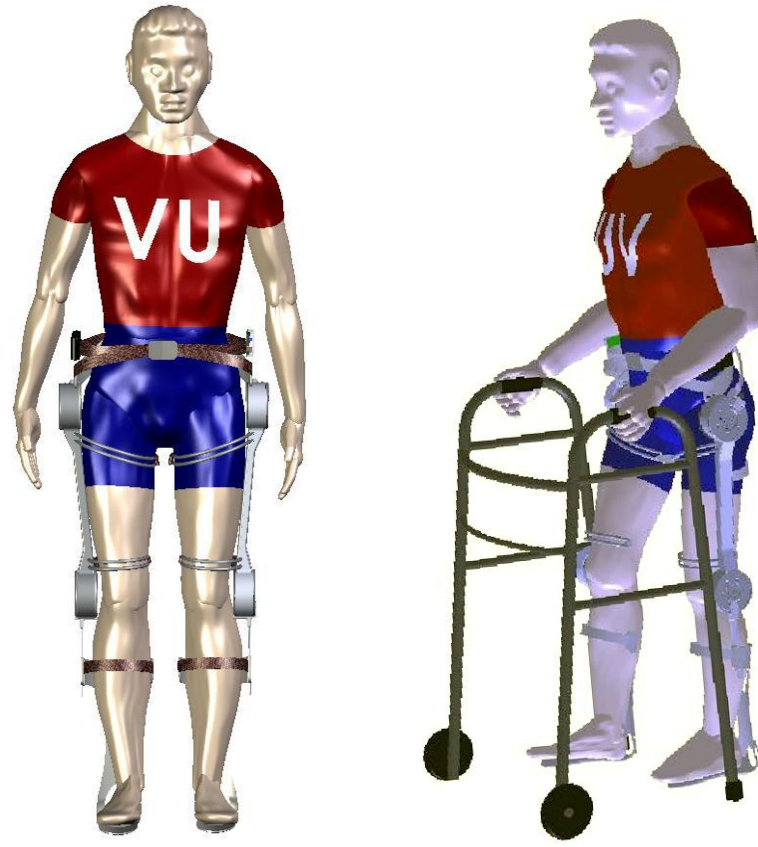


Figure E-2. Anthropomorphic 50th percentile male with JCO and with walker for stability aid.

3.1 *The JCO Gait Sequence*

The gait control approach is described subsequently in the section on gait control and simulation, but is described briefly here to motivate the design of the JCO. Postural stability during gait is provided by a stability aid, such as a walker (see Fig. E-2). The knee of each leg is locked by the controllable friction brakes during stance (see Fig. E-3). Swing is initiated by unlocking the swing leg knee brake, which releases the energy in the biasing spring, which flexes the knee joint and (due to the joint coupling) also flexes the hip joint. During the second half of the swing phase, the hip is locked by the

hip brake while the knee is extended by stimulating the quadriceps group. This knee extension (due to stimulation of the quadriceps) does not, however, generate ipsilateral hip extension, since the (cable-based) coupling is unidirectional. Once the knee is fully extended, it remains locked (by the knee brake) during the stance phase of gait.

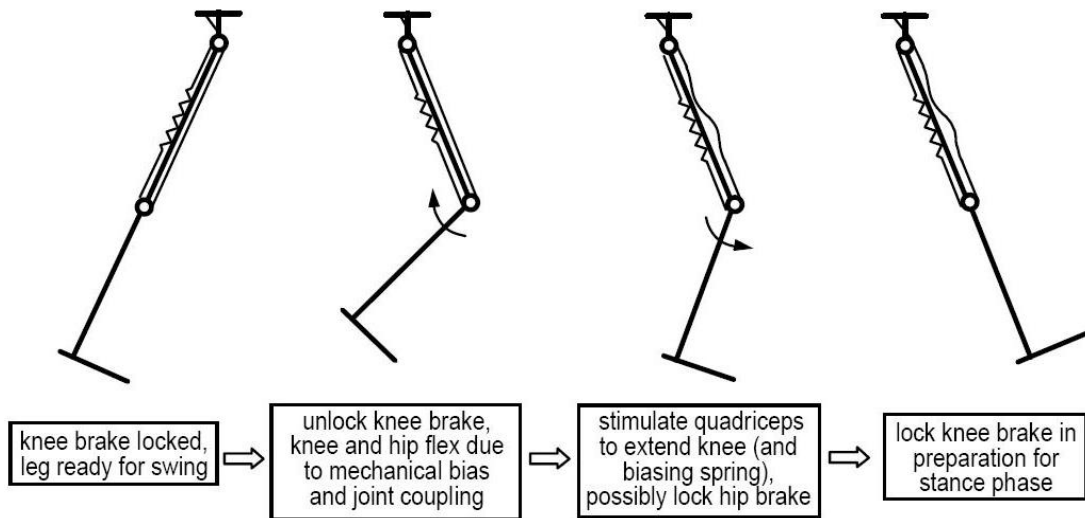


Figure E-3. Schematic representation of JCO swing phase of gait, indicating the cooperative behavior and sequencing of the knee and hip brakes, the mechanical bias spring, the unidirectional joint coupling, and the quadriceps stimulation.

3.2 Joint Coupling Design

The purpose of the joint coupling is to provide hip flexion necessary to generate forward leg motion, which is otherwise a challenge, due to the inaccessibility of the deep hip flexor muscles via surface stimulation. The JCO design incorporates a Bowden cable which spans the inside of the femur link and attaches to the hip and knee rotors

on either end (see Fig. E-4). Cable compression sleeves are used in the hip brake as hard stops in only one direction of rotation, which provides unidirectional coupling of knee flexion to hip flexion. During knee extension, the distal end of the inner Bowden cable winds around the inner hip brake rotor without inducing concurrent hip extension (see Fig. E-4d).

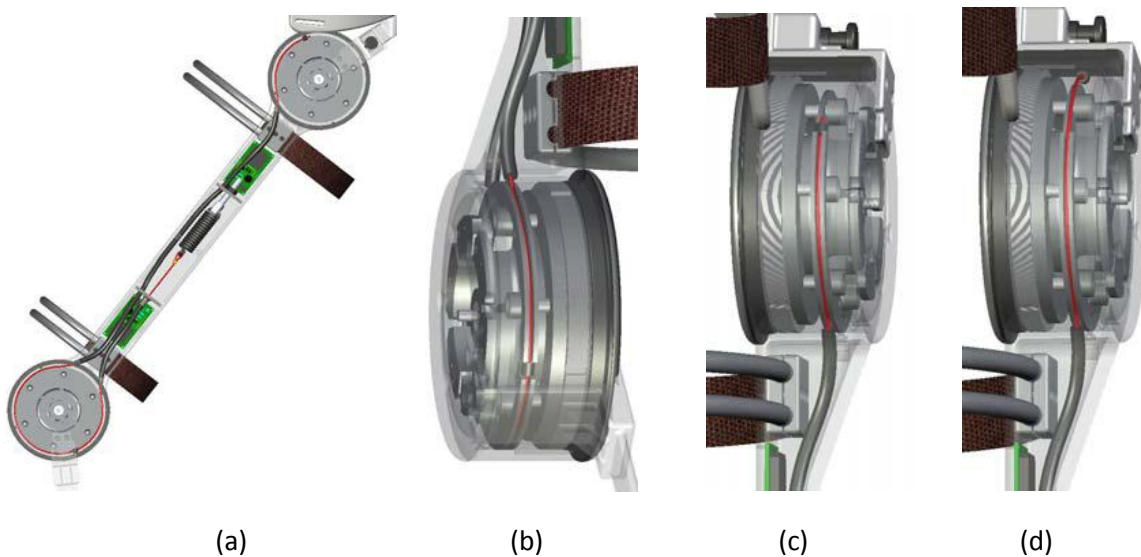


Figure E-4. (a) Femur link shown with joint biasing and coupling cable highlighted in red, (b) detail view of knee joint, showing joint biasing and coupling cable, (c) detail view of hip joint, showing joint coupling cable in the engaged position (e.g., during the knee flexion part of swing phase), and (d) detail view of hip joint, showing joint coupling cable in the disengaged position (e.g., during knee extension part of swing phase). Note that while in the disengaged position, the hip cable is guided around the inside of the hip joint housing, as shown in (d). Note that this figure is clearest when viewed in color.

As previously mentioned, the power for knee (and therefore hip) flexion is provided by the quadriceps, but is stored in an extension spring housed within the femur tube (see Fig. E-5). This spring is attached to the returning end of the Bowden cable which is wrapped around the knee brake rotor, thus creating a torque in the direction of knee flexion as determined by the spring stiffness, equilibrium point, and preload (against a joint hard stop).

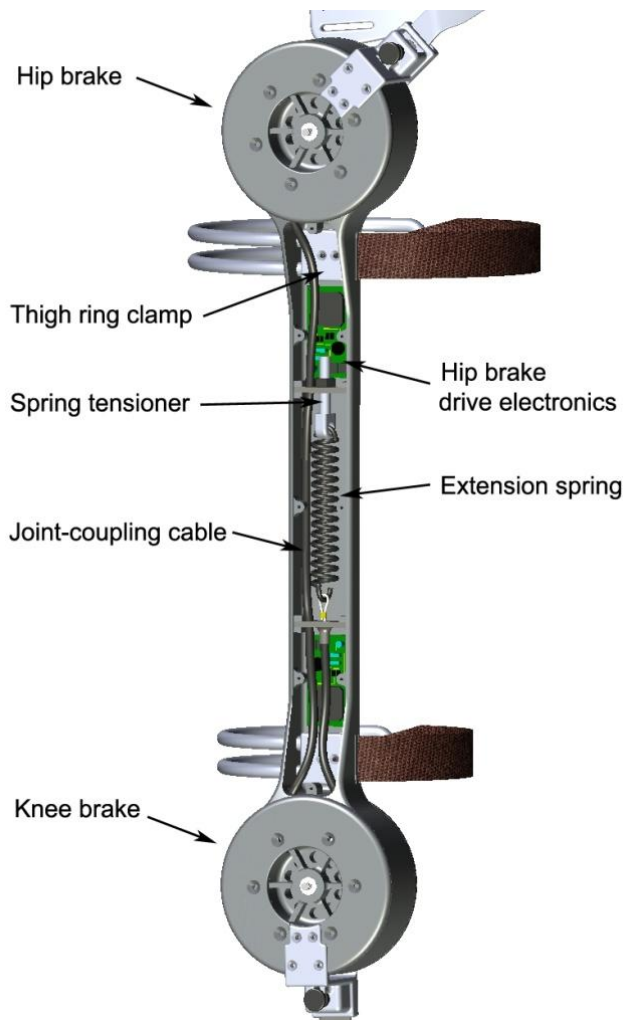


Figure E-5. Femur link detail.

3.3 *Wafer Disc Brakes*

A key component of the JCO is the wafer disc brake (WDB), which serves a threefold purpose: 1) provide added safety via the normally “locked” design of the knee brake, which will prevent the wearer from falling should the device lose power; 2) increase muscle efficiency by locking joints during phases of gait when they are normally static, thus taking the burden of support off the leg muscles, reducing muscle fatigue and allowing longer walking times; and 3) smooth and control leg trajectories for a more natural and repeatable gait by utilizing the brakes as variable dampers controlled in relation to joint angle feedback. A previous effort to create a controlled brake orthosis [20, 24, 25] utilized magnetic particle brakes, which require electrical power to impose resistive torque. In the event of a power failure, the brakes (and thus the orthosis joints) remain unlocked, which could result in collapse and serious injury to the individual. The authors have developed a new type of brake, called a wafer disc brake, which provides nearly 45 times the torque-to-weight ratio of state-of-the-art magnetic particle brakes, and importantly, can be designed in either a “normally locked” mode or “normally unlocked” mode. Since the knee joints should fail in a locked mode, as previously mentioned, the knee brakes are thus of the normally locked type. Since the hip brakes are used primarily for trajectory control and are characterized by relatively low duty cycle operation, the hip brakes are of the normally unlocked type. Designing knee brakes to be normally locked and hip brakes to be normally unlocked both minimizes electrical power consumption (based on data from [25], and importantly prevents collapse during an electrical power failure. The normally unlocked WDB, which was

designed for the hip joint, consists of a stack of thin high-strength plastic wafers which are alternatively coupled (through splines) to the brake stator and rotor. A small brushless motor located inside the brake shaft transmits a compressive force through a ball screw to the stack. Assuming relatively low friction in the ball screw, the stack is subjected to a compressive force which is proportional to the motor current. Due to the series arrangement of discs, the resistive torque on the rotor is the product of the compressive force, the mean radius of contact, and the coefficient of friction, which is amplified by the number of interfaces between discs. Since the hip brake contains 71 discs, the effective hip torque is increased by a gain of 70. Since the ball screw is back-drivable, the brake torque remains in proportion to the motor current, and thus is proportional in nature. The normally locked type of WDB, which is used for the knee joint, is shown in cross-section in Fig. E-6. A photo of the corresponding assembled prototype is shown in Fig. E-7. The design is similar to the normally unlocked type, but the discs are preloaded with a compression spring. Applying current to the motor proportionally unloads the preload, such that full brake torque occurs at zero motor current, and minimum brake torque occurs at full motor current. Since the ball screw is back-drivable, the brake torque remains in inverse proportion to the motor current.

A first-generation prototype of the knee brake has been constructed and tested. The mass of this brake is 0.73 kg. The brake was experimentally measured to provide a maximum torque of 50.7 N-m, which provides a resistive torque-to-weight ratio of 69.4 N-m/kg. In comparison, a state-of-the-art magnetic particle brake (MPB) in a similar size range provides a torque of 1.7 N-m with a mass of 1.14 kg, and as such has a resistive

torque-to-weight ratio of 1.5 N-m/kg (e.g., Placid Industries model no. B15). As such, the WDB has a torque-to-weight ratio approximately 45 times greater than the MPB. Experimental measurements further indicate a minimum torque of 0.16 N-m (i.e., the brake dynamic range is between approximately 0.2 and 50 N-m). Note that this provides a dynamic range ratio of 250:1. The aforementioned MPB has a dynamic range of 100:1, and thus the WDB provides significantly improved performance (relative to the MPB) with respect to both torque/weight ration and dynamic range. For both WDB brake types, the torque varies linearly (and inversely, for the knee brake) with input current.

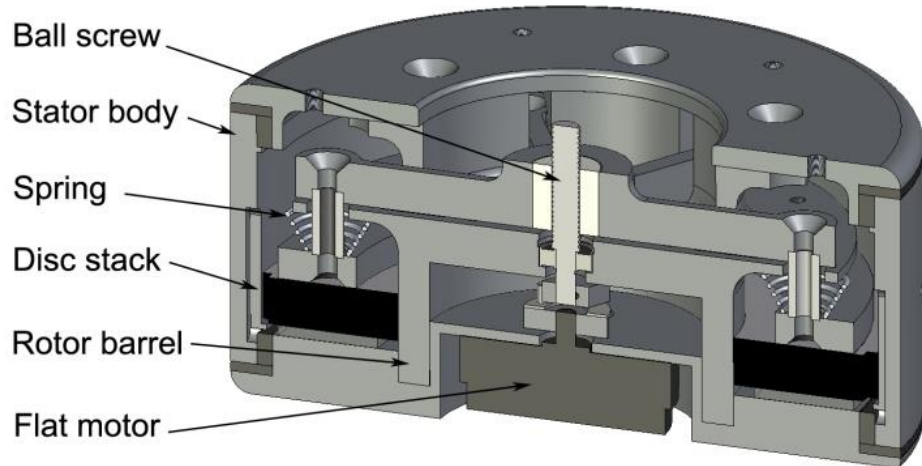


Figure E-6. Cross-section of normally locked knee brake.



Figure E-7. Fully functional knee brake prototype.

3.4 Ankle Support

The JCO utilizes an ankle-foot-orthosis (AFO) at the ankle, which is sufficiently compliant to allow dorsiflexion during the stance phase of gait, but sufficiently stiff to prevent foot drop during the swing phase of gait. Current gait simulations indicate a stiffness of 15 Nm/rad (for a 75 kg user) provides an appropriate balance between these objectives.

3.5 Mass and Inertia

The total orthosis mass as shown in Fig. E-1, based on the solid model and prototypes of the brakes, is approximately 6 kg (13 lbs). Approximately one half of the orthosis weight is located on the pelvis, and thus does not add significantly to the

rotational inertia or gravitational loads of the lower limbs. The rotational inertia of the distal link of the orthosis about the knee joint is approximately 5% of a typical shank inertia, while the inertia of the proximal link about the hip joint is about 10% of a typical thigh inertia.

3.6 *Donning and Doffing*

Along with reliability, function, and perceived and measurable benefit, one of the most important factors in the acceptance and use of a gait restoration system is ease of use, and chief among this factor is the ability of the user to quickly and easily don and doff the system. The JCO was designed to be donned (and doffed) quickly, easily, and independently, while sitting. The JCO consists of five component parts, which are separately donned and snapped together via structural quick connect joints. Specifically, the JCO is separated into two AFO's, two thigh segments, and a waist harness, shown in Fig. E-8.



Figure E-8. Depiction of steps for donning JCO.

4. Simulation

A simulation of the JCO and gait controller was conducted for a user of height $L=1.7\text{m}$ and mass $M=65\text{kg}$. Detailed simulation results are reported in a companion paper. The cadence of the resulting gait was 34 steps per minute and the average velocity was 0.2 m/s . A depiction of the simulation progression is shown in Fig. E-9. Importantly, the simulation indicates a required quadriceps stimulation duty cycle of approximately 15%.

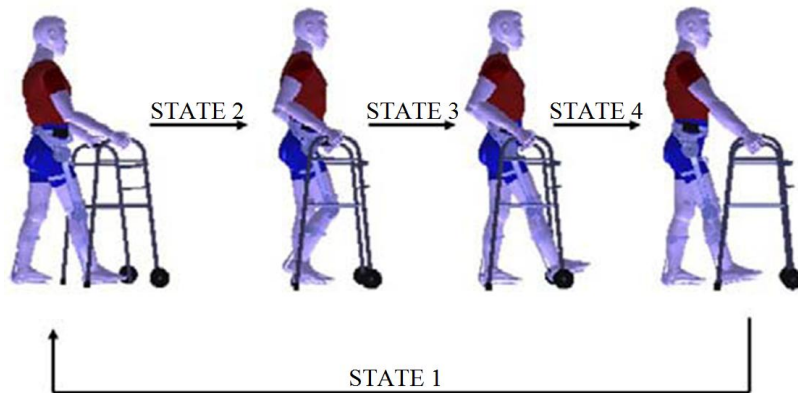


Figure E-9. Progression of simulation states.

5. Preliminary Experiments

The authors have conducted preliminary experiments to test the joint coupling concept, and to assess the extent of fatigue imposed by the bias spring and joint

coupling. A preliminary, one-legged version of the orthosis was created which included one-to-one joint coupling between the hip and knee, an adjustable extension spring for knee flexion, potentiometers on the hip and knee joints for angle measurement, and a locking knee joint with quick release pin. Experiments were conducted to 1) determine if the spring and joint coupling could provide sufficient knee and hip flexion in the context of stride, and 2) determine if the quadriceps could repeatably provide the power necessary to overcome the spring and extend the lower leg without significant fatigue. The first experiment (see Fig. E-10) involved positioning an able-bodied subject in stance such that the leg wearing the orthosis was in the rear and ready to begin stride. The spring was loaded and the knee was locked in the extended position by means of a quick connect pin. As the pin was pulled, the leg swung forward in knee and hip flexion as shown in Figs. E-10 and E-11. At the peak of hip flexion, the quadriceps was stimulated, which fully extended the knee. Based on the resulting motion, the proposed approach appears to provide hip and knee swing motion necessary for gait restoration.

The second experiment involved conducting extended sets of pulsed quadriceps stimulation at a duty cycle of 15%— as indicated by the gait simulations. Ten subjects underwent three five minute periods of stimulation with a rest period in between each trial of three minutes.

Representative data (showing stimulation duty cycle and knee and hip angles) for a few cycles of stimulation for a single subject is shown in Fig. E-12. Note that, since the test orthosis does not include a locking knee brake, the hip and knee joints return to

the flexed position immediately following the quadriceps stimulation (unlike in the proposed gait sequence, in which the knee joint would be locked at full extension following quadriceps stimulation, and would unlock only during the swing phase of gait).

Representative knee angle data for an entire five-minute trial is shown in Fig. E-13.

For each subject, the amplitude of knee motion corresponding to each flexion/extension cycle was collected and plotted versus cycle (84 cycles per trial, 252 cycles total for the three trials). A representative plot of this data for a single subject is shown in Fig. E-14, which also shows a least-squares-fit line through each of the three consecutive five-minute trials. Note that the discontinuity in the lines is due to the three-minute rest period between trials. The average decrease in flexion angular displacement (across all subjects) over the first five-minute trial was 13% and over the second five-minute trial was 10%. As shown in Fig. E-14, however, the average flexion amplitude (across all subjects) during the third trial showed no decrease (in fact showed a 1% increase).



Figure E-10. FES/JCO generated gait sequence experiment.

Frame 1: Right leg is locked in shown position. Assistant pulls pin to unlock the knee joint. **Frames 2-5:** Once pin is pulled, the spring pulls the knee into flexion and the joint coupling therefore pulls the hip into flexion as well. Frame 5 is the final resting state under no muscle contraction. **Frames 6-8:** The quadriceps is stimulated by a momentary push button switch on the walker handle. This causes the knee to extend and therefore relieve the joint coupling, allowing the hip to extend also. Frame 8 is the final resting position of the leg after it has rejoined the ground after stride.

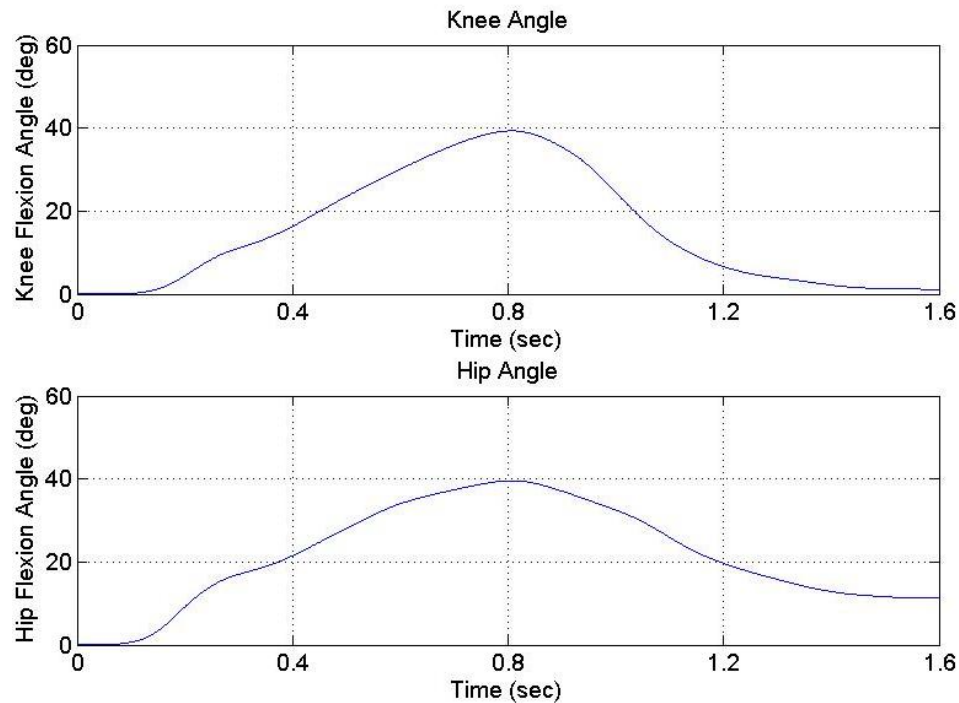


Figure E-11. Joint angle data during gait experiment shown in Fig. E-10.

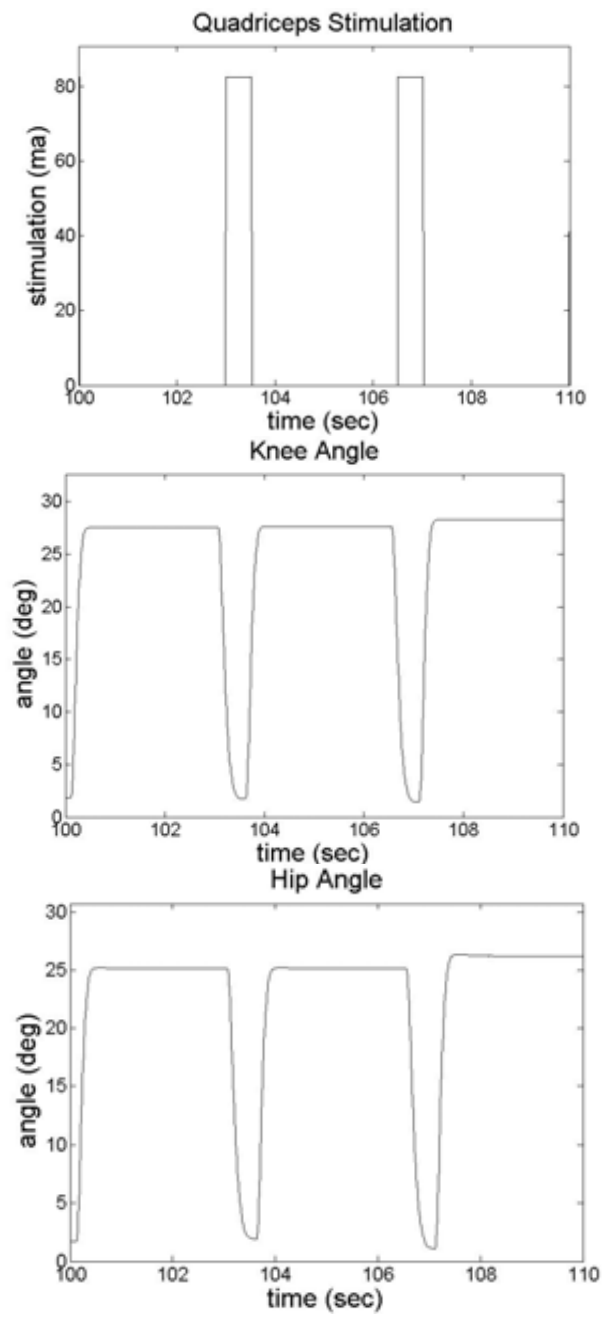


Figure E-12. Representative data from the quadriceps fatigue experiments, showing amplitude of quadriceps stimulation, knee angle as measured by the test orthosis, and hip angle.

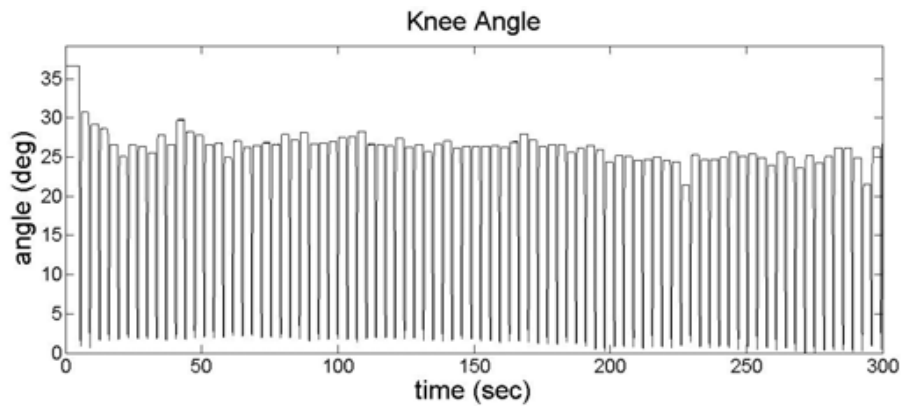


Figure E-13. Representative data from a five-minute trial for FES powered knee (and hip, via joint coupling) extension while wearing the test orthosis.

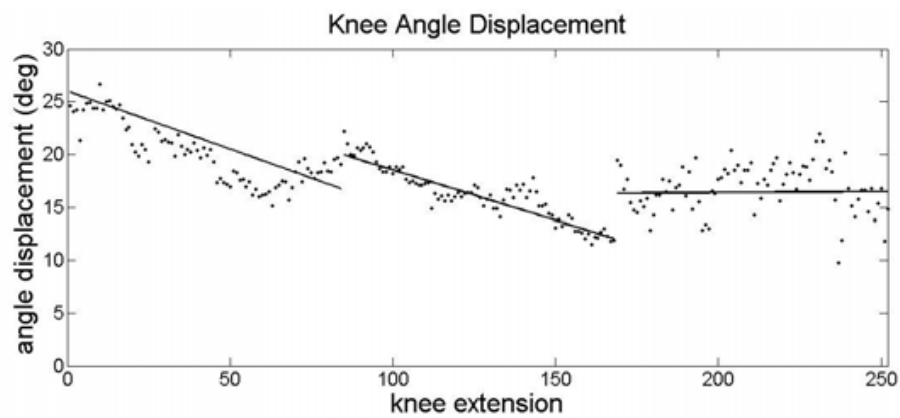


Figure E-14. Representative data from a single subject for three consecutive (five-minute) trials, and least-squares fit line for each trial. The discontinuity in lines is due to the three-minute rest between trials.

Thus, for conditions representative of the proposed approach, the data appears to indicate stabilization in average flexion amplitude by the third five-minute trial. More specifically, based on the averaged data of ten subjects, the flexion amplitude appears to have stabilized at approximately 85% of the mean amplitude exhibited during the first five-minute trial. Importantly, this apparent stabilization indicates that, for the 15% duty cycle and workload imposed on the quadriceps by the JCO, the proposed approach should be capable of providing long periods of locomotion unimpeded by quadriceps muscle fatigue.

6. Conclusion

A joint-coupled controlled brake orthosis (JCO) has been designed as part of a hybrid FES/orthosis system for restoring gait to spinal cord injured individuals. This device will 1) unidirectionally couple hip to knee flexion; 2) aid hip and knee flexion with a spring assist; and 3) incorporate sensors and modulated friction brakes, which are used in conjunction with electrical stimulation for the feedback control of joint (and therefore limb) trajectories. A one-legged joint coupling prototype was used to validate the joint coupling concept and assess the fatigue induced by the system upon the quadriceps muscles. Based on the motion obtained using the prototype and quadriceps stimulation, the proposed approach appears to provide hip and knee swing motion necessary for gait restoration. Furthermore, results from the preliminary fatigue testing showed that muscle output appeared to stabilize at 85% of its initial output after 15 minutes of stimulation. As such, the quadriceps appears to be capable of providing

sustained power for the proposed hybrid approach to support continuous walking without significant degradation of performance. Future work includes characterization of the latest brake prototype, development of a fully functional, two-legged JCO, control design, on-board electronics, and clinical trials of the JCO system.

7. References

- [1] Axelson PW, Gurski D, and Lasko-Harvill A. "Standing and its importance in spinal cord injury management." In Proceedings of the RESNA 10th Annual Conference, pp. 477-479, 1987.
- [2] Gruner J, Glaser RM, Feinberg SD, Collins SR, and Nussbaum NS. "A system for evaluation and exercise-conditioning of paralyzed leg muscles." *J. Rehabilitation R&D*, vol. 20, no. 1, pp. 21-30, 1983.
- [3] Turk R and Obreza P. "Functional electrical stimulation as an orthotic means for the rehabilitation of paraplegic patients." *Paraplegia*, vol. 23, no. 6, p. 345, 1985.
- [4] Phillips L, Ozer M, Axelson P, and Chizek H. "Spinal cord injury: A guide for patient and family." Raven Press, 1987.
- [5] Ragnarsson K. "Physiologic effects of functional electrical stimulation induced exercises in spinal cord-injured individuals." *Clin. Orthop. Rel. Res.*, vol. 233, pp. 53-63, 1988.
- [6] Kaplan P, Gandhavadi B, Richards L, and Goldschmidt J. "Calcium balance in paraplegic patients: Influence of injury duration and ambulation." *Archives of Physical Medicine and Rehabilitation*, vol. 59, pp. 447-450, 1978.
- [7] Odeon I and Knutsson E. "Evaluation of the effects of muscle stretch and weight load in patients with spastic paraparesis." *Scandinavian Journal of Rehabilitative Medicine*, vol. 13, pp. 117-121, 1981.
- [8] Triolo RJ and Bogie K, "Lower Extremity Applications of Functional Neuromuscular Stimulation After Spinal Cord Injury," *Topics in Spinal Cord Injury Rehabilitation*, vol. 5, pp. 44-65, 1999.

- [9] Creasey GH, Ho CH, Triolo RJ, Gater DR, DiMarco AF, Bogie KM, and Keith MW, "Clinical applications of electrical stimulation after spinal cord injury," *J Spinal Cord Med*, vol. 27, pp. 365-75, 2004.
- [10] Cybulski G, Penn R, and Jaeger R, "Lower extremity functional neuromuscular' stimulation in cases of spinal cord injury," *Neurosurgery*, vol. 15, pp. 132-146, 1984.
- [11] Muller EA. "The influence of training and inactivity on muscle strength." *Archives of Physical Medicine and Rehabilitation*, vol. 51, p. 449, 1978.
- [12] Pacy PJ, Evans RH, and Halliday D. "Effect of anaerobic and aerobic exercise promoted by computer regulated functional electrical stimulation (FES) on muscle size, strength and histology in paraplegic males." *Prosthetics and Orthotics International*, vol. 11, no. 2, p. 78, 1987.
- [13] Pacy PJ, Hesp R, Halliday D, Kath D, Cameron G, and Reeve J. "Muscle and bone in paraplegic patients, and the effect of functional electrical stimulation." *Clinical Science*, vol. 75, pp. 481-487, 1988.
- [14] Stefancic M, Kralj A, Turk R, Bajd T, Benko H, and Sega J. "Neurophysiological background of the use of functional electrical stimulation in paraplegia." *Electromyogr. Clin. Neurophysio.*, vol. 26, nos. 5/6, p. 433, 1986.
- [15] Gallien P, Brissot R, Eyssette M, Tell L, Barat M, Wiart L, Petit H. "Restoration of gait by functional electrical stimulation for spinal cord injured patients. Paraplegia.", vol. 33, pp. 660-664, 1995.
- [16] Brissot R, Gallien P, Le Bot MP, Beaubras A, Laisne D, Beillot J, Dassonville J. "Clinical experience with functional electrical stimulation-assisted gait with Parastep in spinal cord-injured patients." *Spine.*, vol. 25, no. 4, pp. 501-508, 2000.
- [17] Guest RS, Klose KJ, Needham-Shropshire BM, Jacobs PL. "Evaluation of a training program for persons with SCI paraplegia using the Parastep 1 ambulation system: part 4. Effect on physical self-concept and depression." *Arch Phys Med Rehabil.*, vol. 78, no. 8, pp. 804-807, 1997.
- [18] Nash MS, Jacobs PL, Montalvo BM, Klose KJ, Guest RS, Needham-Shropshire BM. "Evaluation of a training program for persons with SO paraplegia using the Parastep 1 ambulation system: part 5. Lower extremity blood flow and hyperemic response to occlusion are augmented by ambulation training." *Arch Phys Med Rehabil.*, vol. 78, no. 8, pp. 808-814, 1997.

- [19] Benton L, Baker L, Bowman B, and Waters R. "Functional Electrical Stimulation: A Practical Guide, 2nd edition." Professional Staff Association, Rancho Los Amigos Rehabilitation Engineering Center, Rancho Los Amigos Hospital, Downey CA, 1981.
- [20] Goldfarb M, Durfee W, Korkowski K, and Harrold B. "Evaluation of a Controlled-Brake Orthosis for FES-Aided Gait," IEEE Transactions on Neural Systems and Rehabilitative Engineering, vol. 11, no. 3, pp. 241-248, 2003.
- [21] Kobetic R, Marsolais EB, Triolo RJ, Davy DT, Gaudio R, and Tashman S, "Development of a hybrid gait orthosis: a case report," J Spinal Cord Med, vol. 26, pp. 254-8, 2003.
- [22] To CS, Kirsch RF, Kobetic R, and Triolo RJ. "Simulation of a functional neuromuscular stimulation powered mechanical gait orthosis with coordinated joint locking." IEEE Transactions on Neural Systems and Rehabilitation Engineering, vol. 13, no. 2, pp. 227-235, 2005.
- [23] Durfee W and Rivard A, "Design and simulation of a pneumatic, stored energy, hybrid orthosis for gait restoration," J Biomech Eng, vol. 127, pp. 1014-9, 2005.
- [24] Goldfarb M. "A controlled brake orthosis for FES-aided gait." PhD Thesis, Massachusetts Institute of Technology, 1994.
- [25] Goldfarb M and Durfee W. "Design of a Controlled-Brake Orthosis for Regulating FES-Aided Gait." IEEE Transactions on Rehabilitation Engineering, vol. 4, no. 1, pp. 13-24, 1996.
- [26] Winter DA. "The biomechanics and motor control of human gait: normal, elderly and pathological," University of Waterloo Press, 2nd ed, 1991.